THE UNIVERSITY *of* EDINBURGH

This thesis has been submitted in fulfilment of the requirements for a postgraduate degree (e.g. PhD, MPhil, DClinPsychol) at the University of Edinburgh. Please note the following terms and conditions of use:

- This work is protected by copyright and other intellectual property rights, which are retained by the thesis author, unless otherwise stated.
- A copy can be downloaded for personal non-commercial research or study, without prior permission or charge.
- This thesis cannot be reproduced or quoted extensively from without first obtaining permission in writing from the author.
- The content must not be changed in any way or sold commercially in any format or medium without the formal permission of the author.
- When referring to this work, full bibliographic details including the author, title, awarding institution and date of the thesis must be given.

A study on lipid droplet dynamics in live cells and fluidity changes in model bacterial membranes using optical microscopy techniques

Author: Christine Shiang Yee WONG

THESIS SUBMITTED IN FULFILLMENT OF THE

REQUIREMENTS FOR THE DEGREE OF

Doctor of Philosophy

THE SCHOOL OF PHYSICS AND ASTRONOMY

THE UNIVERSITY OF EDINBURGH

2013

Abstract

In this thesis optical microscopy techniques are used to consider aspects of viral and bacterial infections. In part 1, the physical effects of cytomegalovirus on lipid droplet dynamics in live cells are studied; in part 2, the effects of an antimicrobial peptide on the fluidity of model bacterial membranes are studied.

The optical microscopy techniques used to study the effects of murine-cytomegalovirus (mCMV) on lipid droplets in live NIH/3T3 fibroblast cells in real-time are coherent anti-Stokes Raman scattering (CARS), two-photon fluorescence (TPF) and differential interference contrast (DIC) microscopies. Using a multimodal CARS and TPF imaging system, the infection process was monitored by imaging the TPF signal caused by a green fluorescent protein (GFP)-expressing strain of mCMV, where the amount of TPF detected allowed distinct stages of infection to be identified. Meanwhile, changes to lipid droplet configuration were observed using CARS microscopy. Quantitative analysis of lipid droplet numbers and size distributions were obtained from live cells, which showed significant perturbations as the infection progressed. The CARS and TPF images were acquired simultaneously and the experimental design allowed incorporation of an environmental control chamber to maintain cell viability. Photodamage to the live cell population was also assessed, which indicated that alternative imaging methods must be adopted to study a single cell over longer periods of time. To this end, DIC microscopy was used to study the lipid droplet dynamics, allowing lipid droplet motion to be tracked during infection. In this way, the effects of viral infection on the mobility and arrangement of the lipid droplets were analysed and quantified. It was found that the diffusion coefficient of the lipid droplets undergoing diffusive motion increased, and the droplets undergoing directed motion tended to move at greater speeds as the infection progressed. In addition, the droplets were found to accumulate and cluster in infected cells.

The second part of this thesis presents a study on the effects of an antimicrobial peptide on model bacterial membranes. Giant unilamellar vesicles (GUVs) were produced as a simple model of *E. Coli* membrane using a 3:1 mixture of DPPC and POPG lipids. Incorporating Laurdan fluorescent dye into the lipid membrane of the GUVs allowed the membrane fluidity to be probed and visualised using TPF microscopy, whereby the fluidity was quantified by determining the general polarization (GP) values. Studying GUVs comprising single lipid and mixed lipid compositions over a temperature range from 25 °C to 55 °C enabled the lipid phase bands to be identified on the basis of GP value as gel phase and liquid crystalline phase. As such, the changes in lipid phase as a result of interaction with AMP were quantified, and phase domains were identified. It was found that the amount of liquid crystalline phase domains increased significantly as a result of AMP interaction.

Summary

This thesis presents the results of two studies: the first study investigates the effects of cytomegalovirus on lipid droplet dynamics in live cells, and the second study investigates the effects of antimicrobial peptides on model bacterial membrane fluidity.

Cytomegalovirus infects a majority of the worlds population, and although infection symptoms are typically mild (cold sores), the infection can become fatal for infected individuals with compromised immune systems. The virus is also capable of evading the host immune system, and therefore can evade complete eradication. As such, understanding the mechanisms involved in the viral life-cycle is important to enable permanent elimination of the virus from the host. Intracellular lipid droplets have been identified to be involved in cytomegaloviral infections, however it is currently unknown exactly how the virus associates with lipid droplets. The study presented in this thesis uses real-time imaging to investigate the physical effects of the viral infection on lipid droplet dynamics, arrangement and accumulation in live cells. It was found that the diffusion coefficient of the lipid droplets undergoing diffusive motion increased, and the droplets undergoing directed motion tended to move at greater speeds as the infection progressed. In addition, the droplets were found to accumulate and cluster in infected cells.

The second study investigates the effects of antimicrobial peptides on model bacterial membrane fluidity. A major issue regarding the control of bacterial infections is that bacteria are evolving resistances to current antibiotics. Therefore, a large research focus has been directed to develop alternative forms of antimicrobial agents, such as antimicrobial peptides (AMPs), which are also found naturally in humans and animals. The interest in AMPs stems from the possibility that bacteria may not evolve resilience against these agents as AMPs have been effective for millions of years. In order to develop fully effective AMPs, complete understanding of how they interact with bacteria must be established. Currently, it is believed that to kill bacteria, the bacterial membrane must be disrupted, however the precise mechanisms as to how AMPs disrupt the membrane are unknown. The study presented investigates whether the effects of antimicrobial action on model bacterial membranes induces drastic changes in membrane fluidity. It was found that the presence of AMPs significantly increases the fluidity of the membranes, which implies that the structural integrity of the membranes may be reduced, with an increase in structural defects.

Declaration

I hereby declare that the writing of this thesis is my own work and that, to the best of my knowledge and belief, it contains no material previously published or written by another person nor material which to a substantial extent has been accepted for the award of any other degree or diploma of the university or other institute of higher learning, except where due acknowledgement has been made in the text.

signature: _____

name: _____

date: _____

Acknowledgements

Many people have been involved these last few years to enable this thesis to be achieved, either by providing academic support and guidance, practical support and guidance, or emotional support and general fun and laughter. I would now like to take this opportunity to thank everyone that has made this all possible.

Firstly, I would like to express my thanks and gratitude to my primary supervisor, Simon Titmuss, for providing invaluable scientific expertise and support, and for mentoring and guiding me through this PhD. Also to my secondary supervisor, Jochen Arlt for his invaluable technical expertise and practical help in optics, and Iain Robinson, who guided me through the initial stages of the PhD.

I would also like to thank Michael Ochsenkühn, and Jana Schwarz-Linek for practical help, biological advice and provision of various biological samples. Mathieu Blanc for the provision of biological samples. Andy Garrie for his technical skill in building various cell chambers and parts for the microscope. Hugh Vass for his experience and advice in optics, and Angela Dawson for advice in the biolabs.

My colleagues and friends have been invaluable these last few years, and are responsible for making these years enjoyable and memorable.

A special thanks to Nick Barnes, for his love and support, especially throughout the most stressful period of the PhD, in addition to his coding and scripting prowess.

Most of all, my family: my dad, sister and brother, and especially my mum, who have always been there for me with their unending love, support and continuous encouragement. (Amy, I know you wanted a special mention so here it is, also I am very excited about your amazing cake).

Contents

List of Figures

List of Tables

1 Introduction

Two studies are presented in this thesis: the first study investigates the effects of cytomegalovirus (CMV) on lipid droplet dynamics in live cells, and the second study investigates the effects of antimicrobial peptides on model bacterial membrane fluidity.

1.1 Part 1

CMV infects a majority of the worlds population, and although the symptoms of the infection are typically mild (cold sores), the infection can become fatal and cause severe damage to the central nervous system in individuals with compromised immune systems, such as organ transplant or AIDS patients. An infected host is infected for life as the virus is capable of evading the host immune responses, therefore understanding the behaviour of CMV could help in developing treatments. As the virus is smaller than the resolution limit of far field imaging techniques, it cannot be directly imaged *in vivo*. Instead, the response of the host cell to the pathogen gives an indirect method of studying the effects of CMV infections.

Intracellular lipid droplets have been identified to be involved in CMV infections, in particular the viral infection affects the sterol metabolic pathway (the regulation of sterols). Studies have also found potential links between CMV infection and lipid droplet accumulations with evidence of a link between CMV infection and high levels of low-density lipoprotein

(LDL) cholesterol, and high levels of cholesterol ester deposits on arterial walls. However, currently there have been no direct studies regarding how CMV are involved with lipid droplets, and no studies have been done to investigate how the dynamics, arrangement and/or accumulation of the lipid droplets are influenced by the virus.

1.2 Part 2

The majority of bacteria are not pathogenic, however there are many that cause disease, infections, or illness such as *E. Coli* O157:H7, which is the strain of *E. Coli* that causes severe (possibly fatal) food poisoning. The ability to control infectious strains of bacteria is crucial, and is currently a major research focus as unfortunately, bacteria are able to adapt and evolve in order to counter antibiotics. This has resulted in significant efforts to develop alternative forms of antimicrobial agents. Antimicrobial peptides (AMPs) are natural antimicrobial agents that can be found in humans and animals. Since these peptides are naturally occurring and have been effective for millions of years, the interest in AMPs stems from the possibility that bacteria may not be able to evolve a resilience against these agents. In order to develop fully effective AMPs, a complete understanding of how they interact with bacteria must be established. Currently, it is believed that for the antimicrobial agent to kill bacteria, the bacterial membrane must be disrupted, however the precise mechanism of how AMPs disrupt the membrane is unknown, and is most likely dependant on the peptide, the bacteria and/or environment. It is known that bacterial membranes are dynamic and that the fluidity can be modulated to adapt to changes in the environment. For this reason it is interesting to determine whether an effect of antimicrobial action on bacteria is to perturb the membrane in such a way that induces drastic changes in membrane fluidity, leading to structural defects and loss in integrity.

1.3 Thesis layout

Chapter 2 discusses the optical techniques used for the studies in this thesis, giving an overview of the theory behind the techniques and the benefits and drawbacks for each.

Chapter 3 gives an overview of the biological specimens that were studied, in addition to antimicrobial peptides, viruses and lipid droplets.

Chapter 4 and 5 detail the study on the dynamics of cellular lipid droplets in both healthy cells and cells infected with cytomegalovirus. Chapter 4 presents the results of the study of lipid droplets in live fibroblast cells at different stages of infection using a multimodal coherent anti-Stokes Raman scattering (CARS) and two-photon fluorescence (TPF) imaging system, which enabled changes in lipid droplet configurations to be quantified in relation to the stage of infection. Chapter 5 presents the results of the study on lipid droplet dynamics, where differential interference contrast (DIC) microscopy was used to enable the lipid droplets to be tracked. In this way, the effects of viral infection on the mobility and arrangement of the lipid droplets were analysed and quantified.

Chapter 6 presents the second part of this thesis, in which the effect of antimicrobial peptides on the fluidity of model bacterial membranes was studied. The chapter reports the work to quantify and characterise different lipid phases, which were then used to determine the changes in fluidity as a result of antimicrobial peptide action.

Chapter 7 concludes, and underlines the main findings in this thesis. Potential avenues for further work are also detailed.

The publication relating to the work in Chapter 4 is included in the appendix.

2

Cellular Imaging Techniques

2.1 Introduction

Transparent specimens such as living cells are problematic when it comes to imaging, since under a standard brightfield microscope the image appears with very little contrast and most cellular features remain invisible to the eye (1). Consequently, to enable the biological and physical processes of tissue and cells to be studied, the development of more complex optical microscopes, either involving fluorescent markers or label free imaging and phase contrast techniques have been paramount (2–5). In addition to increasing the image contrast of transparent specimens, there are many other challenges with regards to imaging living cells *in vivo*, such as maintaining cell viability during imaging, minimizing the effects of photodamage from the illuminating light source and reducing the rate of photobleaching when fluorescent dyes are used as markers to depict specific biological components within the cells (1). Image resolution also becomes a factor when the organelle or specimen of interest is around or smaller than the resolution limit. For example, the physical dimensions of viruses are smaller than the resolution limit of far field microscopy thereby precluding direct observation *in vivo*, so the effects of host–pathogen interactions are typically studied instead (6). This chapter will give an overview of the label-free and fluorescence microscopy techniques used in this thesis for studying various biological systems: phase contrast, differential interference contrast (DIC),

fluorescence, two photon fluorescence (TPF), and coherent anti-Stokes Raman scattering (CARS) microscopy.

2.2 Brightfield imaging

Even though brightfield microscopy results in minimal image contrast, there are many advantages such as being both low in cost and being technically easy to set up. This makes it a useful technique to use alongside more complicated systems, as it provides an easy method for locating the specimen within a sample before imaging using a more complex microscope system. Most importantly, correct set up of brightfield illumination, as introduced by August Köhler in 1893, ensures a bright, uniform illumination of the sample (1, 7, 8), and is the foundation for more complex brightfield techniques such as phase contrast or differential interference contrast (DIC) imaging.

2.2.1 Köhler Illumination

Correct microscope alignment is essential for obtaining optimal image quality and contrast. In 1893, Köhler developed a technique which optimises sample illumination (1, 8). This is vital because standard light sources such as tungsten bulbs, halogen bulbs or light emitting diodes (LEDs) typically emit light non-uniformly, which results in intensity variations in the image. Köhler illumination ensures that the light is collimated at the sample, ensuring uniform illumination across the field of view. The angle and size of the light cone illuminating the sample can be controlled so that approximately 70% of the objective lens aperture is illuminated, which optimises image contrast and reduces glare/image degradation that would occur if the sample was saturated with light. Since this alignment ensures that only the desired field of view is illuminated, excess scattered light, which reduces image contrast, is eliminated. Additionally, the optical alignment ensures that the lamp filament is not in focus at the sample, as the field (image-forming) conjugate focal planes and the aperture (illumination) conjugate planes are positioned at different locations along the optical axis, as shown in Figure 2.1 (1), and so the projected image of the filament will not interfere with the specimen image.

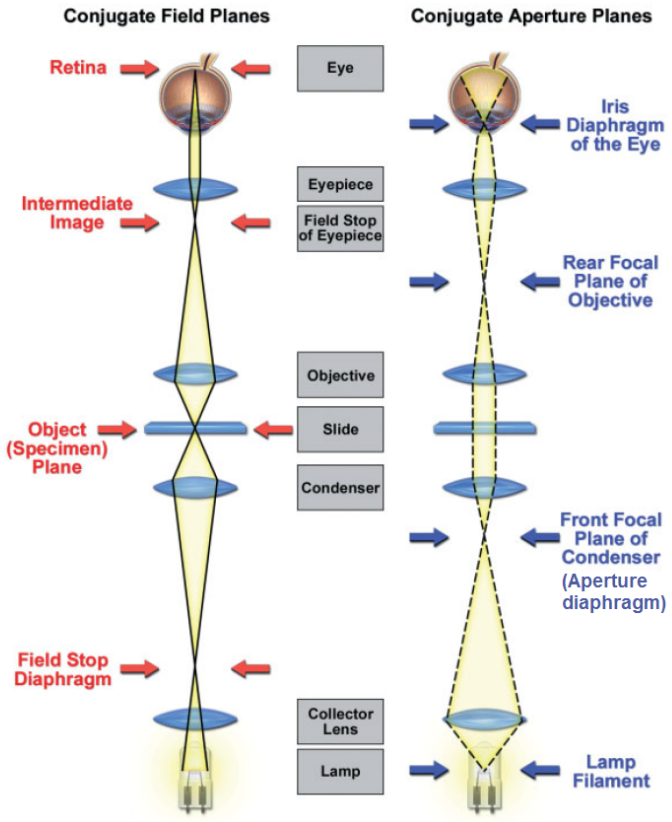

Figure 2.1: The diagram (from ref. (1)) illustrates the position of the two sets of conjugate focal plane positions when Köhler illumination is correctly set up.

2.3 Resolution

The resolution, r, of a microscope is defined as the closest distance where two points can be distinguished as two separate entities (9). The Rayleigh criterion is typically used to determine the resolution of a system and can be calculated using Equation 2.1,

$$r = \frac{0.61\lambda}{NA_{obj}} \tag{2.1}$$

where λ is the wavelength of the illumination, 0.61 is a constant and NA_{obj} is the numerical aperture of the objective lens. In general, the resolution of a system depends on the wavelength of the illumination and the objective lens that is used.

2.4 Further brightfield techniques

As mentioned earlier, Köhler illumination is the base upon which more complex brightfield techniques are built (1, 10, 11), to enable transparent specimens to be imaged at high contrast. This section will provide a brief overview of both phase contrast microscopy and differential interference contrast microscopy.

2.4.1 Phase contrast microscopy

Transparent objects appear nearly invisible because they allow light to pass through without absorbing (or reflecting) the beam. Although transparent objects may induce phase shifts in the illumination (referred to as phase objects) by scattering and diffraction of light, this phase difference cannot be directly detected by the eye, as image contrast is a consequence of the object and illuminating light interacting to give amplitude differences (these objects are referred to as amplitude objects), which are detected by the eye as differences in light intensity (11). Phase contrast microscopy manipulates the phase differences of the diffracted light and converts the phase shifts into corresponding changes in amplitude which can then be detected by the eye and visualised as differences in image contrast. This section will present a brief review on the interaction of light waves with phase objects, and the principles behind phase contrast microscopy.

As an incident wavefront passes through a phase object, the light divides into two components. The first component consists of the majority of incident waves, which pass through the specimen without interaction as an undeviated (zeroth order) planar wavefront, often denoted as the surround wave (S wave) (1). The second component is a small minority of the incident waves, which are scattered in many directions as they pass through the specimen, creating a deviated spherical wavefront. This wavefront differs in phase from the S waves and is often denoted as the diffracted wave (D wave). Both S and D waves pass through the objective lens and are focused at the intermediate image plane, where the waves combine through interference to produce a resultant particle wave (P wave). The relationship between the waves is described as,

$$P = S + D \tag{2.2}$$

Detection of the object image depends on the relative intensity (amplitude) differences between the P and S waves (1) (D waves are not directly observed in the image), where a significant difference between P and S wave amplitudes in the intermediate image plane results in a high contrast image. Typically, the amplitude of the S waves are much greater than the D waves, which is the reason the image of the object is near invisible under simple brightfield microscopes. As such, the underlying concept in the design of a phase contrast microscope is to maximize the difference in amplitude between the P and S waves so as to create a detectable high contrast image. The first element of the optical design is to segregate the S and D waves as they emerge from the specimen, and project them onto different locations in the objective rear focal plane, which is also referred to as the diffraction plane. The second element is to maximise the difference in amplitude between the object and background in the image plane. These two elements are achieved by using a condenser annulus, positioned at the front focal plane of the condenser lens, and that the D waves are retarded in phase by approximately $\lambda/4$ due to scattering at the specimen. In addition, the phase plate positioned at the rear aperture of the objective lens causes the phase of the S waves to be advanced, and the amplitude to be reduced. The path of the S and D waves as they pass through the phase contrast microscope is illustrated in Figure 2.2 (12).

The condenser annulus is typically constructed as an opaque black plate, which is designed to be light absorbing, with a transparent annulus to allow the illumination to be transmitted. Under conditions of Köhler illumination, the S waves that do not interact with the specimen are focused onto the rear focal plane of the objective lens, as a bright ring, whereas light diffracted by the specimen as a spherical wavefront (D waves) passes through the entire rear aperture of the objective lens at various locations that are dependant on the refractive index and thickness of the specimen. As such, the S and D waves are spatially separated at the diffraction plane, enabling the phase of either the S or the D waves to be manipulated individually. A phase plate is positioned at the rear focal plane of the objective lens, which corresponds to

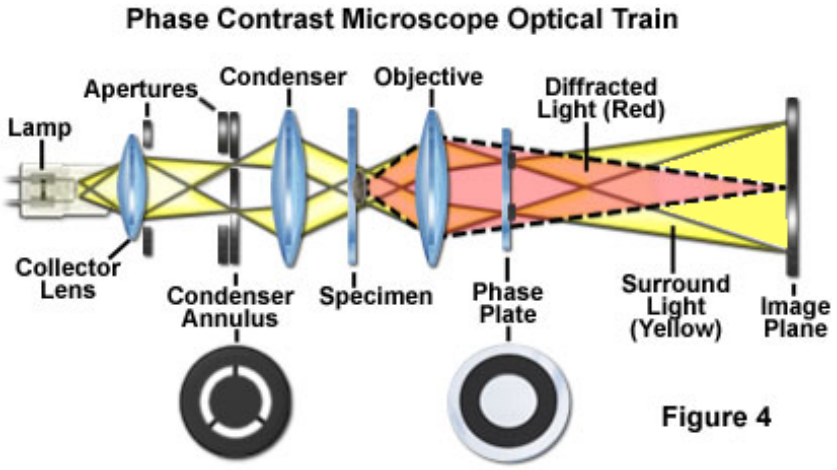

Figure 2.2: The diagram (from ref. (12)) illustrates the path of the undeviated surround (S waves) beams and the diffracted (D waves) beams as the illumination passes through a typical phase contrast microscope set-up.

the location at which the S waves are focused. The material of the phase plate is selected to advance the phase of the S waves by $\lambda/4$, which when combined with the phase of the D waves being retarded by $\lambda/4$, shifts the overall phase between the two wavefronts by $\lambda/2$, resulting in destructive interference at the image plane. In addition, the phase plate is typically darkened with a semitransparent metallic coating (1) which acts to reduce the amplitude of the S wave by approximately 70%. Therefore, the amplitude of the P waves, generated from the (destructive) interference between S and D waves, is significantly less than the S waves. In this way, a high contrast image is formed by converting the difference in phase, induced by a transparent specimen, into visibly detectable differences in light intensity, where specimens with a higher refractive index than the surrounding media appear dark against a lighter background and *vice versa*.

One drawback of phase contrast microscopy is that the phase contrast images exhibit phase halos, which surround phase objects (objects that induce a phase change in the illumination) and therefore can distort or mask features of interest in the specimen. These halos are inherent to phase contrast microscopy as they are produced by the presence of the phase ring, in which diffracted light from the specimen, at low spatial frequencies, passes through the annulus of the phase plate and is transmitted onto the image plane. However, the width of the ring of

undeviated S waves transmitted through the phase plate is smaller than the actual width of the annulus of the phase plate, therefore destructive interference of the transmitted diffracted waves is absent, which causes a localized contrast reversal (1) that appears as a halo around the phase object. Even so, for imaging certain transparent specimens, phase contrast microscopy is ideal due to the ease of set up as it only requires two components, a condenser annulus and a phase plate in order to convert a standard brightfield microscope into a phase contrast microscope.

2.4.2 Differential interference contrast (DIC) microscopy

Similar to phase contrast microscopy, differential interference contrast (DIC) microscopy enables transparent specimens to be visualised as high contrast images. The optical technique and principles for producing DIC images are very different to the phase contrast system, and also address some of the drawbacks of phase contrast microscopy. Primarily, DIC microscopy utilises dual-beam interference optics consisting of polarisers and Wollaston prism beamsplitters to convert local **gradients in optical path length** (13) in a specimen into a visibly detectable high contrast image (phase contrast microscopy converts **optical path differences** in a specimen into contrast differences in the image), where the image exhibits a pseudo 3-dimensional effect.

The optical path length is the product of the refractive index of the material n and the thickness t of the specimen in which the optical path traverses. Gradients in optical path length are created when a pair of beams traverse a phase object with a gradient in refractive index and/or thickness, resulting in an optical path difference between the two beams as they emerge from the specimen. The differential interference between the two beams as they recombine produces a high contrast pattern in terms of light intensity (amplitude) that represents the phase gradients in the specimen. A brief overview of the principles and optical set-up behind a DIC microscope will now be outlined.

In DIC microscopy, beam pairs are generated by passing partially coherent illumination (Köhler illumination) through a polarizer, and then through a Wollaston prism positioned at the front focal plane of the condenser lens, that splits the beam into two wavefronts which

are polarized perpendicularly to each other (14). The two wavefronts are referred to as the ordinary (O) and the extraordinary (E) rays, and are separated spatially by a distance that is less than the system resolution, which is termed as the shear (15). The wavefronts then pass through the specimen and are retarded by varying extents depending on variations in refractive index and thickness of the specimen. Subsequently, the light enters the second Wollaston prism, which is mounted close to the rear focal plane of the objective lens, whereby the two wavefronts recombine. If the two wavefronts exhibit gradients in the optical path length, the recombination of the wavefronts result in elliptically polarised light, otherwise the recombination results in linearly polarized light. Finally, the light passes into a second polarizer, which is referred to as the analyzer and is aligned to be cross polarised with respect to the first polarizer. The polarizer completely blocks linearly polarized light, resulting in an extinction of the background, whilst partially transmitting elliptically polarized light, resulting in a linearized component exhibiting a finite amplitude dependant on the differential phase retardations caused by the phase object (1). Figure 2.3 shows a diagram illustrating the beam path and optical set-up of a DIC microscope.

The major advantage of DIC microscopy over phase contrast microscopy is that the full aperture of the microscope is used, whereas in phase contrast microscopy the presence of the annulus restricts the aperture. This results in DIC images exhibiting higher resolution than phase contrast images (15), and also eliminates the phase halo caused by the annulus which is inherent to the phase contrast optical set-up. Furthermore, since the DIC technique assesses the phase gradient of the specimen, which accounts for differences in sample thickness and refractive index, thicker specimens can be imaged using DIC than when using phase contrast microscopy. On the other hand, a drawback of DIC microscopy is the qualitative nature of the images in terms of creating a 3-dimensional image, since the pseudo 3-dimensional effect is caused by the gradients in the optical path length, where the phase shift cannot be linearly related to the height of the phase object. As such, the heights/depths that are imaged cannot be used to measure the physical height of the specimen (1, 16).

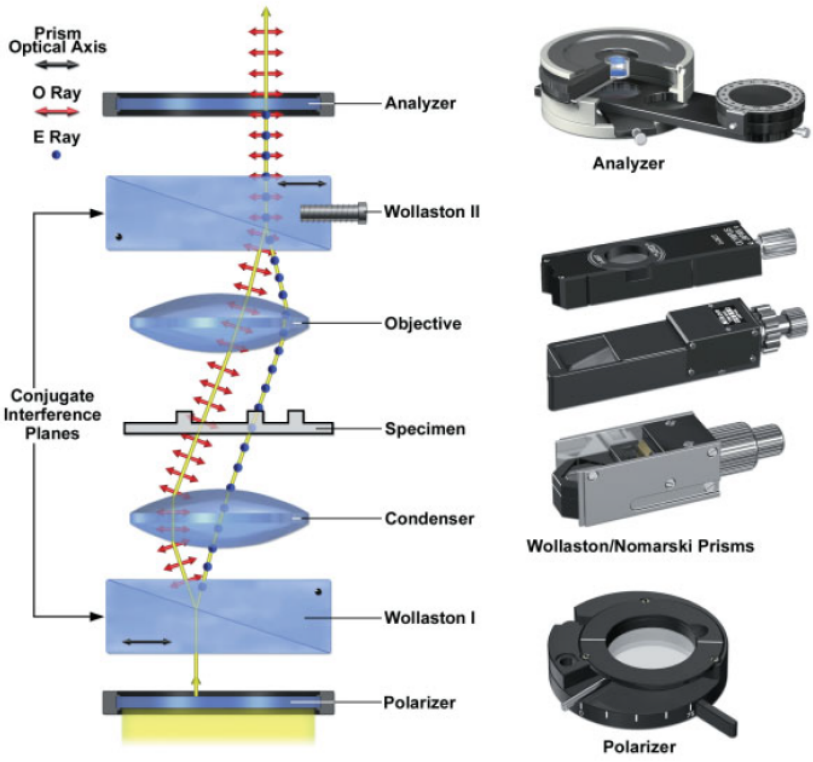

Figure 2.3: This diagram (from ref. (1)) illustrates the optical set-up of a DIC microscope, which consists of two polarizers (polarizer and analyser) and two Wollaston prisms. The path of the illuminated light is also illustrated.

2.5 Fluorescence microscopy

Fluorescence microscopy is a useful technique for imaging transparent specimens. Specific species or regions within a cell can be imaged by staining them with fluorescent dyes, and therefore specific biological or physical processes can be monitored. This section will give a brief overview of both single and two photon fluorescence, and will discuss some of the pros and cons of each technique.

2.5.1 Single photon fluorescence

When a fluorescent molecule absorbs a photon of an appropriate wavelength an electron is excited to a higher energy state. The transition back to the ground state causes emission of a photon (fluorescence) (17). A Jablonski diagram is shown in Figure 2.4 (1), which illustrates

the energy levels and electronic transitions of the excited fluorophore. The energy from the excited state can be released via three different pathways; fluorescence, as heat (internal conversion) or phosphorescence. There is a small probability that an electron in the first excited singlet state can transfer into the excited triplet state. Relaxation of an electron from the excited triplet state to the ground state can result in the emission of phosphorescent photons. The excited triplet state is chemically reactive, and can lead to photobleaching of the sample and production of free radicals which are damaging to cells.

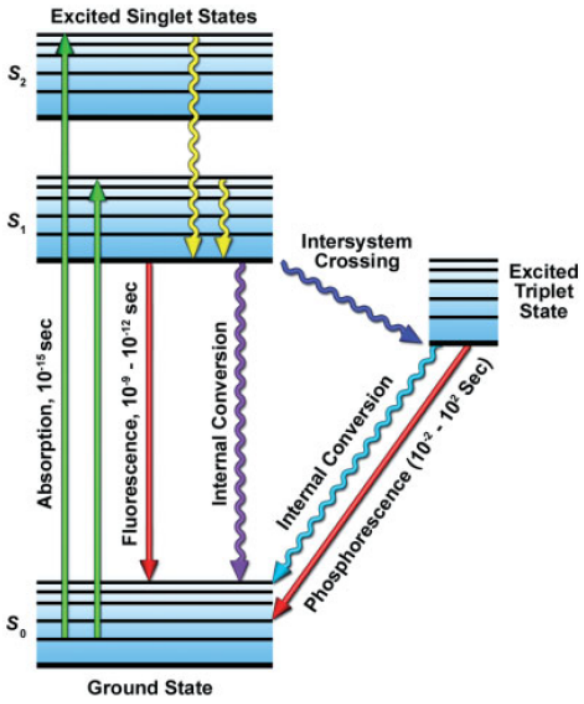

Figure 2.4: A Jablonski diagram (from ref. (1)) showing the energy levels and electronic transitions as the fluorescent molecule is excited. Energy from the excited state can be released via three pathways, fluorescence, heat radiation (internal conversion) or phosphorescence.

Fluorescence emission tends to be red shifted (Stokes shifted) in comparison to the absorption spectrum due to the fraction of absorbed energy that is lost by heat transfer to the surroundings (18). As such, the fluorescence emission can be isolated from the excitation light using appropriate band-pass filters to separate the excitation and emission wavelengths, enabling the fluorescence to be easily detected. This makes single photon fluorescence

microscopy a relatively simple imaging technique, as a standard microscope setup can be used, either with a laser excitation source or a mercury lamp with the appropriate excitation filters to illuminate the sample. Many fluorescent dyes that fluoresce at a range of wavelengths are commercially available, and also have the capabilities of binding to specific chemicals. This allows different organelles of interest to be labelled with different dyes so that by altering the emission filters, fluorescence at different wavelengths can be isolated and so a number of objects can be imaged within one cell. In addition, natural fluorophores such as Green Fluorescent Protein (GFP) (19) are widely available, which have the benefit of being relatively inert within living cells, and cells can also be genetically modified to express the fluorophore in order to fluoresce naturally (20, 21).

A major drawback with fluorescence microscopy is photobleaching, which is when a fluorophore is rendered permanently unable to fluoresce due to photon-induced chemical damage (17). The effects of photodamage can be reduced by limiting the illumination exposure time and intensity. This can be achieved by using neutral density filters, or using a confocal microscope set up. Another drawback is that standard single photon fluorescence microscopy can only image up to depths of approximately 10 μm for biological tissue samples (1), as excitation photons are scattered by the material resulting in weak excitation of the fluorophores. One method to overcome these issues is to use a confocal microscope set-up (22). A pin-hole is utilised to limit the light that illuminates and focuses onto the sample, whereby the reduction in light exposure helps to reduce the effects of photodamage and photobleaching. Optical sectioning is also a feature of confocal microscopy, as only the specimen at the focal plane will be imaged. The imaging depth for imaging biological samples is also increased (1). Even so, single photon fluorescence microscopy is not ideal for live cell imaging because the typical fluorophores require UV illumination, which damages cells. Two photon fluorescence (TPF) microscopy is a technique that addresses many of the drawbacks of single photon fluorescence.

2.5.2 Two-photon fluorescence microscopy

Two photon fluorescence is a two-photon process, whereby a fluorophore is excited when two photons of the same wavelength, with half of the required energy, are near-simultaneously absorbed, resulting in the emission of a single fluorescence photon. This fluorescence emission is equivalent to the single photon process (17).

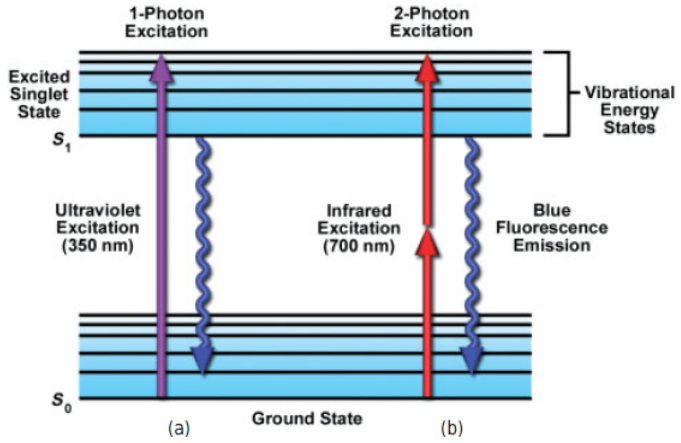

Figure 2.5: A Jablonski diagram (from ref. (1)) showing the energy levels and electronic transitions for single photon (a) and two photon fluorescence (b).

Two photon fluorescence (TPF) microscopy is a laser scanning technique that uses a pulsed near-infrared laser source to excite fluorescence. A pulsed laser source is required because two photon absorption (TPA) is a weak process in comparison to single photon absorption (SPA), which responds linearly to the illumination intensity. TPA only occurs when two photons randomly arrive at the fluorophore within a time window of 10^{-18} seconds (23), at which point excitation via a metastable state occurs. Since TPA requires two photons, stimulation to the excited state is proportional to the square of the light intensity. This makes the mechanism a second-order, nonlinear process (18), which is weak due to the unlikelihood of the event. High instantaneous laser power is required to increase the rate of TPA, which can be achieved by using an ultra-fast pulsed laser source, such as a Ti:Sapphire laser. A Jablonski diagram of the TPF mechanism is shown in Figure 2.5 (1), which illustrates the energy level transitions in the single photon and two photon mechanisms.

As mentioned in the previous section, drawbacks inherent with standard fluorescence microscopy include photobleaching, inability to focus into thicker tissues and the lack of optical sectioning. TPF microscopy counteracts these issues as it utilises a highly focused beam to localise the region of fluorescence. This enhances the resolution of the image (23), reduces the effects of photobleaching as only the region of focus is excited, and therefore results in 3-dimensional optical sectioning (17). The difference between the volume of excited fluorophores for the single photon and two photon process is illustrated in Figure 2.6. In addition, phototoxicity inherent with using a UV light source (which is typically used in single photon fluorescence) is avoided, as using near-IR illumination is less damaging to biological specimens than using UV illumination (1).

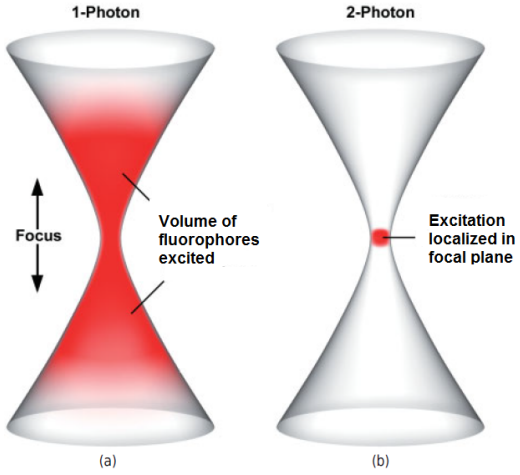

Figure 2.6: Illustration (from ref. (1)) showing the localization of excitation for the single photon (a) and two photon (b) process.

One consideration with TPF microscopy is that the technique is relatively high-cost in comparison with standard fluorescence microscopy. The optical set-up of TPF microscopy typically involves: an ultra-fast pulsed laser source, the ability to scan the laser across the sample such as using galvometric scanning mirrors, a photomultiplier tube (PMT) to detect the fluorescence emission, and an expensive objective lens. The objective lens must have a high numerical aperture to enable very tight focusing of the excitation light source at the sample, and also have very high light transmission and apochromatic correction that spans

across approximately 400 nm to 1000 nm (1), to allow both IR excitation and fluorescence emission to be transmitted. The optical set up used for the studies in this thesis is illustrated in Chapter 4.

To summarize, the capability of 3-dimensional sectioning of relatively thick samples at high resolution, as well as the ability to label and image specific specimens within a sample makes TPF microscopy a very attractive technique to use for biological studies. However, the presence of fluorescent labels will always pose the question: to what degree do the fluorophores perturb the living cell or biological process of interest? Consequently, the development of label-free, chemically selective microscopy techniques have been increasingly popular, for example the coherent anti-Stokes Raman scattering (CARS) microscope (24), which is a label-free imaging technique used in this thesis.

2.6 Coherent anti-Stokes Raman scattering (CARS) microscopy

Coherent anti-Stokes Raman scattering (CARS) is a four-wave mixing process, in which Raman transitions are strongly enhanced (18). In order to explain what is meant by a four-wave mixing process and subsequently discuss the CARS process, the basic principles of Raman scattering will first be reviewed, followed by an overview on non-linear Raman effects, in which the CARS mechanism and imaging technique will be discussed.

2.6.1 Raman scattering

Raman scattering is a two photon process, in which one photon is absorbed as another is emitted almost simultaneously (18). This inelastic scattering process results in an exchange of energy, whereby the frequency of the emitted photon is shifted according to the change in the molecule's vibrational state, known as Stokes and anti-Stokes scattering depending whether the molecule gains or loses vibrational energy to the photon respectively (25). The photon frequencies are,

$$\begin{aligned} &\text{Stokes} && \omega_s = \omega_0 - \omega_m \\ &\text{anti-Stokes} && \omega_{as} = \omega_0 + \omega_m \end{aligned} \tag{2.3}$$

where ω_0 is the frequency of the incident beam and ω_m is the vibrational frequency of the molecules. In this way, the Raman emission spectra probes the vibrational modes of the molecule, which consequently provide chemical information. The effect of Raman scattering is extremely weak, where only 1 in 10^5 photons of the incident beam undergoing Raman scattering (26). The majority of the photons are Rayleigh scattered, which is an elastic process, where the incident and emitted photon possess the same energy. Figure 2.7 shows the energy diagrams of Rayleigh and Raman scattering.

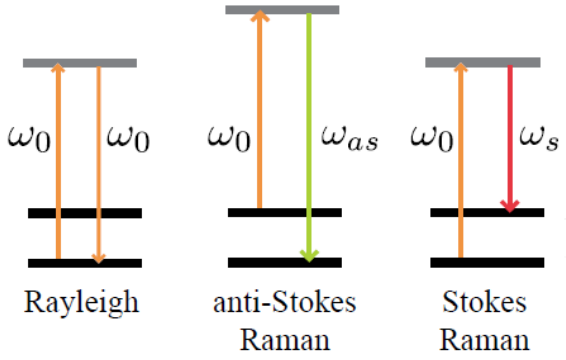

Figure 2.7: Energy diagrams showing Rayleigh scattering and Raman (Stokes and anti-Stokes) scattering (27).

The theory of Raman scattering can be explained using both a classical and quantum-mechanical treatment, as detailed by Ferraro et al. (25). For the purpose of this general overview, the classical treatment will be discussed and subsequently expanded to discuss the non-linear Raman effects.

The electric field strength (E) of the incident electromagnetic wave, fluctuating with time (t) is expressed as,

$$E = E_0 \cos 2\pi\omega_0 t \tag{2.4}$$

where E_0 is the vibrational amplitude and ω_0 is the frequency of the incident radiation. By first considering a diatomic molecule, if the molecule is irradiated with this light source, an electric dipole moment P will be induced, which is proportional to the applied field,

$$P = \alpha E = \alpha E_0 \cos 2\pi\omega_0 t \tag{2.5}$$

where α is the polarizability of the molecule, and is a proportionality constant, which depends on the vibrational displacement (nuclear displacement), q, of the molecule. Therefore, if the molecule vibrates with a frequency of ω_m, and a vibrational amplitude of q_0,

$$q = q_0 \cos 2\pi\omega_m t \tag{2.6}$$

For small displacements, α is a linear function of q, and can therefore be expressed to the first order,

$$\alpha = \alpha_0 + \left(\frac{\partial\alpha}{\partial q}\right)_0 q \tag{2.7}$$

where α_0 is the polarizability at the equilibrium position and $\left(\frac{\partial\alpha}{\partial q}\right)_0$ is the derivative of α with respect to q at the equilibrium position. By substituting Equations 2.6 and 2.7 into Equation 2.5 the following expression is reached,

$$P = \alpha_0 E_0 \cos 2\pi\omega_0 t + \frac{1}{2}\left(\frac{\partial\alpha}{\partial q}\right)_0 q_0 E_0 \left[\cos(2\pi(\omega_0 + \omega_m)t) + \cos(2\pi(\omega_0 - \omega_m)t)\right] \tag{2.8}$$

which is the first order time varying dipole moment representing an oscillating dipole that causes radiation at three distinct frequencies (25). The first term corresponds with Rayleigh scattered photons at frequency ω_0, and the second term corresponds with Raman scattered photons at frequencies $\omega_0 - \omega_m$ (Stokes) and $\omega_0 + \omega_m$ (anti-Stokes). Interestingly, it is clear that if $\left(\frac{\partial\alpha}{\partial q}\right)_0$ is zero, the vibration is not Raman active. This model is simplified to describe a diatomic molecule that vibrates in one-dimension. In reality, many molecular vibrations are

present and not only diatomic molecules are considered, in which case, α is a polarizability tensor (18).

The property of chemical selectivity makes the effect of Raman scattering desirable for label-free imaging, however as the Raman effect is very weak, Raman microscopy is not viable for live cell imaging as high intensity laser excitation is required (28). This issue can be avoided by considering the properties of resonant Raman scattering (18), whereby the intensity of both the Stokes and anti-Stokes scattering increases if the incident light falls within a molecular absorption band, and is the foundation of CARS miscroscopy.

2.6.2 Coherent Anti-Stokes Raman Scattering

CARS microscopy enables non-invasive intracellular imaging without the need for fluorescent labelling, due to the properties of enhanced signal and chemical selectivity inherent with resonant Raman techniques (29). CARS is a third-order non linear technique, whereby signal generation only occurs within the focal volume. As a result, CARS microscopy exhibits 3-dimensional optical sectioning and is capable of relatively deep tissue penetration (30).

The CARS mechanism is classically described as a parametric four-wave mixing process (30, 31), in which three fields, *pump*, *probe* and *Stokes*, with electric field amplitudes of E_p E_{pr} and E_s, and frequencies ω_p, ω_{pr} and ω_s respectively, are mixed at the sample to produce a fourth *anti-Stokes* (CARS) field E_{as} with frequency ω_{as}. Typically, the probe and the pump field are obtained from the same laser, therefore $\omega_{pr} = \omega_p$ (32). As such, the frequency of the CARS field can be determined as (32),

$$\omega_{as} = 2\omega_p - \omega_s \tag{2.9}$$

An energy diagram of the CARS process is shown in Figure 2.8, where Ω is the frequency difference between the pump and Stokes field, which is tuned to match the vibrational frequency of the Raman band of interest in order to produce the resonant enhanced CARS signal.

The term *coherent* in CARS simply means that photon emission from the excited molecules

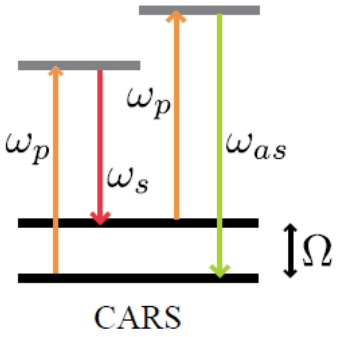

Figure 2.8: Energy diagram showing the CARS process (27).

across the region of the four-wave mixing process occurs coherently, as the pump and Stokes field drive all the resonant oscillators in the focal volume to oscillate at frequency Ω, with a well defined phase. In contrast, for spontaneous Raman scattering, the molecules within the region of illumination emit photons with random phases (18).

To explain parametric four-wave mixing, the classical theory of non-linear Raman scattering needs to be considered. In the previous section, the induced dipole moment was only expressed to the first order. The more accurate expression of the induced dipole moment is (25),

$$\begin{aligned} P &= P^{(1)} + P^{(2)} + P^{(3)} + \dots \\ &= \alpha E + \frac{1}{2}\beta E^2 + \frac{1}{6}\gamma E^3 + \dots \end{aligned} \tag{2.10}$$

where E is the electric field strength of the laser illumination, α is the polarizability, and β and γ are the first and second order hyperpolarizabilities respectively. For spontaneous Raman scattering, $\alpha \gg \beta \gg \gamma$ therefore the hyperpolarizabilities are negligible, however when the sample is irradiated with high powered laser pulses the contributions of β and γ become significant, resulting in non-linear Raman effects such as CARS. Equation 2.10 can be written in terms of the electric-field dependant susceptibilities, (E) (33),

$$P = E\chi(E) = \chi^{(1)}E + \chi^{(2)}E^2 + \chi^{(3)}E^3 + \dots \tag{2.11}$$

The CARS signal originates from the induced third-order polarization $P^{(3)}$ (32), and is

determined by the strength of the excitation fields E and the nonlinear susceptibility $\chi^{(3)}$,

$$P^{(3)} = \left(\chi_R^{(3)} + \chi_{NR}^{(3)}\right) E_p^2 E_s^* \tag{2.12}$$

where $\chi^{(3)}$ can be simplified by separating it into its resonant $\chi_R^{(3)}$ and nonresonant components $\chi_{NR}^{(3)}$ (34),

$$\chi^{(3)} = \chi_R^{(3)} + \chi_{NR}^{(3)} \tag{2.13}$$

$\chi_R^{(3)}$ is a complex quantity, where $\chi_R^{(3)} = \Re\left(\chi_R^{(3)}\right) + i\Im\left(\chi_{NR}^{(3)}\right)$, which represents the nuclear response of the molecules (30), as the $\chi^{(3)}$ term also leads to other third order processes (33). However, CARS becomes significant over the other effects when the resonant component, $\chi_R^{(3)}$, is excited with the Raman shift $\omega_p - \omega_s$ matching the Raman active molecular vibration.

Since CARS is a third order non-linear process, the intensity of the CARS signal, I_{as}, is proportional to the square modulus of the induced polarization,

$$I_{as} \propto |P^{(3)}|^2 \tag{2.14}$$

Solving the wave equation, assuming that the pump and Stokes fields are plane waves (27), means that the intensity can be expressed as,

$$I_{as} \propto |\chi^{(3)}|^2 I_p^2 I_s \left(\frac{\sin \frac{\Delta k z}{2}}{\frac{\Delta k z}{2}} \right)^2 \tag{2.15}$$

where z is the sample thickness and Δk is the wavevector phase mismatch (30). The phase matching condition is described by the following expression,

$$\Delta k = |\vec{k}_{as} - (2\vec{k}_p - \vec{k}_s)| \tag{2.16}$$

which depends on the propagation directions and frequencies of the pump, Stokes and CARS fields. This emphasises the importance of attaining tight focusing and phase matching of the

beams since the efficiency of the nonlinear CARS process is maximised when $\Delta k = 0$ (35).

By substituting Equation 2.13 into Equation 2.15, the proportionality of the CARS intensity to the modulus square of the total nonlinear susceptibility can be expressed as,

$$I_{as} \propto |\chi_R^{(3)} + \chi_{NR}^{(3)}|^2 \quad \propto \left(\chi_{NR}^{(3)}\right)^2 + |\chi_R^{(3)}|^2 + 2\chi_{NR}^{(3)} \Re\left(\chi_R^{(3)}\right) \tag{2.17}$$

where the first term is the nonresonant component that represents the electronic responses of the one and two photon electronic transitions, which are always present as background and are independent to the frequencies of the excitation. The second term describes the resonant components, which were discussed earlier and are dependent on the frequency difference between the pump and Stokes beams to match the Raman vibration. The third term represents the mixing of the nonresonant and the real part of the resonant Raman responses.

As mentioned previously, CARS microscopy enables the properties of chemical selectivity inherent with Raman scattering to be utilised for label-free imaging. Additionally, since the signal lies in the anti-Stokes region, it naturally discriminates from fluorescence signals (fluorescence typically lies within the Stokes shift region (25)). This enables the CARS signal to be easily isolated and detected, and also allows multi-modal imaging capabilities, for example, combining TPF and CARS microscopy techniques within the same system.

The main drawbacks of CARS microscopy are that the system is highly optically challenging and involves high costs, as the coherent nature of CARS means that a signal will only be generated if the four-wave mixing process occurs at both a temporal and spatial overlap at the sample, that results in constructive interference of all the molecular oscillators in the region of excitation. Another drawback is the non-resonant signal which is always present when CARS is generated. The issue with the non-resonant signal is that it contains no vibrational information and can overwhelm the CARS signal, especially if the sample is at low concentrations or when imaging weak Raman bands, since the CARS signal depends on the number of coherent oscillators that are excited. Polarization CARS and stimulated Raman scattering are techniques developed from CARS microscopy to minimise or eliminate the non-resonant background. Further information on these techniques can be found in

literature (36, 37)

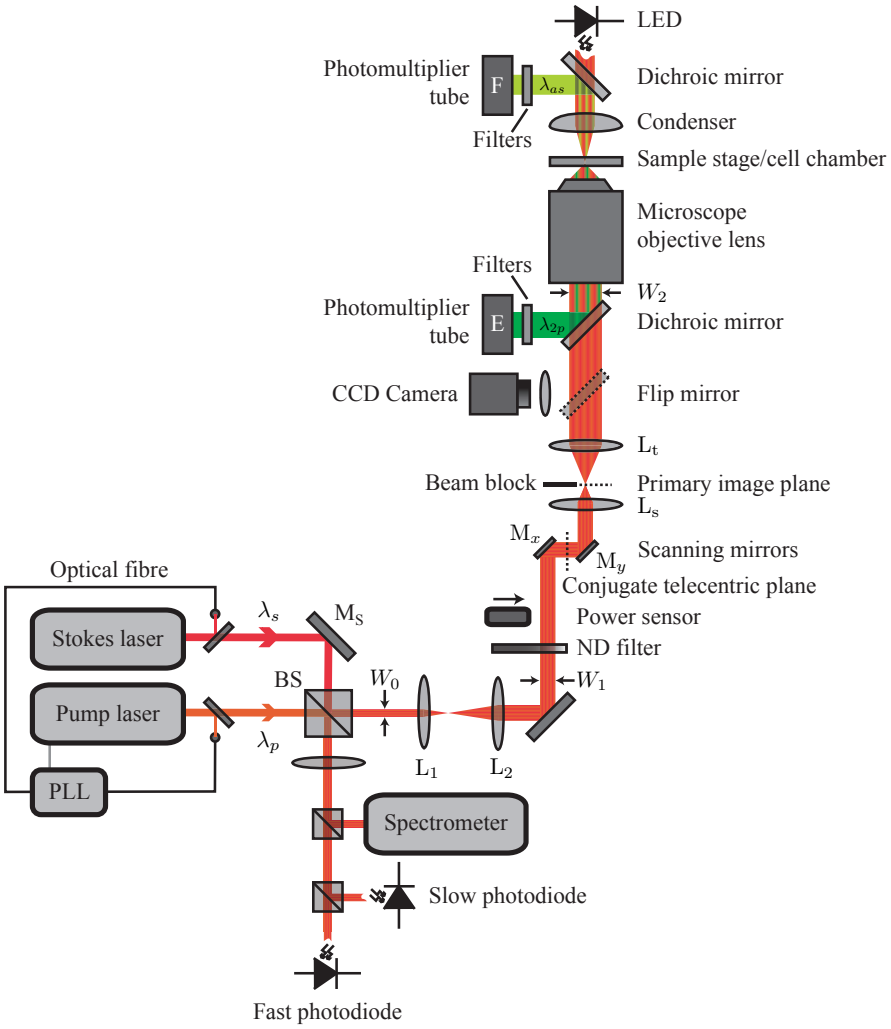

Figure 2.9: Diagram showing the CARS set-up.

The CARS system used for the studies in this thesis utilised two tunable Ti:Sapphire pulsed lasers, in which one laser was tuned to the pump frequency (ω_p) and the other was tuned to the Stokes frequency (ω_s) with pulse durations between 2-7 ps. Picosecond pulses were used rather than femtosecond pulses, which are typically associated with other nonlinear optic techniques such as TPF. Femtosecond pulses give a spectral width ($\approx$ 100 cm^{-1}) which is much wider than typical Raman vibrational linewidths (10 $-$ 20 cm^{-1}), resulting in much larger non-resonant signals that can overwhelm the CARS signal (38). Using pulses of 2-7 ps in duration corresponds to a spectral bandwidth of ($2-5$ cm^{-1}), which optimises the ratio

between resonant and non-resonant signal and maintains spectral resolution to give images with chemical contrast. The two laser beams are synchronised in phase using a phase-locked loop system (39) (Synchrolock, Coherent), which ensures that the synchronised pump and stokes photons arrive at the sample simultaneously. The optical set-up of this system is shown in Figure 2.9. Further information regarding the setup used for the studies in this thesis is detailed in Chapter 4, and full details of the system can be found in Iain Robinson's PhD thesis (27).

2.7 Conclusion

The basic theories and optical set-up of the imaging techniques presented in this chapter give some understanding as to the reasoning for using different microscopy techniques for the studies presented in this thesis. The use of various brightfield microscopy techniques, fluorescence microscopy techniques, and CARS microscopy facilitated the study of different biological systems, whereby the benefits of each system could be utilised, and the drawbacks of each system could be circumvented by using multiple techniques alongside each other whenever necessary. The combination of CARS and TPF microscopy is used to study the effects of mCMV on lipid droplets in fibroblast cells (Chapter 4), DIC microscopy is then used to further study the effects of mCMV infection on the lipid droplet dynamics (Chapter 5). Phase contrast microscopy, fluorescence microscopy and TPF microscopy are used to study giant unilamellar vesicles, synthesized to model Gram-negative bacteria membrane in order to study the effects of antimicrobial peptides on the membrane fluidity. The next chapter will give an overview on the biological systems that are studied in this thesis.

3

Cell biology

3.1 Introduction

The imaging techniques detailed in Chapter 2 were used to facilitate the studies on the effects of cytomegalovirus on lipid droplet dynamics in live fibroblast cells, and the effects of antimicrobial peptides on the fluidity of model bacterial membranes. This chapter will provide an overview of the biological specimens that were investigated, with a specific focus on the structure and function of lipid droplets in eukaryotic cells, and the membrane of bacterial cells, in addition to brief sections on cytomegalovirus and antimicrobial peptides. Since this thesis focuses on the physical effects rather than the biological effects, the discussion on biology will be highly selective, with the purpose to provide the necessary biological background to complement the physical analysis presented, and highlight the relevance of the studies.

3.2 Cell biology: eukaryotic and prokaryotic cells

Biological cells are classified into two categories, eukaryotic and prokaryotic, in which the main difference is that eukaryotic cells possess a cell nucleus containing its genetic material, whereas the genetic material is free within the cell of prokaryotes (40). Prokaryotic cells are structurally simpler than eukaryotic cells, and are more primitive, with fossil records

suggesting that prokaryotes pre-date eukaryotes by at least 2 billion years. Figure 3.1 illustrates the structure of the two different types of cells, and Table 3.1 highlights some factors that differentiate eukaryotic and prokaryotic cells. Typically, animal and plant cells are eukaryotic, such as the fibroblast cells studied in Chapters 4 and 5, and bacterial cells are prokaryotic.

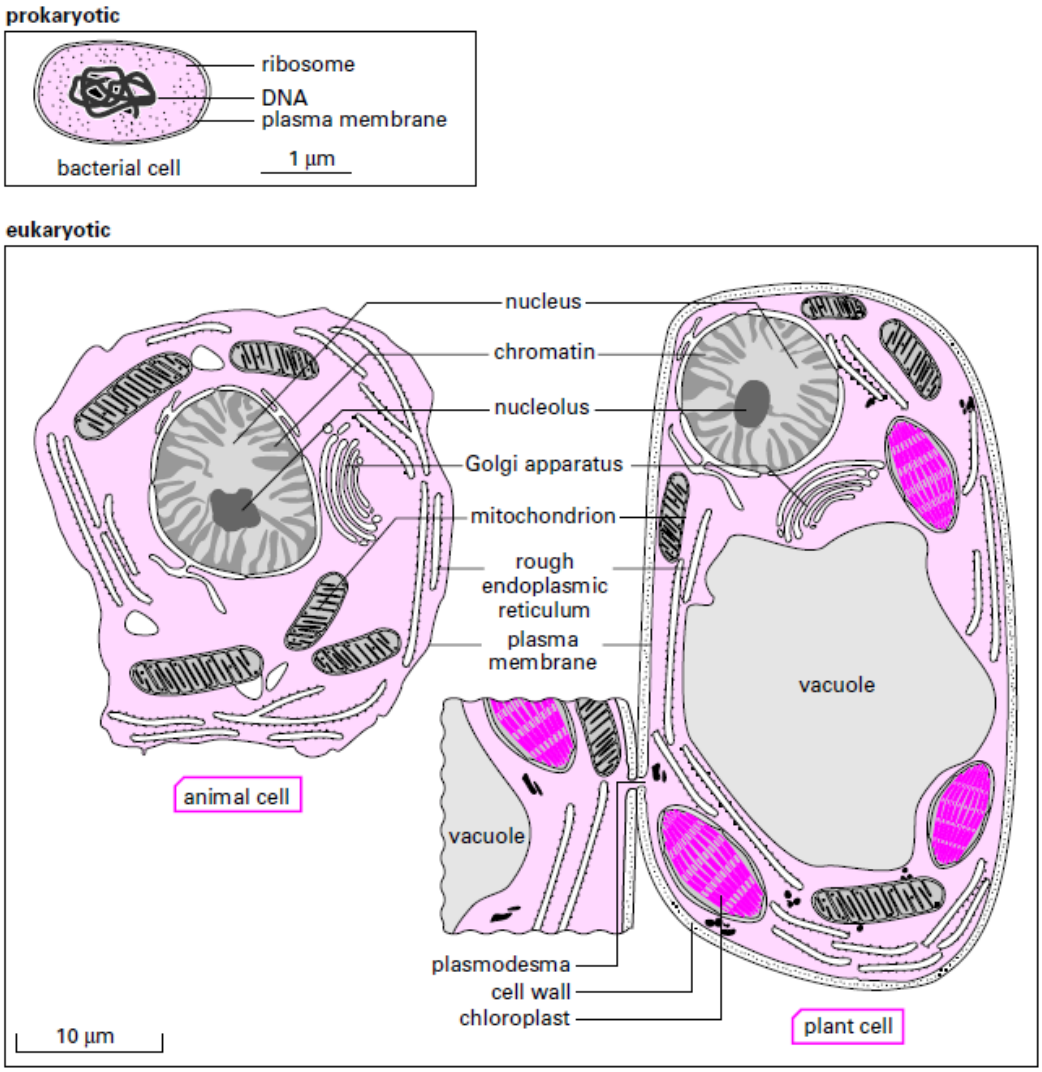

Figure 3.1: An illustration (from ref. (40)) of the structure of eukaryotic and prokaryotic cells.

	Prokaryotic	Eukaryotic
Typical size	$\approx 1-2$ µm	$\approx 5-100$ µm
Type of nucleus	No nucleus - nuclear body	Nucleus bounded by a nuclear envelope
DNA	usually a single circular molecule	Multiple, linear molecules (chromosomes) with associated proteins
Cell division	Binary (simple) fission	Mitosis (normal cell replication) and Meiosis (gamete production)
Internal membranes and structures	Rare, very few structures	Highly structured with membranes (nuclear envelope, organelles such as Golgi apparatus, mitochondria, endoplasmic reticulum) and cytoskeleton (microtubules, actin filaments)
Motility	Rotary motor driving bacterial flagellum	Cilia and more complex flagella

Table 3.1: Differences between prokaryotic and eukaryotic cells.

3.3 Prokaryotes: Bacteria

Bacterial cells are prokaryotes, of which there are many different types with a wide diversity of morphologies such as spherical (cocci), rod-shaped (bacilli), curved rod (vibrio), spiral shaped (spirilla) and tightly coiled (spirochaetes) (41). Although the majority of bacteria are not pathogenic, there are many that cause disease, infections or illness such as *E. Coli* O157:H7, which is the strain that causes severe (possibly fatal) food poisoning (42). As such, the ability to control infectious strains of bacteria is crucial, and is a major research focus (43, 44). It is known that bacteria adapt and evolve to counter external perturbations, such as environmental changes and antibiotics (45, 46); many theories and studies have found that the structure of the bacterial membrane, and its ability to dynamically adapt, plays a vital role in bacterial resilience (47).

3.3.1 Bacterial membranes

There are two major classes of bacteria, Gram-positive and Gram-negative, which are differentiated by the structure of the cell wall/membrane. Gram-positive bacteria, such as *Staphylococcus aureus*, have a thick cell wall (20-50 nm) that consists of several layers

of peptidoglycan, attached with teichoic acids, surrounding an inner cytoplasmic lipid membrane (48). Teichoic acids are polymers that bear a strong negative charge, and are covalently bonded to the peptidoglycan cell wall (41).

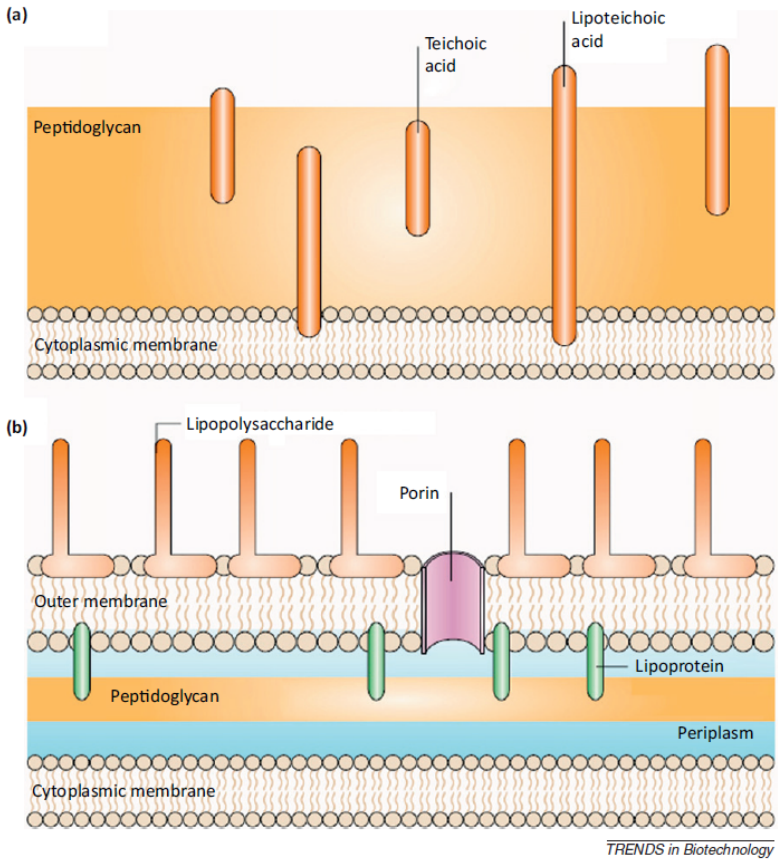

Figure 3.2: An illustration (from ref. (48)) of the structure of Gram positive (a) and Gram negative (b) bacterial membrane/cell wall.

Gram-negative bacteria, such as *Escherichia coli*, have a much more complex structure, which consists of an outer lipid membrane with lipopolysaccharide molecules attached to it, surrounding a very thin (2 nm) peptidoglycan layer, and an inner cytoplasmic lipid membrane. The lipid membranes typically consist of a mixture of zwitterionic and anionic phospholipids, with approximately 25% being anionic (49). The structure of Gram-positive and Gram-negative bacterial cell wall/membrane is illustrated in Figure 3.2 (48).

The bacterial cell wall acts to provide rigidity, strength and shape to the cell, and protects the cell from osmotic rupture and mechanical damage. Therefore, Gram-positive bacteria tend

to be more resilient to environmental stresses. On the other hand, the lipopolysaccharide outer membrane tend to confer resistance to detergents and chemical environments. Of course, this is highly generalised, as the susceptibility of bacteria to antimicrobial agents are also dependent on how the agent can bind to and penetrate the membrane/cell wall (48, 50)

3.3.2 Antimicrobial peptides

Antimicrobial peptides (AMPs) are small peptides which range in size from around 15 to 34 amino acids (51, 52), and are natural antimicrobial agents produced by the epithelial surfaces of the host to kill infectious micro-organisms. The development of AMPs and the understanding of how they interact with bacterial membranes is currently a major research focus because current antibiotics are losing effectiveness against bacterial infections, as over time bacteria evolve resilience to antibiotics (53, 54). The interest in AMPs stems from the possibility that bacteria may not be able to evolve a resilience against these agents, since AMPs have remained effective for millions of years in humans and animals (53).

The peptides tend to possess a cationic region and a hydrophobic region where electrostatic attraction between the cationic region of the AMP and anionic bacterial membranes leads to an initial interaction. It is generally understood that AMPs undergo what is known as *self-promoted uptake* in order to penetrate the outer membrane and cell wall, which is then followed by disruption of the inner membrane (55, 56). Self-promoted uptake is when the cationic compound of the AMP displaces the cation bridge that is present between adjacent lipopolysaccharides, causing a local perturbation to the outer membrane which allows the cationic part of the AMP to be taken up by the membrane (57). As such, the initial interaction between different AMPs and bacteria is non-specific. However, for the AMP to penetrate or disrupt the inner, cytoplasmic membrane, the hydrophobic section of the AMP must interact and bind with the membrane. This depends on the specificity and design of the peptide (52), where the amphipathic structure causes the AMPs to adopt specific conformations which allows the peptide to penetrate the membrane (54). Most current theories assume that for antimicrobial peptides to kill bacteria effectively, they must disrupt the bacterial cytoplasmic membrane. The

precise mechanisms of how AMPs disrupt the membrane are currently unknown, and are most likely to vary with the peptide, however there are many studies that suggest the main modes of disruption include pore formation or a carpet mechanism (54, 58, 59).

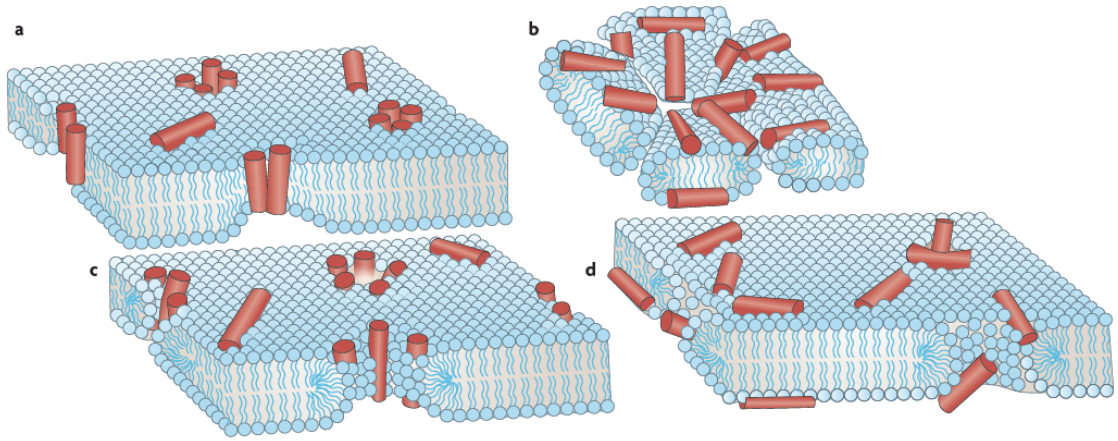

Figure 3.3: An illustration (from ref. (54)) of pore formation; Barrel-stave pores, where AMPs insert perpendicularly in the bilayer (a), carpet mechanism, where peptides bind parallel to the membrane bilayer, and disintegrates the membrane via a detergent-like effect when they reach sufficient coverage (b), toroidal pore formation, where AMPs insert perpendicularly but induce local membrane curvature (c), and Disordered toroidal pore formation, where AMPs insert as they would in a toroidal pore formaion but with less rigid peptide conformations and orientations (d).

Figure 3.3 illustrates the proposed methods of AMP interactions at the membrane surface, where for a specific AMP, the mode of interaction may vary depending on the membrane environment (51). There are three suggested mechanisms of pore formation: barrel-stave, toroidal and disordered toroidal (51, 54, 60). In the barrel-stave mechanism, the AMPs position around an aqueous pore in a barrel-like ring. The initial step of barrel-stave pore formation involves peptide binding at the membrane surface. The peptide then undergoes a conformational transition which forces the polar headgroups of the membrane lipids aside, thinning the membrane. The hydrophobic portion of the peptide then inserts perpendicularly into the membrane and self-assembles into barrel shaped aggregates if the AMP concentration is sufficient. Continued aggregation further expands the membrane pore. Formation of a toroidal pore is similar to the formation of a barrel-stave pore, in that the AMPs insert perpendicularly into the membrane in a similar way. The primary difference between the two

mechanisms is that for toroidal pore formation, the peptides adopt an α-helical conformation as they interact with the bacterial membrane. The α-helical peptide induces local curvature onto the membrane as the hydrophobic region of the bound peptide displaces the polar headgroups of the lipid bilayer, creating a positive curvature strain in the bilayer, forming a toroidal shaped pore. If the peptide conformation and orientation is less rigid and structured, the interaction is then regarded as disordered toroidal pore formation. In the carpet model, a high density of peptides accumulate on the surface of the membrane, binding parallel to the bilayer. At low AMP concentrations, the membrane is not affected, however at high concentrations, the orientation and attachment of the peptides destabilizes the phospholipid packing, altering its fluidity, leading to a loss of membrane integrity and concomitant disruption. It is unclear whether pore formation also results in a detectable change in membrane fluidity. Bacterial membranes are known to maintain an optimal state of membrane fluidity in order to counteract environmental stresses (45). As such, it is interesting to consider whether AMP perturbations of bacterial membrane can be detected as significant changes in fluidity.

3.3.3 Model bacterial membranes

As mentioned, Gram-negative bacterial membranes are highly complex, so it can be beneficial to first study the interactions between AMPs and simple model membranes. This section will briefly discuss the feasibility of using simple model membranes to study the physical interactions of AMPs.

Since it is generally believed that the penetration into the outer membrane occurs via self-promoted uptake, the interest is then do determine how the AMPs penetrate the inner cytoplasmic membrane. The cytoplasmic membrane is known to comprise an approximate 3:1 mixture of zwitterionic and anionic phospholipids, where the primary zwitterionic phospholipid has been identified as Phosphatidylethanolamine (PE) and the primary anionic phospholipid as phosphatidylglycerol (PG) (61). In addition to the phospholipids are various proteins that sit within the lipid bilayer. As such, many studies have used a simplified model membrane formed using only phospholipids, such as using DOPC:DPPG phospholipid mixtures (62) or

POPC:POPG phospholipid mixtures (59), with various bilayer conformations being studied, including flat bilayers, giant unilamellar vesicles and large unilamellar vesicles.

3.3.4 Phospholipids and lipid phases

Phospholipids are amphipathic molecules, with a polar head group and two hydrophobic hydrocarbon tails (63). The most common phospholipids are phosphaltidylcholine (PC), phosphatidylethanolamine (PE), phosphotidylserine (PS), phosphatidic acid (PA) and phosphatidylglycerol (PG). Typically, the tails are between 14-20 carbons in length, where one tail is fully saturated, and the other can either be saturated or consist of one or more double bonds. The degree of saturation affects the main transition temperature (T_m) of the lipids, which is the temperature that the lipids transition from gel phase to liquid crystalline phase, where lipids with fully saturated hydrocarbon tails have higher T_m than lipids consisting of unsaturated hydrocarbon tails. Examples of phospholipids are shown in Figure 3.4, which shows the chemical structure of 1,2-dipalmitoyl-sn-glycero-3-phosphoethanolamine (DPPE), 1,2-dipalmitoyl-sn-glycero-3-phosphocholine (DPPC) and 1-palmitoyl-2-oleoyl-sn-glycero-3-phospho-(1'-rac-glycerol) (sodium salt) (POPG).

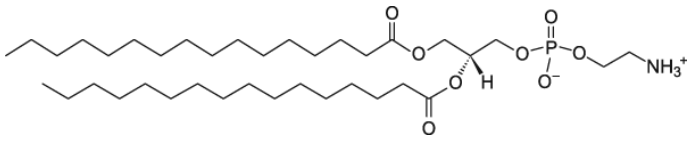

(a)

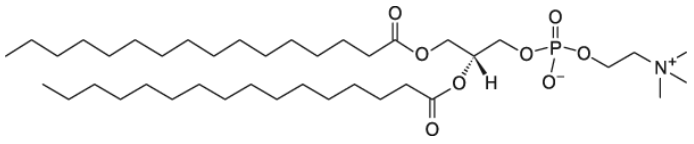

(b)

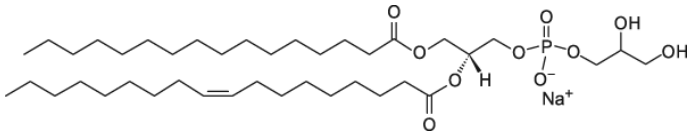

(c)

Figure 3.4: The chemical structure of DPPE (a), DPPC (b) and POPG (c).

3.4 Eukaryotes: Fibroblasts

There are many different types of eukaryotic cells, which together form multicellular organisms where different groups of cells have specific functions within an organism. Focusing on animal cells, there are four major types of tissue: epithelium (skin cells, lung and intestinal lining), connective tissue (bone, cartilage, fibroblasts, macrophages), nervous tissue (neurons, glia), and muscle (40).

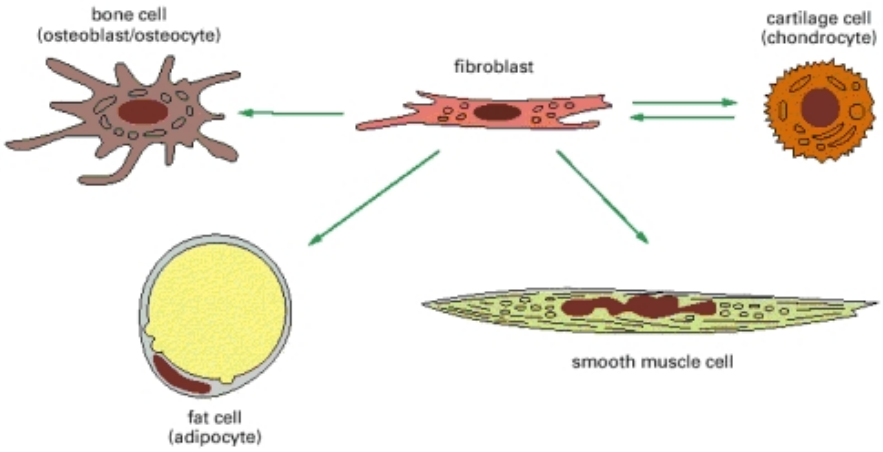

Figure 3.5: An illustration (from ref. (64)) showing the versatility of fibroblasts, indicating the different types of connective tissue that fibroblasts can transform into.

Fibroblast cells are the least specialised of the cells in the connective tissue family and are highly versatile (64). The cells are dispersed in the connective tissue throughout the body and play an important role in the maintenance and regulation of the extracellular matrix, healing muscle and tissue injuries, and regulating fluid volume and pressure of tissues (65). Some classes of fibroblasts are able to transform into other types of connective tissue, such as bone or skin cells depending on the composition of the surrounding extracellular matrix, as illustrated in Figure 3.5.

The NIH/3T3 cell line (66) was used for the experiments in this thesis. This cell line of fibroblasts originates from an albino Swiss mouse embryo, and was established in the early 1960s by George Todaro and Howard Green.

3.5 Intracellular Lipid droplets

Lipid droplets are intracellular storage organelles (67), which reside within the cellular cytoplasm of cells. The droplets tend to be between 0.1 µm to 2 µm (67) depending on the type of cell they reside in, and are composed of a hydrophobic core of triglycerides and cholesteryl esters, with a phospholipid membrane surrounding the core, in which structural proteins such as perilipin cover approximately 15% of the membrane surface (68). Figure 3.6 shows an illustration of the structure of lipid droplets.

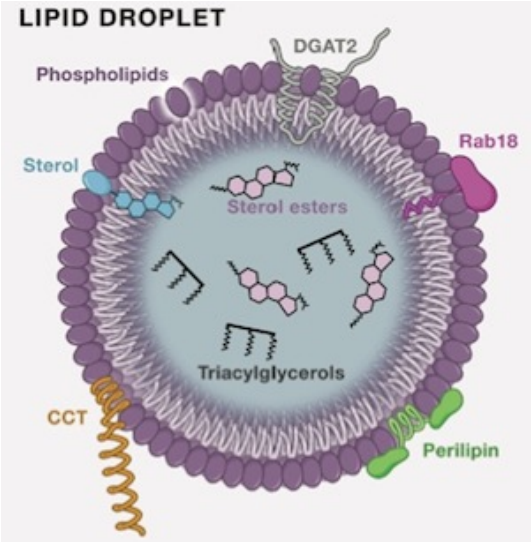

Figure 3.6: An illustration (69) of the structure of lipid droplets.

Historically, it was thought that lipid droplets were inert aggregations of neutral lipids, however recent investigations have found that lipid droplets are dynamic organelles that participate actively in cellular activities. For example, lipid droplets have been found to participate in safe processing of (toxic) protein aggregates (70), in which cellular lipid droplets provide surfaces that allows large amphipathic proteins to attach, preventing the proteins from forming toxic aggregations.

Lipid droplets are highly mobile organelles (71), and are actively transported around the cell by molecular motors. There are three different classes of molecular motors: myosin, kinesin, and dynein, which operate along two intracellular transport networks known as

the microtubule network and the actin network (cytoskeleton). The microtubule network is polarized, with the plus end towards the cell periphery and the minus end towards the nucleus, whereas the actin network can be randomly orientated (72). Myosin motors move along actin filaments, kinesin motors move towards the plus end of the microtubules, and dynein motors move towards the minus end. In this way, lipid droplets undergo bi-directional movement, dependant on the driving motor (73, 74).

3.6 Viruses

Viruses are submicroscopic particles that comprise a core of genetic material enclosed within a protein capsid. Some viruses also possess an outer glycoprotein membrane that envelopes the viral capsid (40, 75). Although they contain genetic material, they rely on the host cell to replicate the genetic material and to produce viral proteins. As such, viral particles are metabolically inert until they enter a host cell.

Viruses are classified depending on morphology, chemical composition and structure of the genome, and the mode of replication (41). The different morphologies of the viral capsids include helical, in which the capsid proteins (protomers) are wrapped around a spiral filament of nucleic acid, and icosahedral, in which the capsid forms an icosahedral structure that surrounds the viral genome. The viral genome may either be DNA or RNA, with a structure that is single stranded, double stranded, linear or circular, where the type of genome determines the mode of replication.

3.6.1 Pathogenicity

Viral pathogenicity is the capability of the pathogen to cause disease. Pathogenicity depends on many factors including the capacity to penetrate the host cell, to replicate within the host, to transmit between host cells and also to evade the host immune system (76). Viruses with a low ability to harm or infect the host are termed non-pathogenic or poorly-pathogenic. In general, the host recovers from pathogenic infections by eliminating the virus, regardless of the pathogenicity.

The ease with which the outer layer of the virus binds to the outer membrane of the host cell is an essential factor in determining the viral pathogenicity (76). In order for many macromolecular substances to pass through the cellular membrane, the macromolecule must be recognised by receptors that are situated throughout the membrane. This process is called receptor-mediated endocytosis, which is the selective uptake of macromolecules into the cell via successful ligand binding (77), which allows low concentrations of macromolecules, to pass through the cellular membrane. By mimicking the ligands that are recognised by the cell receptors, the virus is able to gain entry into the cell.

3.6.2 Lipid droplets and viruses

Lipid droplets have also been identified to be involved in viral infections. For example, it was discovered that lipid droplets are appropriated by certain viruses, such as the hepatitis C virus (HCV), and form part of the infection cycle (78–81). It has been found that HCV core viral proteins associate with the droplets, and that failure of the core proteins to attach to the lipid droplets results in low production of viral progeny (82). However, a full understanding of the precise purpose of viral core protein attachment to the lipid droplets as part of the HCV life cycle is still a subject of ongoing research.

Other viruses such as cytomegalovirus have been suggested to perturb the lipid metabolism in the infected cells (83), in particular by affecting the sterol metabolic pathway that regulates the sterols. Studies have also found potential links between CMV infection and lipid droplet accumulations (84) with evidence of a link between CMV infection and high levels of low-density lipoprotein (LDL) cholesterol, and high levels of cholesterol ester deposits on arterial walls (85). However, as of now, there have been no direct studies of how CMV are involved with lipid droplets, and no studies have investigated how the dynamics, arrangement and/or accumulation of the lipid droplets are influenced by the virus.

3.6.3 Cytomegalovirus

Herpesviridae is a double-stranded DNA virus comprising three subfamilies: *alphaherpesvirinae*, *betaherpesvirinae*, and *gammaherpesvirinae*. Cytomegalovirus belongs to the *betaherpesvirinae* classification, where the human form (HCMV) is a wide spread pathogen that infects the majority of the world's population. Infection symptoms are typically mild, such as cold sores, however in individuals with compromised immune systems such as organ transplant or AIDS patients, the infection can become fatal, and can affect the central nervous system (41, 86). An infected host is infected for life as the virus is capable of evading the host immune responses, either by becoming dormant, or by exhibiting mild activity without rapidly killing or excessively damaging host cells. In this state, the virus is described as having established a viral persistent state, or a viral latency state. Understanding the behaviour of cytomegalovirus is important for permanent elimination of the virus from the host. The studies presented in Chapter 4 and 5 uses murine-cytomegalovirus (mCMV), which is the mouse variant of CMV to study the effects of CMV and host-cell lipid droplets. HCMV and mCMV both belong in the same group and therefore express similarities between the replication characteristics and disease syndromes (41, 76), and since herpesviridae is species specific (will not infect across species) using mCMV to model HCMV is practically more desirable.

Cytomegalovirus has a four-layered structure, which is illustrated in Figure 3.7. The core of the virus is a double-stranded DNA genome enclosed within an icosapentahedral capsid. The viral capsid is surrounded by the tegument, which consists of amorphous proteins. Encasing this is a glycoprotein-bearing lipid bilayer envelope.

The glycoprotein membrane layer enables the virus to penetrate the host cell membrane as the complexes interact with the cellular receptors of the host by mimicking the correct ligands required for the host cell to recognise the molecule. In this way, the host cell will bind to the outer protein layer of the virus allowing endocytosis of the viral capsid. Once the capsid is within the cell, it transports viral DNA into the host cell nucleus where DNA replication begins. The tegument plays an important role by acting to conceal the virus from the host's

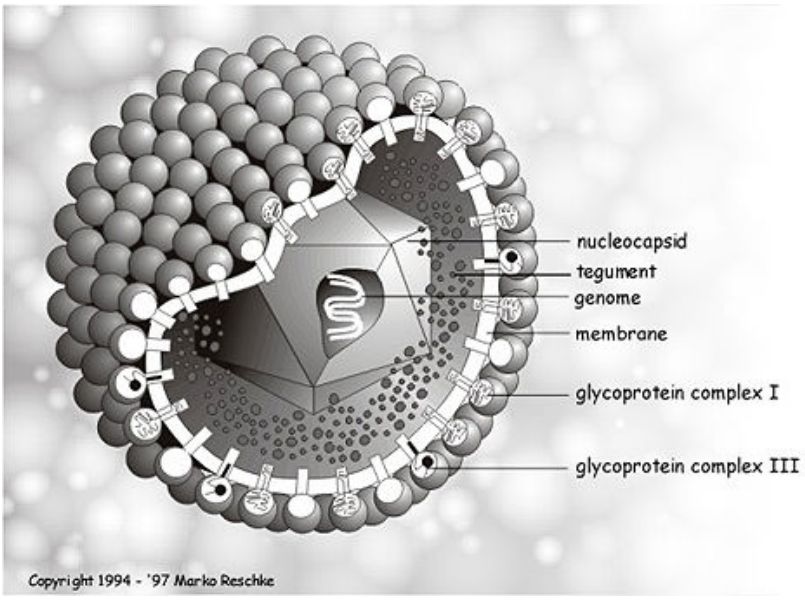

Figure 3.7: An illustration depicting the basic structure of human cytomegalovirus (87).

immune system, and the protein capsid protects the viral DNA enroute to the host cell nucleus, where DNA replication begins (88).

3.7 Conclusion

This chapter gives an overview of the basic biology of the specimens studied in this thesis, where the distinctions between eukaryotic (fibroblasts) and prokaryotic (bacteria) were highlighted. The function and structure of intracellular lipid droplets, bacterial membrane and cytomegalovirus were also reviewed, and the motivation for studying these specimens was discussed. The underlying theme is that in order to control pathogenic bacteria and viruses, a full understanding on the interaction between the pathogen and the host is crucial, which includes understanding how the pathogen infects the host, in addition to understanding the physical effects of host-pathogen interactions. The subsequent chapters will present the studies on host-pathogen interactions, where Chapters 4 and 5 presents the investigation on the physical effects of cytomegalovirus on lipid droplets in host fibroblast cells, and Chapter 6 presents the investigation on whether antimicrobial peptides affect the fluidity of model bacterial membranes.

Part 1

Study on lipid droplets in live mCMV infected cells

4

Multimodel imaging of mCMV infected fibroblast cells

4.1 Introduction

Many studies have shown a link between certain viral infections and intracellular lipid droplets. In particular, for hepatitis C virus (HCV), it was found that core viral proteins tend to interact with lipid droplets following disassembly of the proteins from the capsid within the host cell (84, 89, 90). Other viruses such as cytomegalovirus (CMV) have also been linked to intracellular lipid droplets, with studies finding potential links between CMV and lipid droplet accumulations (84). In addition, high levels of LDL cholesterol and high levels of cholesterol ester deposits on arterial walls have also been linked to CMV infection (85). However, the way in which the virus interacts with, and influences lipid droplets is currently unknown. It is unclear how CMV are involved with lipid droplet accumulations and no study has been done to determine whether the dynamics and arrangement of the lipid droplets are influenced by the virus.

In this chapter a study on host-pathogen interactions in live cells will be presented. Far-field microscopy techniques have been used to image the consequences of murine cytomegalovirus (mCMV) infection in mouse fibroblast cells. In particular, a multimodal microscope platform

combining coherent anti-Stokes Raman scattering (CARS) and two-photon fluorescence (TPF) was used to examine the correlation between cytomegaloviral infection and the behaviour of host cellular lipid droplets. CARS microscopy is a label-free imaging technique, which thereby minimises perturbation of biological systems making it the ideal technique for studying lipid droplet behaviour *in vivo*. The mechanism for generating a CARS signal is based on the ability to target a specific resonance band of the chemical species of interest. By targeting the resonance band of the aliphatic chain (CH_2), lipid droplets in live cells were imaged throughout the course of infection without the need for fluorescence labelling. TPF microscopy was used alongside CARS in order to probe the progression of infection. In this way, the observed lipid droplet behaviour was correlated to the progression of the infection.

4.2 Background

Lipid droplets are mainly thought to be a store for energy, and membrane building blocks (91). More recently, lipid droplets have been identified to be involved in viral infections. For example, it was discovered that lipid droplets were appropriated by certain viruses, such as the hepatitis C virus, during the infection cycle (78–81). In addition, viruses such as cytomegalovirus have been suggested to perturb the lipid metabolism in the infected cells (83).

CARS microscopy is widely used for imaging cellular lipid droplets (24, 92) and as explained earlier, the technique is a valuable tool for studying the link between lipid droplets and viral infection. However, CARS alone is insufficient for identifying the infection state of cells. To facilitate this, a genetically modified strain of mCMV that expresses green fluorescent protein (GFP) (19, 93) was used in this experiment. This particular strain causes the host cell to express GFP under the control of the immediate-early promoter 3 gene (94), so as soon as viral mRNA is translated in the host cell, the host will express GFP in parallel. An advantage of using this strain of mCMV is that the modified genetic code will persist in the DNA of the viral progeny, therefore subsequent infections of the progeny will also cause its host to express GFP. As a result, continuous monitoring of GFP in the infected cells is possible for an extended time period after the initial infection. This method avoids the problems of toxicity, changes to

cellular function and issues regarding loss of fluorophore with time that is inherent with usual fluorescent labelling techniques (95).

In a previous study by Robinson et al. (95) CARS and TPF imaging were combined to compare fixed samples of healthy (uninfected) and mCMV infected mouse fibroblast cells. The results showed that morphological changes such as expansion of the cell nucleus and an apparent rearrangement of intracellular lipid droplets occurred due to viral infection. However, the study only compared uninfected cell samples with samples that were incubated with mCMV for two to three days, therefore any changes occurring between those time points were not observed.

The aim of the study reported in this chapter was to use CARS/TPF microscopy and adapt the system to sustain live cell imaging. Then by imaging live fibroblast cells infected with mCMV, intracellular changes resulting from the viral infection were assessed. In particular, the focus was to quantify and assess the observed changes from CARS/TPF images in order to investigate how lipid droplet configuration changes within the cell during infection.

4.3 Method

The first step was to ensure that the system was capable of sustaining live cells over several days and that the cells survive laser scanning. This was paramount for the study because in order to assess cellular changes in live cells during the full course of infection, the sample would need to be imaged over several days. The next step was to identify changes in the cellular features which are characteristic to a particular time post infection so that specific stages of infection can be identified and defined. This is essential for live cell samples because the infection and incubation method used allowed uninfected cells to continue to replicate, resulting in the potential of neighbouring cells to be at different stages of infection within the same cell population. Therefore, by being able to identify and distinguish specific stages of infection, changes in lipid droplet configuration can be linked to specific time points as infection progresses.

4.3.1 Sample preparation

Sample preparation and viral infection was done by Michael Ochsenkühn, and the method used is described in detail in the paper by Robinson et. al. (95). Briefly, NIH/3T3 fibroblast cells with a passage number[1] in the range 11–20 were cultured in Dulbecco's modified Eagle's medium (DMEM), with L-glutamine (200 mol/m^3), penicillin/streptomycin (10 000 units/ml) and 10 % calf serum. Standard growth conditions of 37 °C and a 5 % CO_2 environment were maintained during an incubation period of 12 hours. Cells were seeded onto glass-bottom Petri dishes (P35Gcol-1.0-14-C, MatTec). Infection with mCMV wildtype mutant C3X was carried out using a genetically modified version of the Smith strain (94) at a multiplicity of infection (MOI) of 1, with the growth media containing only 3 % calf serum.

Fixed cell samples were used to produce a profile to characterise infection. The cells were produced in the same way as above, except that the cells were seeded onto glass coverslips and fixed using 1 % formaldehyde in phosphate buffered saline. By using the synchronization transfection method (96) a range of samples were fixed at known time points between 0 and 96 hours post transfection (hpt). The synchronized transfection method ensures that every cell in the sample is at the same infection stage. Therefore each coverslip contained large numbers of cells fixed at the same time (hpt) in the infection cycle.

4.3.2 Instrumentation

4.3.2.1 Live cell chamber

A portable cell chamber was built to provide a suitable environment for sustaining live cells on the microscope stage. The chamber was designed to attach directly onto the microscope, as shown in Figure 4.1. Since the function of the chamber was to sustain a stable population of living cells, access for passaging or perfusion was not required. Therefore, the chamber was designed to be airtight, to maintain a 5 % CO_2 atmosphere, and to provide a controlled temperature of 37.0 °C (97). The top window of the chamber was designed to touch the growth

[1]The passage number is the number of times a cell population has been removed from the culture flask and passaged, which is when the cell population is subcultured at a low population density to stimulate further growth.

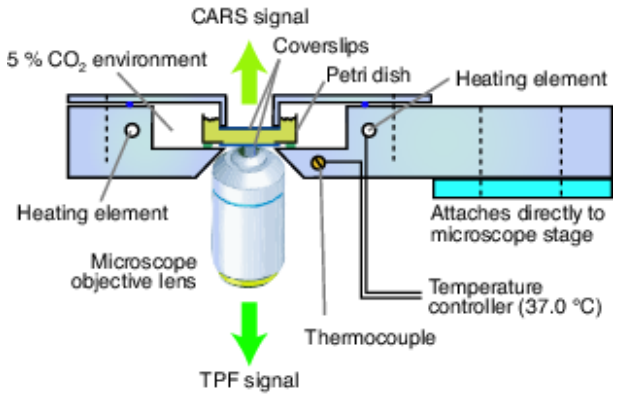

Figure 4.1: Portable cell chamber for live cell imaging. A glass-bottom Petri dish containing the cell sample is sealed into the chamber in a 5 % CO_2 environment. The aluminium chamber body is fitted with heating elements and connected to a temperature controller which maintains a constant temperature of 37.0 °C. The chamber attaches directly to the stage of the (custom-built) microscope.

media in order to minimize signal loss due to refraction/reflection and to prevent the formation of condensation on the glass. This set-up enabled live cells to survive on the microscope for at least 7 days, which was verified by observing a gradual growth in cell population from the initial 50–70 % to 100 % confluence[2] over the period. A phenol-red indicator confirmed that neutral pH was maintained, suggesting that the CO_2 concentration remained constant inside the chamber (98, 99). As cytomegalovirus completes its replication cycle after 72 hours at most (100), the longevity of cells in the chamber is more than sufficient for the process being investigated.

4.3.2.2 Multimodal CARS/TPF microscope setup

A custom-built laser-scanning inverted CARS microscope setup (95, 101), shown in Figure 4.2, was used to record both CARS and TPF images simultaneously. The laser source was a pair of titanium-sapphire lasers (Mira 900, Coherent), which were mode-locked and synchronized via a phase-locked loop system (39) (Synchrolock, Coherent). The illumination source was focused onto the sample with a 100x 1.4NA oil objective lens.

The 2845 cm^{-1} vibrational Raman mode corresponding to aliphatic C–H vibrations found

[2] 100 % confluence is when the cell population grows to cover the entire surface

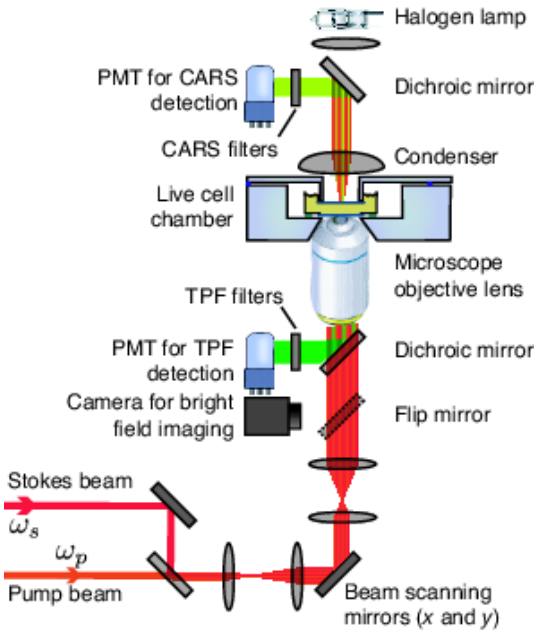

Figure 4.2: Multimodal CARS and TPF microscopy system. The Stokes laser is tuned to 896 nm and the pump to 714 nm, to target a Raman shift of 2845 cm^{-1}. The two lasers are mode-locked and the pulses are synchronized. An x–y pair of galvanometer mirrors is used to scan the combined beams across the sample. The CARS signal is detected by a photomultiplier tube (PMT) in the forward direction (F-CARS) and TPF is detected, also by a PMT, in the backward direction. The set-up can also perform bright field imaging with a halogen lamp and camera.

in lipids (102) was targeted by tuning the pump laser wavelength to 714 nm and the Stokes laser to 896 nm. This generated a CARS signal at 593 nm, which was separated from the laser beam path using a long wave-pass dichroic mirror (683dcxr, Chroma) and further filtered with a short wave-pass filter (680/SP-25, Semrock) and a narrow band-pass filter (600/14-25, Semrock). The forward CARS (F-CARS) signal was detected with a photomultiplier tube (PMT) (R3896, Hamamatsu). The Stokes beam at 896 nm falls within the excitation band of GFP, allowing simultaneous TPF imaging with CARS. Unlike CARS, TPF is emitted isotropically (103) and is most efficiently collected in the backward direction, therefore a dichroic mirror placed behind the objective lens enables the TPF signal to be reflected out of the beam path and onto an identical PMT (R3896) detector. Two filters, a short wave-pass (680/SP-25, Semrock) and a broad band-pass (510/84-25, Semrock), were used to block the pump and Stokes laser wavelengths whilst transmitting most of the GFP emission spectrum. The band-pass filter also

blocks the CARS signal at 593 nm. The picosecond pulse duration used in this set-up is ideal for CARS microscopy, but less so for TPF. Nonetheless, it is still capable of producing high-quality TPF images (104).

A custom LabVIEW program was used for Image acquisition, which controlled the beam scanning mirrors and enabled the CARS and TPF signals collected to be recorded. The laser power at the sample was adjusted with neutral density filters (not shown in the Figure). Bright field microscopy was used for all sample alignment and focusing in order to minimize the exposure of the sample to the laser beam.

4.4 Results and discussion

4.4.1 Multimodal microscopy: simultaneous CARS and TPF

The system was optimised so that simultaneous CARS and TPF images could be acquired (rather than the sequential CARS-TPF images obtained by Robinson et al. (95)). The advantage of simultaneous imaging over sequential is that the images are acquired in the same focal plane at the same moment in time. This avoids problems associated with mechanical drift of the focus or small movements of the cell between CARS and TPF images. For sequential images, TPF images are acquired using only the Stokes laser beam, however for simultaneous acquisition, both the Stokes and the pump beam are focused onto the sample. As such, it was essential to ensure that the pump beam did not result in background, additional unwanted non-linear excitations or CARS signal cross-channel leakage.

Simultaneous and sequential CARS and TPF images are shown in Figure 4.3 as A|B and A|C respectively. Bright spots were observed in the cytosol in Figure 4.3A, which were identified as the resonant CARS signal from lipid droplets (102). Sequential TPF images (Figure 4.3C) were collected by scanning the Stokes laser beam only, the wavelength of which falls within the two-photon excitation band of GFP. It is evident that the TPF images generated simultaneously with CARS (Figure 4.3B) are comparable to the images generated sequentially (Figure 4.3C), with both TPF images revealing similar features. The bright high-contrast spots

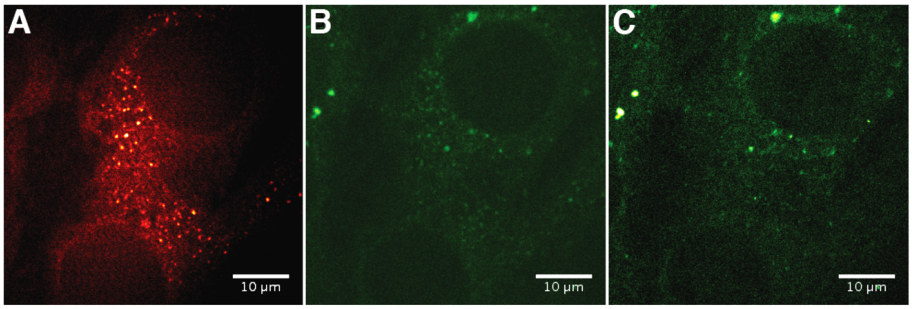

Figure 4.3: Images of fibroblast cells infected with a genetically modified mCMV which causes cellular expression of GFP. The CARS image (A) shows the distribution of cellular lipid droplets. The TPF image (B), acquired simultaneously with the CARS, shows the sites of GFP, indicating that the cell is infected. A second TPF image (C) was recorded after the CARS image (sequentially) using only the Stokes laser beam with the pump beam blocked.

in the simultaneous image (Figure 4.3B) could in principle arise from either CARS or GFP. To confirm that cross-channel CARS leakage was not significant, pairs of images were taken with the phase of the pump and Stokes beams shifted by approximately 180° using the phase-locked loop system (Synchrolock-AP, Coherent Inc.). When the beams are out of phase, pump and Stokes pulses do not arrive at the sample simultaneously, so frequency mixing cannot occur and no CARS signal is generated. This test allows discrimination of the TPF signal from the CARS and confirmed that the filters did indeed prevent cross-channel leakage. The bright spots in TPF images recorded simultaneously with CARS (Figure 4.3B) were therefore unambiguously identified as sites of GFP accumulation.

4.4.2 Cell viability

A method for assessing photodamage of cells is by observing physical changes in cell morphology, for example, rounding or rupturing of the membrane and detachment of the cell from the coverslip surface. There is a surprisingly small amount of literature regarding the assessment of photodamage in live cells due to laser exposure, beyond observing the change in cell morphology. For it to be feasible to image a single cell over the entire course of infection, the internal chemical and biological functions of the cell must not be affected by laser scanning. Yet, consideration must be given to the image quality and contrast, by which a higher laser exposure increases the image contrast, where laser exposure is defined as the product of the

laser beam (average) power, the cell area and the image acquisition time. As such, a balance must be struck between low laser exposure, to minimise cell damage, and image contrast, which is related to the laser power and image acquisition time.

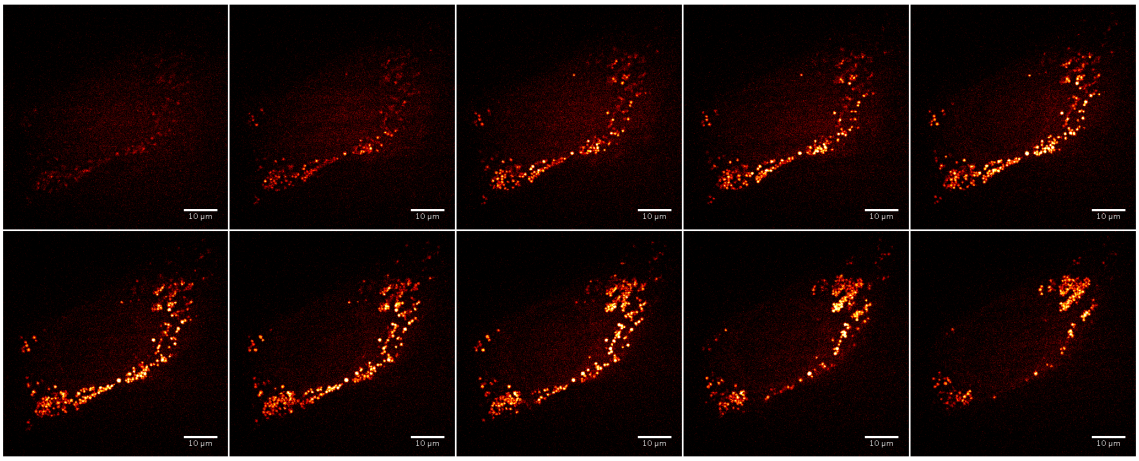

Figure 4.4: A stack of CARS images through a single cell. Slices were taken at 0.25 µm increments in the z-direction. The laser power at the sample was approximately 35 mW. The bright spots visible in the images were identified as lipid droplets.

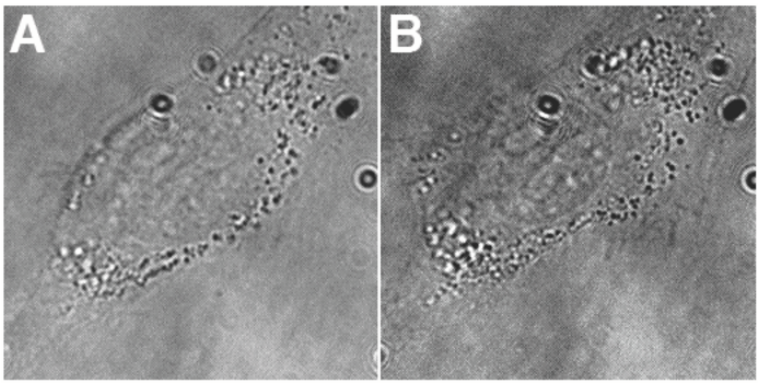

Figure 4.5: Brightfield images recorded before (A) and after (B) the acquisition of the stack shown in Figure 4.4. Visible photodamage is apparent after laser scanning.

To assess the cell viability for the purpose of determining the feasibility of studying a single cell over the course of infection, a single cell was monitored using bright field microscopy for physical effects of photodamage whilst exposed to different laser intensities and different laser scanning durations. Firstly, using a low combined average laser power of approximately 35mW at the sample, a stack of images was acquired at increments of 0.25 µm, starting

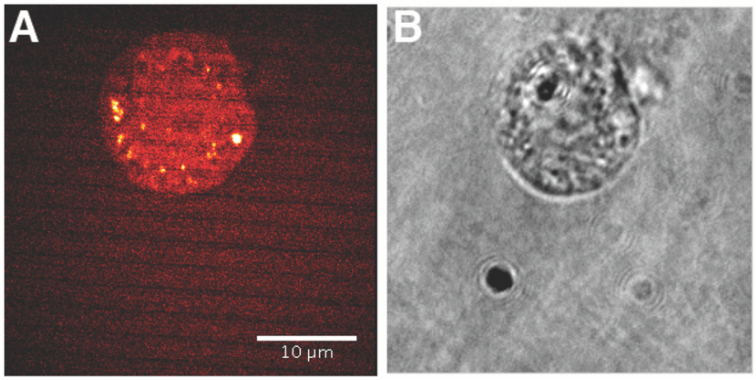

Figure 4.6: CARS (A) and brightfield (B) images of the same cell shown in Figure 4.4 and Figure 4.5 recorded 2 hours after acquisition of the stack.

from the coverslip and scanning upwards in the z-direction. Figure 4.4 shows the stack of images where the lipid droplets, depicted by the bright spots, can be clearly seen. Brightfield images were taken before (Figure 4.5A) and after (Figure 4.5B) recording the stack to identify physical signs of photodamage. The image taken after recording the stack shows a small degree of morphological change to the cellular membrane, whereby the membrane is seen to become slightly more rounded in shape. This suggests that by the time visible changes are observed, cells are already beyond their damage threshold. Images of the same cell recorded two hours later, shown in Figure 4.6, revealed that the cell had become rounded and detached from the surface of the Petri dish, which is characteristic of cell death. Nearby cells retained a normal appearance, indicating that the cell's death was due to photodamage effects from the laser scanning. It can also be seen in Figure 4.4 that during the imaging timescale, no significant physical changes due to photodamage can be observed in the CARS images of the lipid droplets.

The accumulated laser exposure experienced by a cell during stack acquisition is far greater than required for imaging a single slice. Cell viability was tested against a range of laser powers in order to determine the optimum parameters for 2D imaging. It was found that integrating over 4 image scans of 512×512 pixels provided the optimum balance between noise, image contrast and acquisition time. The minimum average laser power for these parameters was approximately 28 mW at the sample, however at this power the noise was relatively large

compared to the signal. Increasing the laser power increased the image contrast but also increased the likelihood of photodamage, therefore further cell viability tests were applied on different cells with increased laser powers to determine whether higher laser powers caused immediate damage to the cell morphology.

It was found that powers up to 120 mW could be used without causing morphological changes to the cell on the timescale of imaging. However every cell that was imaged, including the cell imaged using an average laser power of 28 mW, exhibited morphological changes to the membrane which only became apparent some time after imaging. Typically, the physical changes were only observed 30 minutes post laser scanning, therefore long time-course experiments, which involve imaging a single cell over many hours could not be carried out. Instead, it is feasible to image many cells within the live cell population over the time period of interest, which enables a large sample size for each infection time point to be acquired. This gives an overview of the state of the cell population at each time point, and allows the change in the cell population to be assessed over the time-course of infection.

4.4.3 Quantification of the stage of infection using fixed cells

In order to correlate the lipid droplet behaviour observed using CARS microscopy to the stage of infection of live cells, a method to quantify the progression of infection is required. Cells infected via synchronisation transfection method were fixed at 3 hour intervals from the start of infection. Fixed cells were ideal for the purpose of creating an infection timeline, in which the fixing of the cells at 3 hour intervals from the start of infection enabled the effects of infection to be imaged at those specific time points.

TPF images provide a picture of the distribution of cellular GFP, whilst the integrated TPF intensity across the cell gives a quantitative measure of the amount of GFP within the cell, which is an indicator of viral activity. Specifically, cellular transcription of viral mRNA causes expression of GFP, so an increase in the quantity of GFP within a cell indicates more viral activity as an increase in transcribed viral mRNA results in greater production of GFP, indicating the progression of infection. The integrated TPF signal can therefore be used

as a measure of the infection stage of the cells, which coupled with CARS images of the intracellular lipid droplets allows changes in the lipid droplets to be linked to a time point of infection. TPF is a second-order nonlinear process, so the fluorescence emission intensity is proportional to the square of the excitation intensity. There were small variations in laser power between different images, therefore the image data were divided by the square of the laser power to correct for these variations.

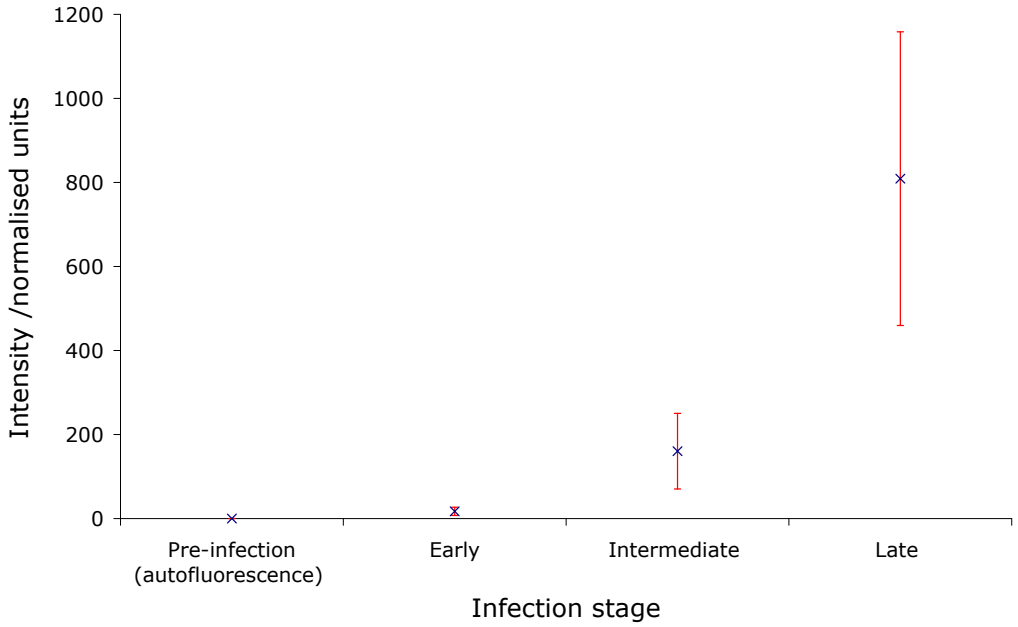

Figure 4.7: Graph showing the average intensities for a set of TPF images acquired pre-infection; and during the early, intermediate and late stages. Error bars indicate 1 standard deviation of the data sets. To account for small changes in laser power between images the two-photon intensities have been normalized by dividing by the square of the power.

It was found that the data could be grouped into three statistically distinct infection stages, based on the empirical data of the measured fluorescence intensity. The groups correspond to time points of 0–9 hpt, 9–24 hpt and > 24 hpt and determined as the early, intermediate and late stage of infection respectively, as shown in Figure 4.7. The graph shows a significant increase in fluorescence intensity as the infection progressed, whereby the average intensity increased from 17.3 to 1025.9 (normalised units) during infection and the standard deviation for each

data set confirmed that these were significantly different. TPF images of a control sample of uninfected cells (pre-infection) were also acquired, showing an average intensity of 0.09, indicating that there was no significant autofluorescence background in the uninfected cells. Consequently, the intensity of the GFP signal is a good indicator for the stage of infection.

The corresponding CARS images show the lipid droplet configurations and changes in cell morphology in the fixed cells. All cell samples in the early infection stage (0–9 hpt) displayed similar features to those exhibited by the cell shown in Figure 4.8. During this stage, CARS images showed both uniform size and spatial distributions of lipid droplets throughout the cytosol. TPF images had zero or limited contrast, indicating either no GFP, or the presence of a low concentration of GFP in the cytosol. There was no TPF signal from the nucleus, as GFP is expressed in the cytoplasm. The images also show areas of small accumulations of GFP in the cytosol, which could indicate the sites of GFP expression or suggest vesicle-mediated GFP transport.

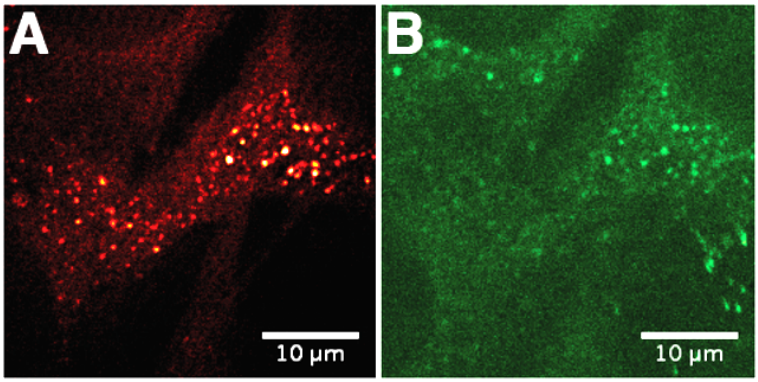

Figure 4.8: CARS (A) and TPF (B) images of cells fixed at the early stage of infection. Lipid droplets of regular size are uniformly distributed in the cytosol. The low level of fluorescence provides limited contrast in the TPF image.

CARS images of cells acquired at times between 9–24 hpt typically exhibited the features shown in Figure 4.9, where correlation of the CARS images with the TPF intensities measured confirmed that these observations of lipid droplet configurations are linked to the intermediate stage of infection. The cells in this group displayed some lipid droplet clustering, whereby non-uniform spatial distributions of lipid droplets and some relatively large lipid droplets became identifiable. In addition, a general increase in cell nucleus area was evident. This is consistent

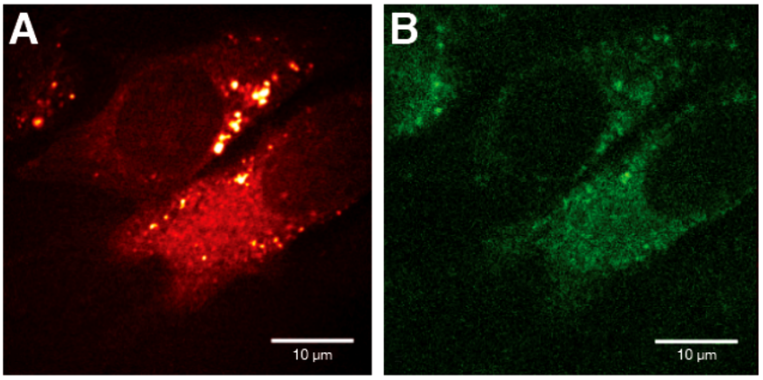

Figure 4.9: CARS (A) and TPF (B) images of cells in the intermediate stage of infection. The distribution of lipid droplets is less uniform than in the early stage (Figure 4.8) with the emergence of some clustering. The TPF image shows an increased amount of GFP expression.

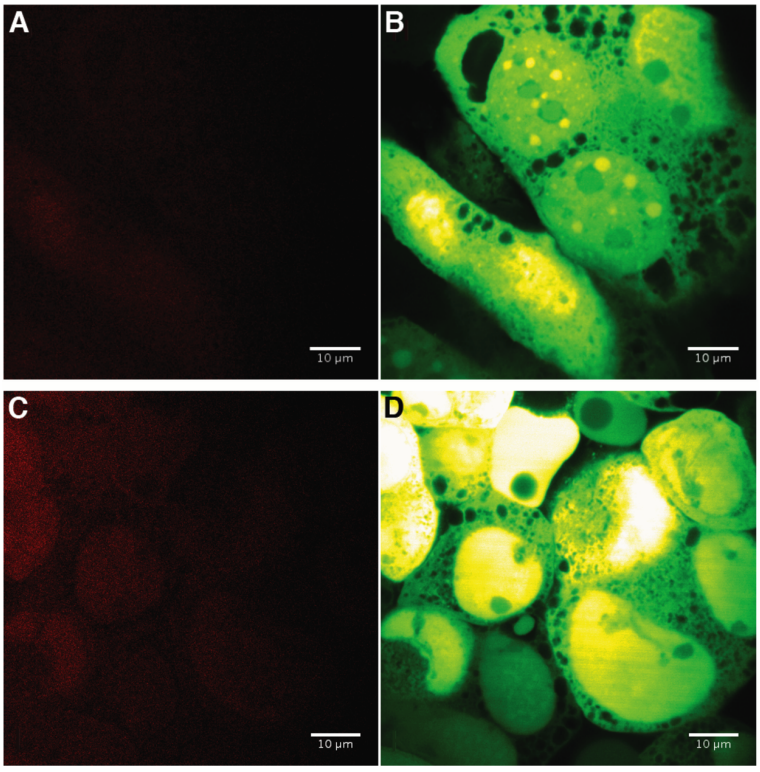

Figure 4.10: CARS (A) and TPF (B) images of a sample of cells fixed in the late infection stage. (C) and (D) are CARS and TPF images of a different area of the same sample. The very low contrast in the two CARS images (A,C) is due to the absence of lipid droplets. The TPF images (B,D) show a high level of GFP expression as well as fragmentation of cell nuclei suggesting apoptosis.

with an earlier study (95), which concluded that infected cells exhibited nuclear expansion.

Figure 4.10 shows typical CARS and TPF images of cells infected for > 24 hpt, which were designated as the late stage of infection. The contrast is very limited in the CARS images due to a dramatic reduction in the number of lipid droplets, with no lipid droplets detected in the majority of CARS images. In Figure 4.10A and C, only the non-resonant CARS signal was detected. The corresponding TPF images indicated high concentrations of GFP in both cytosol and nucleus, suggesting that GFP is imported into the cell nucleus at this late infection stage. Additionally, many images display fragmented cell nuclei, which suggests the cells are undergoing apoptosis.

4.4.4 Multimodal imaging and study of live cells during infection

The study using fixed cells enabled the infection process to be grouped into three visually distinct stages, however a persisting question is to what degree the fixing method perturbs the cell. For example, it is known that the formaldehyde fixing method causes rapid degradation of lipid droplets (105), which may affect the condition of the droplets when they are imaged. As such, the use of live cell samples is imperative for further analysis of lipid droplet characteristics during the infection process as the progression of infection in the unperturbed cells can be observed, with the additional benefits of being able to image more infection time points.

One factor regarding the live cell sample is that the cells often progressed through the infection process at different times, so within one field of view it is possible that every cell may be at a different stage of infection, which is evident in Figure 4.13B, therefore using the TPF intensities measured from the fixed cell study as a guideline, the live cells were assigned to a stage (early, intermediate or late) of infection.

CARS images of cells show a trend in the lipid droplet configurations throughout the course of infection, where common lipid droplet spatial distributions within the cytosol could be identified for each infection stage. Figure 4.11, Figure 4.12, and Figure 4.13 show typical images of cells in each group.

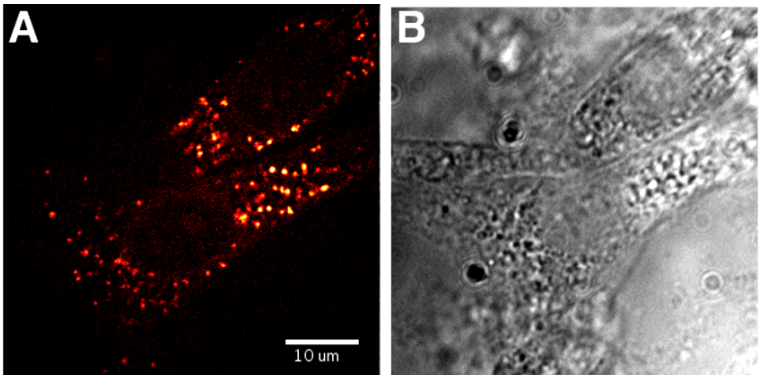

Figure 4.11: CARS (A) and bright field (B) images of a group of live cells during the early stage of infection. The CARS image shows lipid droplets of regular size uniformly distributed throughout the cytosol. The pump and Stokes laser powers at the sample were approximately 25 mW and 30 mW respectively. The bright field image is shown in this example, which depicts the cell outline because no TPF signal was detected.

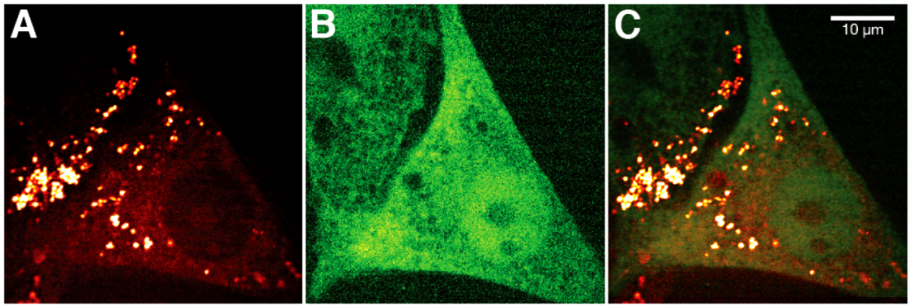

Figure 4.12: CARS (A) and TPF (B) images of two cells in the intermediate stage of infection. The images are overlaid in (C). The pump and Stokes laser powers at the sample were approximately 28 mW and 32 mW respectively. The CARS image shows a non-uniform distribution of lipid droplets within the cytosol; the lipid droplets are clustered towards the neighbouring cell. The TPF image confirms that the cells are infected, and also shows that some GFP has been imported into the nucleus.

CARS images of live cells in the early stage of infection, shown in Figure 4.11, clearly show regularly-sized lipid droplets uniformly distributed throughout the cytosol, which is consistent with the preliminary study on fixed cells (Figure 4.8). The figure shows the corresponding bright field image which shows the outline of the cell, giving an indication of the cell morphology. During this stage of infection, there was low to zero TPF signal which indicated that viral mRNA transcription had only just begun, or had not occurred yet.

CARS images of cells in the intermediate stage of infection, such as the image shown in

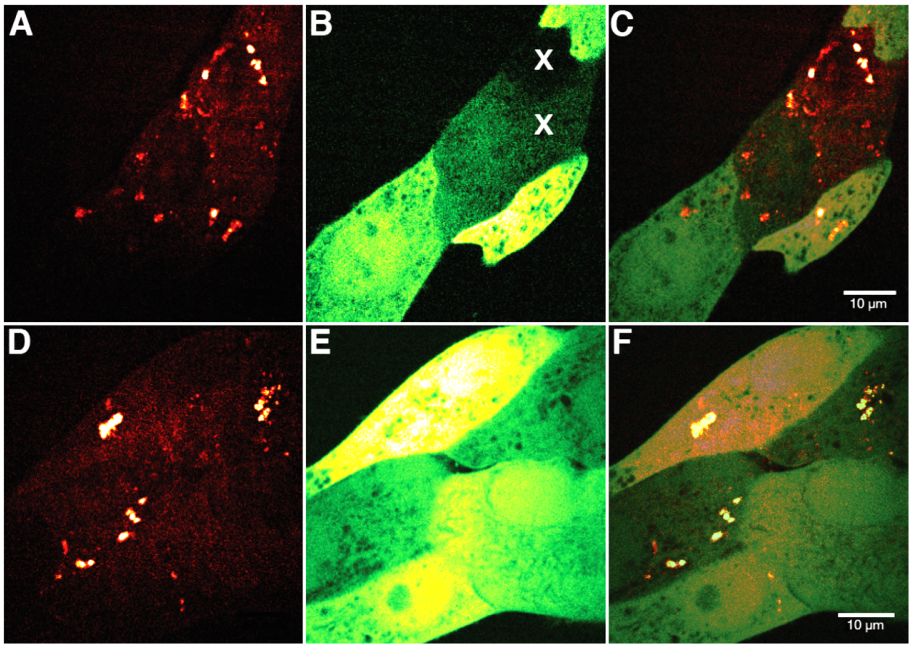

Figure 4.13: CARS (A), TPF (B) and overlaid (C) images of a group of live cells in the late infection stage. (D–F) show a different group of cells. The pump and Stokes laser power at the sample were approximately 43 mW and 47 mW respectively, which is higher than the powers used for previous infection stages due to the lower contrast in the CARS images at low laser powers. The CARS images (A,D) show a small number of lipid droplet clusters. The high intensity in the corresponding TPF images (B,E) confirm the late stage of infection. Inhomogeneous infection is evident in image (B), where most cells are in the late infection stage with the exception of the two cells marked X which are in the intermediate stage, identified using fixed cell data as a reference.

Figure 4.12 show a non-uniform spatial distribution of lipid droplets through the cytosol. In addition, some relatively large lipid droplets were seen, suggesting a clustering effect where individual droplets may be accumulating or that lipid droplets increase in size during infection. The clustering behaviour identified in the images are consistent with observations from the preliminary study (Figure 4.9).

Furthermore, some live cell images of cells in the intermediate stage of infection (including Figure 4.12) showed lipid droplet clusters positioned towards the outer membrane adjacent to neighbouring cells. This is an interesting observation as it suggests that the viral infection influences the movement of lipid droplets, directing the droplets towards neighbouring cells. In addition, it was observed that the lipid droplets in isolated cells of the same infection stage

tended to be positioned around the cell periphery (not shown). Both these observations suggest the possibility that the virus may use the lipid droplets as a means to transport the viral progeny out of the host cell and possibly into a neighbouring cell.

Live cell TPF images revealed GFP in a number of cell nuclei. To confirm that the GFP is located in the nucleus, a 3D image stack was collected and compared against a 3D image stack of a cell displaying GFP in the cytosol only. This verified the presence of GFP in the cell nucleus. This feature was not observed in fixed cell images at the same stage of infection, as GFP was only detected in the nucleus during the late stages of infection for fixed cells. These live cell images show that nuclear import of GFP occurs during the same infection stage as lipid droplet clustering. The import of GFP into the nucleus was an unexpected feature, since GFP is synthesized in the cytosol and nucleocytoplasmic transport is highly controlled (106) so that large molecules such as GFP must be actively transported into the nucleus. This suggests that the behaviour may not be a cellular function initiated by the virus but rather a side-effect of infection caused by some mechanism occurring within the cell during the infection cycle which could allow GFP to move into the nucleus. A study by Muranyi *et al.* (107) supports this observation, in which evidence is presented to show that CMV recruits cellular kinases to dissolve the nuclear lamina, allowing viral capsids to pass through the nuclear membrane. A breach in the nuclear membrane could therefore explain the presence of GFP in the nucleus.

CARS images of cells in the late stages of infection, shown in Figure 4.13, show a significant reduction in the number of lipid droplets, with the cells exhibiting a high intensity in TPF images tending not to show lipid droplets in the CARS image. The lipid droplets that were imaged were typically larger in droplet size than the droplets observed in the early stage of infection. The average laser power used to acquire these images was greater than the powers used for the initial and intermediate stages of infection because the CARS images tended to exhibit poor image contrast at low laser powers.

One of the main observations was a decrease in the number of lipid droplets as infection progressed. This decrease could either be the result of lipid droplet depletion or lipid droplet clustering, whereby clustered droplets appear as a single, large particle rather than being

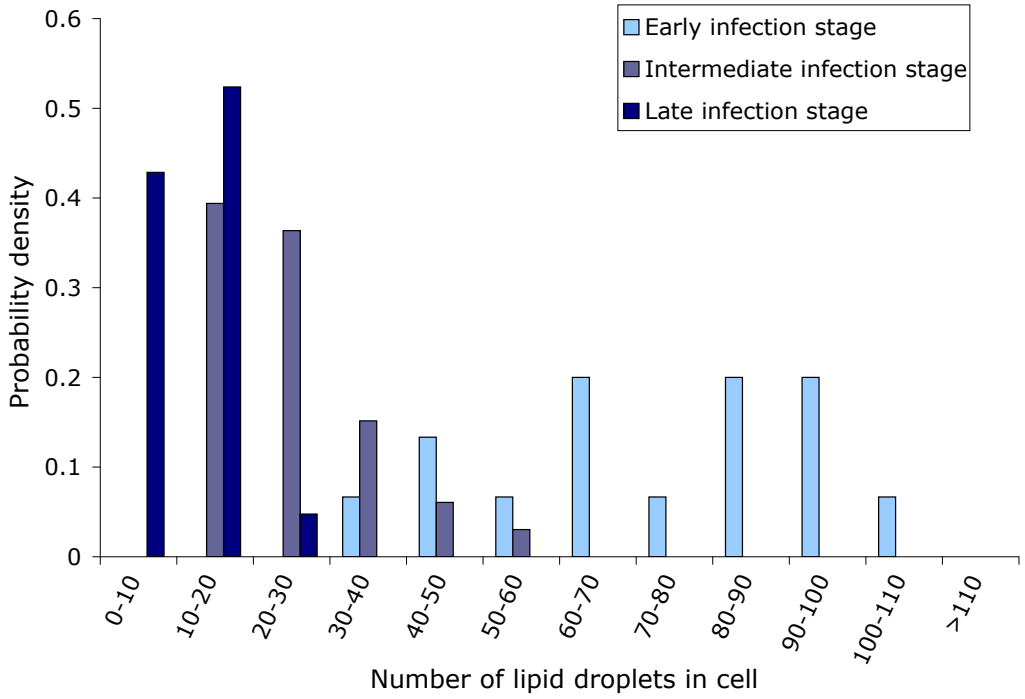

Figure 4.14: Histogram showing the probability distribution of the number of lipid droplets in a cell for the early, intermediate and late infection stages. The separate counts for each infection stage group were binned and are plotted in the histogram. An empty bin for a particular infection stage indicates that there were no cells whose lipid droplet count was within the bin range.

resolved as separate droplets. To quantify whether the observed reduction in lipid droplet number is linked to the infection process, a sample of 69 cells was examined in more detail. For each infection stage, the number of lipid droplets in each cell was counted. The histogram in Figure 4.14 shows the probability that a cell has a given number of lipid droplets during the early, intermediate and late stages of infection. A clear decrease in lipid droplet number throughout the infection process is apparent, with mean numbers of lipid droplets of 73(21), 25(10) and 11(5), in the early, intermediate and late stages of infection respectively.

Another observation was that the lipid droplets appeared to increase in size as the infection progressed. In order to quantify this, the cross-sectional area of the lipid droplets in a large sample of cells was measured for each stage of infection using ImageJ (108). 545, 897 and 295 lipid droplet areas were measured for the early, intermediate and late infection stages

respectively. A histogram showing the probability of measuring lipid droplets with a certain size during each infection stage is shown in Figure 4.15. In the early infection stage, 86 % of the cells' lipid droplets were less than 1 μm^2 in size. This confirms the observation from CARS images that all lipid droplets were broadly similar in size during this infection stage. The graph shows that the probability of measuring lipid droplets with sizes less than 1 μm^2 was 77 % for both the intermediate and late infection stages, showing that the majority of lipid droplets were similar in size to the droplets in the early stages of infection. The difference in lipid droplet sizes is most apparent for lipid droplets with cross-sectional areas greater than 6 μm^2, where the probability of finding lipid droplets larger than 6 μm^2 is greater in the intermediate stage of infection, with the probability further increasing in the late infection stage. In addition, no lipid droplets larger than 5.8 μm^2 were measured in cells in the early infection stage, showing that the large lipid droplets are only found once infection has progressed. This behaviour is highlighted by the inset in Figure 4.15, where the histogram shows the probability distribution in more detail for the lipid droplets larger than 2 μm^2.

The increase in lipid droplet size could either be due to droplet clustering, or that a side effect of infection causes the size of the droplets to increase. It is also evident that the number of lipid droplets in the late stage of infection decreases rapidly which suggests that the lipid droplets are either depleted, aggregated into larger particles, or have formed unresolved lipid droplet clusters. The number of lipid droplets in each cell within each stage of infection varies, therefore the total cross-sectional area can not be used to compare between different infection stages, which would have given an indication as to whether the droplets cluster/aggregate, or whether they are depleted. Additionally, by referring to Figure 4.12 it is evident that the individual droplets are not well resolved within the clusters, therefore it is unclear from the CARS images whether the lipid droplets form aggregations or clusters of distinct droplets. As such, further investigation is required to determine the behaviour of lipid droplets during infection. An ideal study to complement the results and observations found using CARS/TPF microscopy would be to track the lipid droplets in real time to directly assess the lipid droplet dynamics during infection. The next chapter will present a study using differential interference

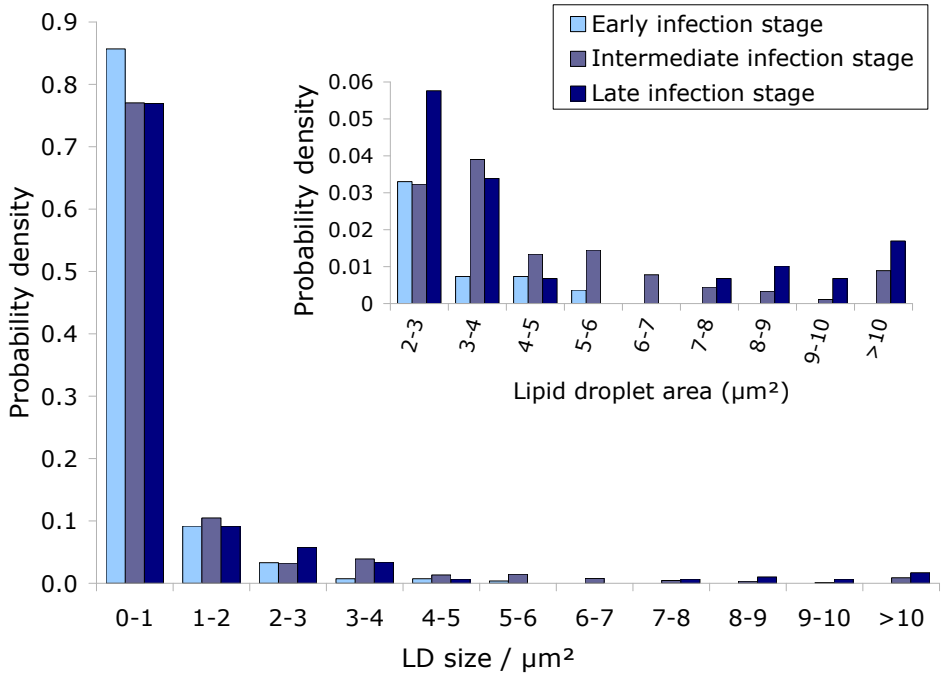

Figure 4.15: Histogram showing the probability distribution of lipid droplet area for the early, intermediate and late infection stages. Inset: histogram (of the same data) showing the probability distribution of the lipid droplets with area greater than 2 μm^2.

contrast (DIC) microscopy, whereby the usage of DIC microscopy allows the live cells to be imaged over longer timescales in order to acquire image sequences suitable for particle tracking analysis.

4.5 Conclusion

The aim of this study was to investigate the influence of cytomegaloviral infection on host cell lipid droplets. By adapting the multimodal CARS and TPF microscope system to accommodate live cell imaging, it was found that the cells were able to survive for 2 to 3 days on the microscope stage, which enabled the fibroblast cells to be successfully observed over the entire course of mCMV infection. As a result, changes in the lipid droplet configurations were correlated to specific stages of infection (early, intermediate and late), based on the TPF intensities detected. The focus was to assess the physical changes of lipid droplets

during infection. It was found that the number of cellular lipid droplets observed via CARS microscopy significantly decreased from the early stage of infection through to the late stage of infection. It was also evident that the cross-sectional areas also increased as infection progressed. Additionally, it was found that lipid droplets with cross-sectional areas greater than 8 μm^2 were only detected in the intermediate and late stages of infection. This indicates that the change in the lipid droplet size, and decrease in the number of droplets detected could be an effect of the viral infection, where the lipid droplets are either being depleted, or are forming lipid clusters. Interestingly, the CARS images also showed that the lipid droplets tended to exhibit clustering during the intermediate stage of infection however it is unclear from the images whether the clusters are an aggregation of droplets or a cluster of individual droplets. Additionally, it was observed that during the intermediate stage of infection, lipid droplets tended to accumulate towards the cell periphery, favouring the cell boundaries adjacent to neighbouring cells. This indicates that the lipid droplet movements are influenced by the viral infection, and could possibly suggest that the virus uses lipid droplets as a method of transporting viral progeny out of the host cell, however further work is required to investigate this speculation. The following chapter will continue with a study to assess and analyse the effects of mCMV infection on lipid droplet dynamics, using differential interference contrast (DIC) microscopy to image the live cells so that the lipid droplet movements can be tracked in real time and analysed.

5

Lipid droplet dynamics: Using DIC imaging

5.1 Introduction

The study detailed in chapter 4 presented results which indicate a tendency for lipid droplets in fibroblast cells infected with murine cytomegalovirus (mCMV) to exhibit a higher degree of clustering than in healthy cells. This suggests the possibility that lipid droplet positioning within the cell is affected by the viral infection, either directly or as a by-product. The change in lipid droplet arrangement may also imply that droplet dynamics and movements are influenced by the viral infection. This chapter will present a study on lipid droplet dynamics, where the aim was to analyse and quantify lipid droplet movement and arrangement within healthy and infected cells. The focus of the analysis was to determine whether a significant difference in lipid droplet motion and arrangement due to the interaction of cytomegalovirus could be identified.

5.2 Background

Differential interference contrast microscopy (DIC) was used to image and identify lipid droplets in live fibroblast cells. Image contrast in the DIC images is produced by differences in the gradients in optical path length of the incident light as it passes through the specimen

comprising components with different refractive indices. This phase shift of light is detected as a difference in amplitude, creating pseudo 3-dimensional images with heights and depths dependent on the refractive index and optical thickness of the specimen. This makes the technique ideal for imaging cellular lipid droplets because lipid droplets have a much higher refractive index than other organelles in the cell (109).

DIC microscopy was selected over phase contrast microscopy for the following reasons. Optical sectioning is far superior in DIC microscopy, whereby a thin focal plane can be clearly imaged (110), enabling lipid droplets to be easily identified within the cell. On the other hand, in phase contrast microscopy, an annular ring positioned in the back focal plan restricts the objective aperture and results in specimens above and below the focal plane to also be imaged. The annular ring also introduces diffraction halos, so that phase contrast images tend to be overwhelmed by cellular features and diffraction halos, making it difficult to precisely determine the location of the lipid droplets.

Another benefit of using DIC imaging is the relatively low stress exerted on the cells, especially when compared to laser scanning techniques. Therefore, cells can be continuously imaged over a longer time frame, without inducing effects of photo damage. This enables a single, live cell to be imaged over many hours and also for continuous video capture to be employed. In addition, the image acquisition time for DIC images is significantly less than for CARS and TPF images, which allowed image sequences of the the lipid droplet movements to be captured, and so the lipid droplet positions could be tracked, enabling the movement and dynamics, as well as the clustering behaviour of the droplets to be analysed.

5.3 Method

5.3.1 Imaging system and sample preparation

For the study of healthy fibroblast cells, cultures were grown using the same method as described in chapter 4, where NIH/3T3 fibroblast cells with a passage number in the range 11–20 were cultured in Dulbecco's modified Eagle's medium (DMEM), with L-

glutamine (200 mol/m^3), penicillin/streptomycin (10 000 units/ml) and 10 % calf serum. Standard growth conditions of 37 °C and a 5 % CO_2 environment were maintained during an incubation period of 12 hours. The cells were harvested when 70-80% confluent and seeded onto glass-bottom Petri dishes (P35Gcol-1.0-14-C, MatTec) ready for imaging. The infected samples were prepared by Mathieu Blanc, from the Division of Pathway Medicine, University of Edinburgh. Infection with mCMV wildtype mutant C3X was carried out at a multiplicity of infection (MOI) of 1, with the growth media containing 3 % calf serum.

To prepare for imaging, the cells were seeded onto a glass-bottom Petri dish and sealed within a 5 % CO_2 environment in the live cell chamber detailed in Chapter 4. The sample was kept in an ice container prior to imaging. As soon as the sample was placed onto the microscope stage, the cell chamber was heated and maintained at 37 °C, at which point infection would begin and this is therefore denoted as the starting time of infection. A commercial inverted Nikon microscope, set up for DIC imaging was used to image the fibroblast cells. Illumination was provided by a tungsten bulb, and a 1.4NA 100x oil objective lens was used to image the sample.

DIC image sequences were acquired at 10 frames per second, with each video lasting between 40 seconds and 2 minutes. For both healthy and infected cells, many image sequences of a large number of cells in the sample were recorded to capture the lipid droplet motion for the cell population. In addition, a selection of infected cells were followed throughout the course of infection to produce an infection timecourse study.

5.3.2 Particle identification and tracking

One of the particle tracking algorithms used for this study required the images to be thresholded and converted to a binary format. Fluorescence images are ideal for this since bright fluorescent particles against a dark background can be identified with ease. On the other hand, DIC images tend to be difficult to threshold uniformly as a number of lipid droplets tend to be removed during thresholding. As such, a combination of particle identification methods must be used to accurately identify and track lipid droplets in DIC images.

Two ImageJ plugins, Mtrack2 and Spottracker, were used side by side to ensure successful tracking of lipid droplets. Mtrack2 is a multi-particle tracking plugin, and requires the image stack to be thresholded. To optimise the number of lipid droplets thresholded, a size filter was applied since it was shown in Chapter 4 that the size of lipid droplets in fibroblast cells tend to range between 0.35 μm and 0.7 μm in diameter. Image artefacts which persistently feature in the images tend to be larger, and along with other cellular features tend to have lower contrast than lipid droplets. The Spottracker plugin is designed specifically to utilise the high contrast of DIC images, and is ideal for tracking individual particles missed by thresholding. The centre of lipid droplets have the highest intensity, therefore they are identified and tracked based on intensity changes across the image stack. Unfortunately, Spottracker is highly time consuming as it can only track one particle at a time where the typical time taken to process a trajectory ranged from 40 seconds to 2 minutes.

5.4 Results and Analysis

DIC images of healthy NIH/3T3 fibroblast cells and cells infected with mCMV were recorded at ten frames per second. The lipid droplets are easily distinguished in the cell, as shown in Figure 5.1 where the droplets appear as light grey/white, circular particles. Comparisons with previous studies provide confidence in identifying lipid droplets in these images, where studies presenting both DIC and fluorescence microscopy of fluorescent labelled lipid droplets (111) (109), and the CARS images presented in Chapter 4 confirmed similarities in shape, size and contrast of the imaged droplets.

The movement of lipid droplets in live cells could be observed in real-time, where the droplets were seen to alternate between diffusive and directed modes of motion. Differences in lipid droplet dynamics between healthy and infected cells were evident. The motion of lipid droplets in the diffusive regime appeared to be more constrained within healthy cells, whereas diffusive droplets in the infected samples appeared to be more dynamic with large clusters of individual lipid droplets seeming to move together, and slide past other droplet clusters in an almost fluid-like manner. In addition, the number of lipid droplets moving in a specific

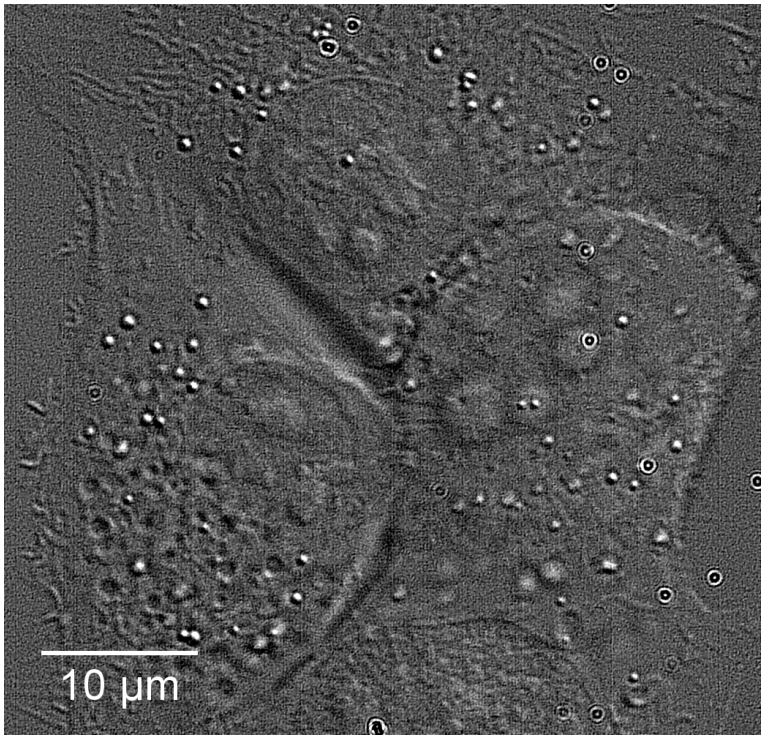

Figure 5.1: DIC image of three 3T3 fibroblast cells (healthy). Lipid droplets can be clearly identified as light grey/white particles with diameters between 0.3 µm and 0.7 µm. The cellular membrane and nuclear membrane can also be identified.

direction, identified as directed motion, was seen to be greater in infected samples.

A greater degree of lipid droplet clustering in infected cells was also observed. Groups of closely packed lipid droplets were more frequently seen in infected cells, with the clusters comprising a number of individual lipid droplets. This mirrors the observations made from CARS images of infected fibroblast cells, shown in chapter 4, where lipid droplets were seen to cluster during the intermediate stage of infection and confirms that the clusters are composed of individual droplets rather than an aggregation.

Various analysis methods were used to analyse and quantify the observations detailed above. Lipid droplet dynamics was studied by analysing the trajectories obtained through particle tracking of single lipid droplets, and lipid droplet clustering was analysed by calculating the radial distribution function to determine particle densities across the cell.

5.4.1 Trajectory analysis

Lipid droplet trajectories were acquired using the particle tracking methods described earlier, where the droplet positions were tracked across an image sequence. Each trajectory may comprise segments of both diffusive and directed motion since lipid droplets frequently switch between the two modes. As a result, the modes must be distinguished and treated separately because directed travel occurs via a different mechanism to diffusion. Studies have shown that directed motion of lipid droplets occur along microtubules and is facilitated by the pulling of molecular motors (73). The study presented by Lyn et al. (109) found that movement of lipid droplets in (normal) Huh7.5 cells were restricted when treated with nocodazole, which acts to disrupt the microtubule network. This suggests that the directed motion trajectories are dependent on the microtubule network and molecular motor activity, and therefore can be described in terms of movement speed and distance travelled. On the other hand, diffusive motion is dependent on the temperature and viscosity of the medium, and is described in terms of diffusion coefficient.

5.4.1.1 Mean squared displacement

The mean squared displacement (MSD) can be used to characterise the lipid droplet trajectories (112). To calculate the MSD, the trajectory is analysed in terms of its step-wise displacements, where the MSD is calculated for each displacement and averaged over the time-step, Δt. The displacements for different time-step magnitudes, $n\Delta t$, which is also referred to as timelag, τ, are determined, and using equation 5.1 (113), the MSD is calculated,

$$\begin{aligned} &\text{For} \quad \tau = n\Delta t \\ &\qquad < r_\tau^2 > = \frac{1}{N-n} \sum_{i=1}^{N-n} (\vec{r}_{i+n} - \vec{r}_i)^2, \qquad n = 1, ..., N-1 \end{aligned} \tag{5.1}$$

where N is the total number of frames and $\vec{r}$ is the location of the lipid droplet. The MSD shows how the amplitude of the lipid droplet motion fluctuates from the average displacement as a function of timelag, therefore the value is affected by the size of τ. Consequently, it is

important to optimise the number of τ used to produce the MSD curve, with the number of data points within each timelag. It can be seen that when τ is large, the number of displacement data points is less than when τ is small, where at large τ, each displacement averages over a longer segment of the trajectory. As a result, the MSD calculated for large τ is less representative of the actual trajectory and much of the literature suggest that only the initial portion of the MSD curves are valid for analysis (114). The valid proportion of the curve is dependent on the ratio between the number of data points for each timelag, n, and the number of frames that make up the length of the trajectory, N. The initial portion of the trajectory, $\frac{n}{N}$, should be small, and in this study, the ratio $\frac{n}{N}$ was chosen to be $\frac{1}{4}$ (112), which is consistent with other MSD scripts, such as the IDL script, msd.pro (115). The minimum length of the trajectories analysed was restricted to 16 frames to ensure at least 4 data points in the MSD curve. A script written for the analysis software IGOR Pro by Nicholas Barnes (116) was used to calculate the MSD and to determine the diffusion coefficient and the exponent, α, for the trajectories.

The type of motion exhibited by the lipid droplets is characterised by a power law for the MSD (112),

$$< \Delta r^2 >= A \times \left(\frac{\tau}{\Delta t}\right)^{\alpha} \tag{5.2}$$

where A has the dimensions of length square, and is a prefactor that contains the effective diffusion coefficient, D, for diffusive motion, or velocity for directed, ballistic motions (112). The exponent, α, denotes the mode of motion, such that when $\alpha = 1$, the mode of motion is Brownian, and when $\alpha = 2$, the mode of motion is ballistic, which is also often described as directed motion (114). Additionally, there are two further diffusive regimes, in which $\alpha < 1$ and $1 < \alpha < 2$ denotes subdiffusive (constrained Brownian motion) and superdiffusive modes respectively (113).

For Brownian diffusion, MSD scales linearly with time therefore

$$< \Delta r^2 >= A \times \frac{\tau}{\Delta t} \tag{5.3}$$

where the prefactor A determines the diffusion coefficient

$$A = 2dD\Delta t \tag{5.4}$$

d is the dimension of the system, D is the diffusion coefficient, Δt is the time-step and corresponds to

$$D = \frac{<\Delta r^2>}{2d\tau} \tag{5.5}$$

Since the prefactor A is directly proportional to D, an effective diffusion coefficient is calculated for exponent $\alpha \neq 1$ by choosing $\tau = \Delta t$ (112), therefore,

$$D = \frac{A}{2d\Delta t} \tag{5.6}$$

In this way D is not explicitly dependent on exponent, α (112), and retains the dimensions of length squared per time ($\mu m\, s^{-1}$), so by using equation 5.2 with equation 5.6, a diffusion coefficient, D, was extracted from the diffusive lipid droplet trajectories independent of the type of diffusion.

The diffusion coefficient and exponent is determined by linearising equation 5.2, with $A = 2dD\Delta t$. By plotting $ln(MSD)$ against $ln(\tau)$, the gradient of the line gives the exponent α and the y-intercept enables D to be calculated. The linearised equation for MSD is shown in equation 5.7.

$$ln(MSD) = ln(4D) + \alpha ln(\tau) \tag{5.7}$$

5.4.1.2 Separating diffusive and directed trajectories

Before calculating the MSD of the trajectories, the diffusive and directed modes of motion need to be distinguished and separated. By plotting the $x-$ and $y-$ coordinates of the lipid droplet position in each frame of the image sequence, the lipid droplet trajectory can be visualised. Figure 5.2(a) and (b) show the trajectories exhibited by two lipid droplets in a fibroblast cell.

The plots show the lipid droplet trajectories switching between diffusive and directed motions, where directed motion can be identified by the directional segments, and diffusive motion by the clustered segments.

Figure 5.2(c) and (d) shows the displacement of the lipid droplets between each frame, where the trajectory is comprised of distinct short and long displacements. The displacement of the trajectories can be related to whether the mode of motion is diffusive or directed, and referring to equation 5.2, it is evident that the magnitude of δr for diffusive motion increases linearly with t. This indicates that when t is relatively large, the diffusive displacements are small and are therefore smaller than the typical displacements exhibited by directed motion. This also confirms that the chosen frame rate of 10 fps is ideal for the study. As a result, the two modes of motion can be separated by applying a threshold to distinguish between the short and long displacements per frame.

To determine the threshold, a theoretical value for the maximum distance travelled between two frames by a lipid droplet undergoing Brownian motion was calculated. Firstly a theoretical diffusion coefficient, D, was estimated using the Stokes-Einstein relation,

$$D = \frac{k_B T}{6\pi\eta r} \tag{5.8}$$

where k_B is the Boltzmann constant, T is the temperature, η is the viscosity in the cell and r is the radius of the lipid droplet. A radius of 0.25 μm was selected as the approximate size of an average lipid droplet, based on the study in Chapter 4 where the radius was found to range from 0.15 μm to 0.35 μm. The viscosity of the cytoplasm was taken to be 0.14 Pas, which was the average viscosity measured *in vivo* by Kuimova et al. (117). Typical literature values state that the cytoplasm viscosity is $3.2 \times$ that of water, which at room temperature would be 0.32×10^{-3} Pas (118). However, these measurements were taken with the cytoplasm removed from the cell, which consequently does not give a true representation of the actual viscosities inside the cell, since within the cell, neighbouring macromolecules contribute to the viscosity by hindering diffusion of molecules. It is also known that the local, microviscosities within a cell is complex and non uniform, therefore many studies have looked to measure the

viscosities *in vivo* (117) (119). This is important because the intracellular viscosity affects the transport and interaction of biomolecules and chemical signals in live cells. The study by Liu et al. measured the microviscosities *in vivo* to be between $0.1 - 0.5$ Pas, with small intracellular regions recording viscosities greater than 0.9 Pas (119). This is in agreement with the measurements made by Kuimova et al. therefore using 0.14 Pas to estimate a theoretical diffusion coefficient seemed sensible.

For this viscosity, the diffusion coefficient for a lipid droplet with radius, $r = 0.25$ μm, is 6.5×10^{-15} m^2s^{-1}, and using equation 5.5, with $\tau = 0.1$ seconds, gives the MSD as 2.6×10^{-15} m^2, corresponding to a root mean squared (rms) distance of 0.051 μm, suggesting that a lipid droplet with a radius of 0.25 μm undergoing Brownian motion would be displaced by 0.051 μm in 0.1 seconds.

Figure 5.2(c) and (d) shows this rms value as a red line across the plot of displacement per frame, where it is evident that the short displacements lie below this threshold. To confirm that the diffusive and directed modes of motions are successfully separated, only the displacements that lie beneath the threshold were plotted, which is shown in Figure 5.2(e) and (f). It is clear that these remaining trajectory segments belong to the diffusive regime, confirming that the diffusive trajectories can be isolated using a threshold value of 0.051 μm. This was consistent for the entire data set.

The MSD analysis is applied to the thresholded trajectories consisting of 16 or more consecutive frames. This not only ensures that there are enough data points to determine the MSD of the trajectory, but also that the analysis is independent of variations in the chosen threshold value, unless the threshold is changed so much that the directed motion displacements are included or too many trajectory segments are discarded. Each diffusive segment is analysed individually, and a diffusion coefficient and exponent value is determined for each diffusive segment of the trajectory.

Figure 5.3(a) and (b) shows plots of MSD against τ for a diffusive segment and a directed segment of a trajectory respectively, where it is evident that the plot is linear for the diffusive mode and quadratic for the directed mode. The directed mode trajectories tend to be relatively

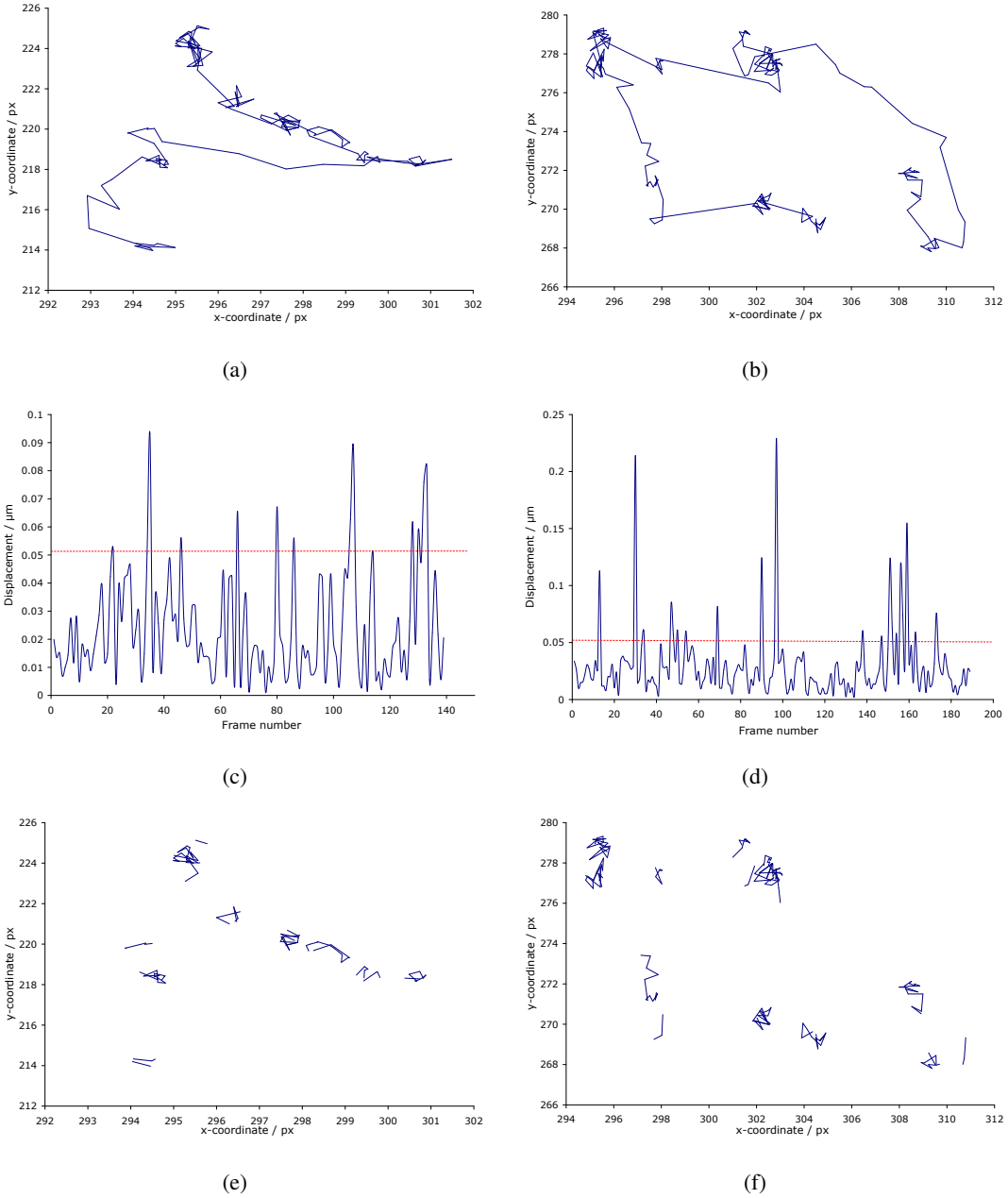

Figure 5.2: The trajectories of two different lipid droplets are shown in (a) and (b), where the clustered trajectories show diffusive motion and the linear trajectories show directed motion. Lipid droplet displacement per frame was plotted for the corresponding droplets (c) and (d). By only plotting the x and y coordinates of displacements that lie underneath the threshold, 0.051 µm the diffusive trajectory segments were visualised (e) and (f).

short, with n being between 2 and 5, as a result of using a time frame of 0.1 seconds per frame.

However, as discussed earlier, using this time-frame was deemed ideal as it allowed both the

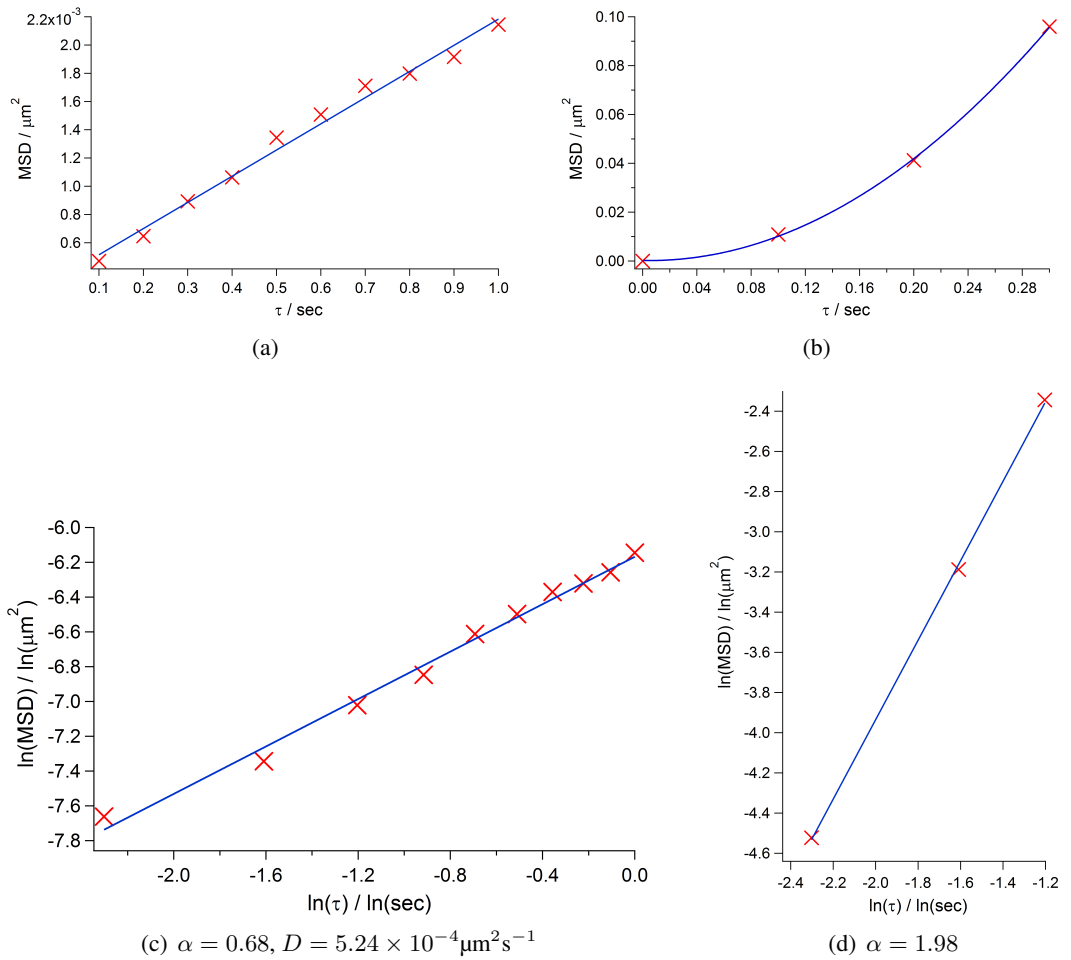

Figure 5.3: Graphs showing MSD against τ for diffusive motion (a) and directed motion (b). Diffusive and directed motion MSD plots are linear and quadratic respectively, however the directed motion trajectories tend to have a low number of data points. Plotting ln(MSD) against ln(τ) gives a linearised plot for diffusive (c) and directed (d) motion, where the gradient gives the exponent value, α. For the diffusive regime, the intercept gives the effective diffusion coefficient, D. The exponent, α describes the mode of motion. For directed motion, $\alpha \approx 2$, whereas $\alpha < 1$ is constrained diffusion, $\alpha = 1$ is Brownian diffusion and $1 < \alpha < 2$ is superdiffusion.

diffusive and directed modes of motion to be analysed.

Figure 5.3 (c) and (d) shows the corresponding linearised plots for the diffusive and directed trajectory segments, where $\alpha = 0.68$ and 1.98 respectively. As discussed earlier, $\alpha \approx 2$ denotes directed (ballistic) motion, whereas $\alpha < 1$ describes constrained diffusion, which confirms that the MSD analysis can distinguish the two modes of motion. The corresponding diffusion coefficient for the diffusive regime was determined to be 5.24×10^{-4} µm^{2}s^{-1}. The diffusion

coefficient is only meaningful when used to describe diffusive motion, therefore MSD analysis was used to analyse the diffusive trajectories only, and the velocity of the trajectory was used to analyse directed motion.

5.4.2 Timecourse study of infected cells

One benefit of DIC imaging is the capability to undertake timecourse analysis, since the technique exerts a low stress on live cell samples, allowing the same cell to be imaged over the course of infection without inducing photodamage effects. Figure 5.4 shows two cells which were imaged over 20 hours, where the top cell was denoted as cell 1 and the bottom cell was denoted as cell 2. Image sequences lasting between 40 seconds and 2 minutes of the two cells were taken every 2-3 hours for 12 hours, and again at 20 hours post infection. The lipid droplet trajectories were measured from the image sequences, with the aim to determine whether any changes in lipid droplet dynamics could be identified as the infection progressed. The number of lipid droplets in each set of images ranged from 56 to 72 droplets.

Using the analysis method detailed earlier, the lipid droplet trajectories were thresholded to separate the diffusive and directed modes of motion and the diffusive trajectories were analysed using the MSD analysis. The diffusion coefficient and exponent values were determined for each diffusive trajectory segment and averaged for each time point of infection. Figure 5.5 shows the average exponent value for each time point post infection, where it is evident that the average values are similar throughout the course of infection, with $\alpha \approx 1$. The standard deviation of the data is large and shows that the lipid droplets exhibit a range of diffusive modes of motion, however the average exponent values indicates that the typical mode of motion is Brownian diffusion.

Figure 5.6(a) and (b) shows the average diffusion coefficient at each time point in cell 1 and 2 respectively. The diffusion coefficient increases during the first 12 hours after infection from 1.3×10^{-3} $\mu m^2 s^{-1}$, to 3.5×10^{-3} $\mu m^2 s^{-1}$ before dropping down to 7.5×10^{-4} $\mu m^2 s^{-1}$ after 20 hours for cell 1 and from 8.7×10^{-4} $\mu m^2 s^{-1}$ to 3.7×10^{-3} $\mu m^2 s^{-1}$ before dropping down to 5.9×10^{-4} $\mu m^2 s^{-1}$ for cell 2. The error bars indicate one standard deviation and indicate

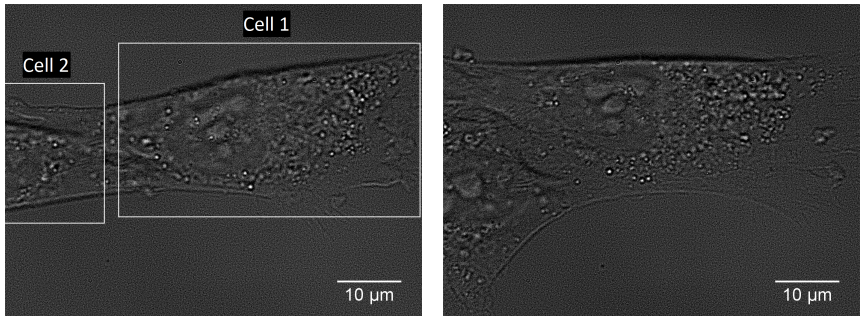

(a) 1hr (b) 4hrs

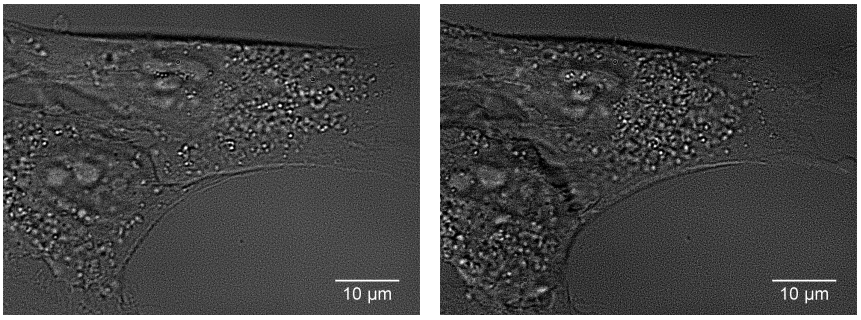

(c) 6hrs (d) 8hrs

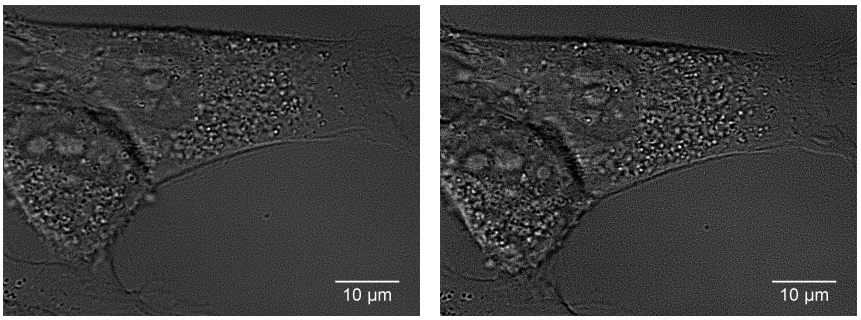

(e) 10hrs (f) 12hrs

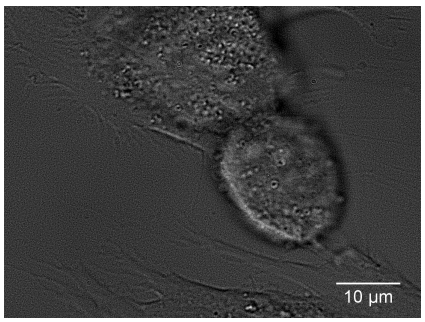

(g) 20hrs

Figure 5.4: DIC images of two cells, analysed over the course of infection. The top cell in the images were denoted as cell 1 and the bottom cell denoted as cell 2.

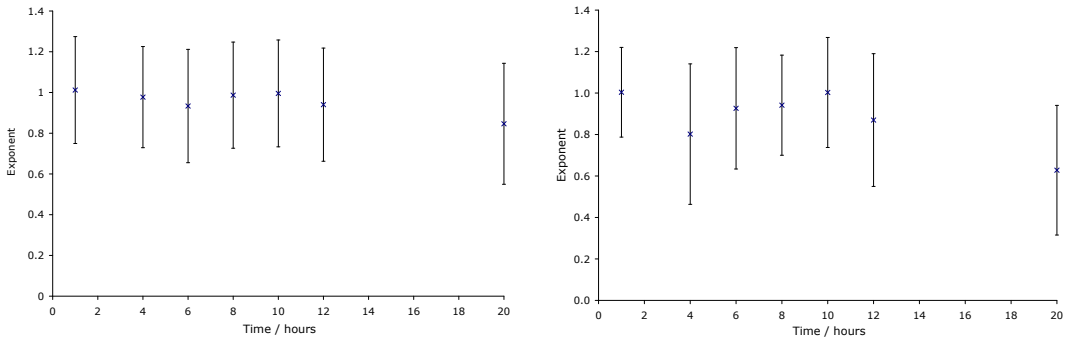

(a) Cell 1: Exponent

(b) Cell 2: Exponent

Figure 5.5: Graphs showing the average exponent value over the course of infection for cell 1 (a) and cell 2 (b). Error bars indicate 1 standard deviation.

the wide distribution in diffusion coefficients. It is evident that the increase in the average values are significant as the diffusion coefficient more than doubles over the first 10 hours post infection.

The increase in diffusion coefficient could be associated with a decrease in the size of the lipid droplets and/or by a decrease in the effective viscosity experienced by each droplet. Figure 5.6(c) and (d) shows no significant changes in the average radius of the lipid droplets, which may imply that the effective viscosity experienced by each droplet must have decreased to account for the increase in the diffusion coefficient. However, the dimensions of the lipid droplets measured falls within the resolution limit of the system, which means that if the lipid droplets are smaller, they can not be measured accurately. As such, accurate determination of lipid droplet size is not possible with this set up, therefore only the lipid droplets that are larger than the resolution limit can be assessed, and so only an estimation of the change in the effective viscosity can be applied by assessing the large lipid droplets.

Using equation 5.8 and the measured radius of each lipid droplet, the effective viscosity η was calculated. Figure 5.6(e) and (f) shows this viscosity for cell 1 and cell 2 respectively. The error bars show that there is a wide distribution in the effective viscosities, which is not unexpected as it is known that the intracellular microviscosities are non uniform (119). The effective viscosities dipped from 0.838 Pas and 1.40 Pas for cell 1 and cell 2 respectively at 1 hpi, to 0.415 Pas and 0.515 Pas for cell 1 and cell 2 respectively at 8 hpi. This indicates

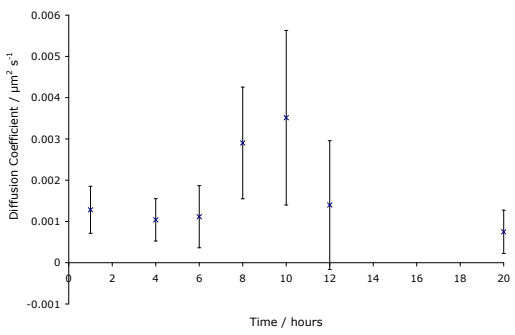

(a) Cell 1: Diffusion coefficient

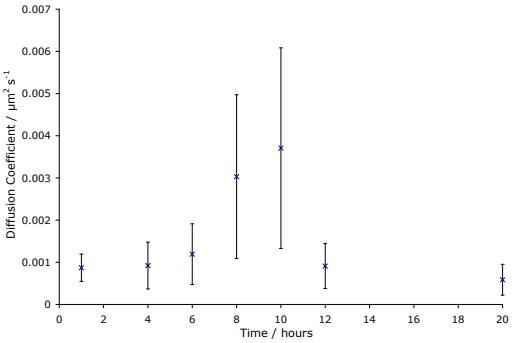

(b) Cell 2: Diffusion coefficient

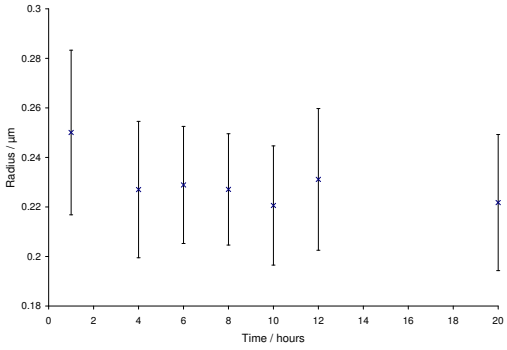

(c) Cell 1: Lipid droplet size

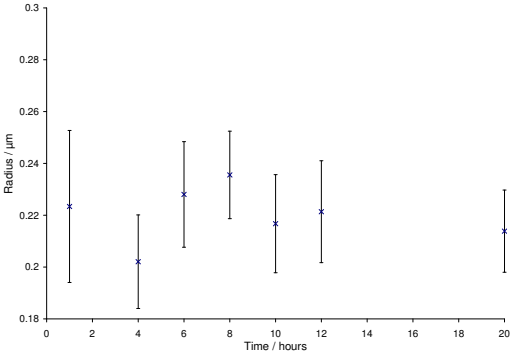

(d) Cell 2: Lipid droplet size

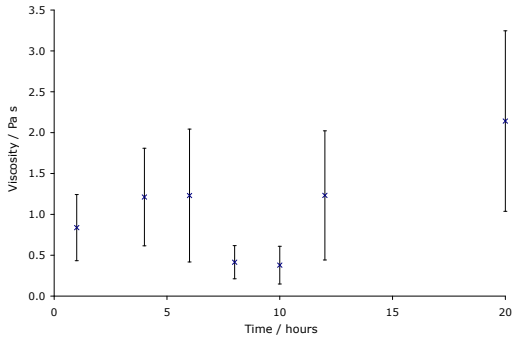

(e) Cell 1: Viscosity

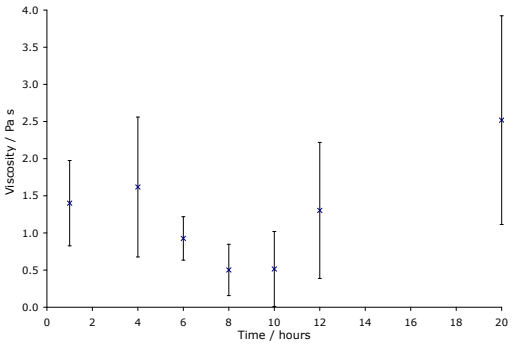

(f) Cell 2: Viscosity

Figure 5.6: Graphs showing the average diffusion coefficient for cell 1 (a) and cell 2 (b), the average size of the lipid droplets over the course of infection for cell 1 (c) and cell 2 (d) and the effective viscosities for cell 1 (e) and cell 2 (f). Error bars indicate 1 standard deviation.

that the cellular properties are altered during the intermediate stage of infection such that the effective viscosity decreases. The effective viscosity then increased to 2.14 Pas and 2.52 Pas for cell 1 and cell 2 respectively at 20 hpi, which is approximately double the viscosity at the

start of infection. Referring to Figure 5.4(g) which corresponds to 20 hpi, it is evident that the cells are in the late-stage of infection as the cellular membrane has adopted a completely rounded morphology. It is possible that the increase in the effective viscosity of the cytoplasm at this stage of infection could be associated with the rounding of the cell, which is correlated with changes in the internal structures and organelles as cell death begins. It is known that the process of apoptosis starts with condensation of the nucleus and cytoplasm (120), which results in cytoplasmic organelles becoming abnormally close packed (121). As such, it is expected that the effective viscosity inside the cell would increase, and is corroborated by a study by Kuimova et al. where intracellular viscosity were found to increase during photoinduced cell death (122).

Next it was investigated whether any significant variations regarding the trajectories exhibiting directed motion could be seen during the course of infection. Only trajectories consisting of three or more consecutive points were analysed. This step was applied in order to filter out the false tracks that arose occasionally when the Mtrack2 algorithm falsely assigned a trajectory between two frames by connecting two different particles. The trajectory segments were separated depending on the direction of motion because the molecular motors that transport the lipid droplets only travel in one direction, therefore different motors are responsible for transport in a specific direction (73, 74). There are three different classes of molecular motors known as myosin, kinesin and dynein which operate along two intracellular transport networks known as the microtubule network and the actin network. The microtubule network is polarized, with the plus end towards the cell periphery and the minus end towards the nucleus, whereas the actin network can be randomly orientated (72). Myosin motors move along actin filaments, kinesin motors move towards the plus end of the microtubules and the dynein motors move towards the minus end. With the data available, only approximate directional information could be extracted because the different networks could not be identified from the DIC images, however, this was not an issue because the focus of the analysis is to assess the lipid droplet trajectories rather than the molecular motor activities. The trajectories were sorted on the basis of whether the movement was towards or away from

the nucleus. This was deemed to be acceptable because the important criteria was to ensure that the trajectories facilitated by kinesin motors were not combined with the trajectories facilitated by dynein motors. It has to be noted that the separated trajectory segments may also comprise trajectories moving along the actin networks.

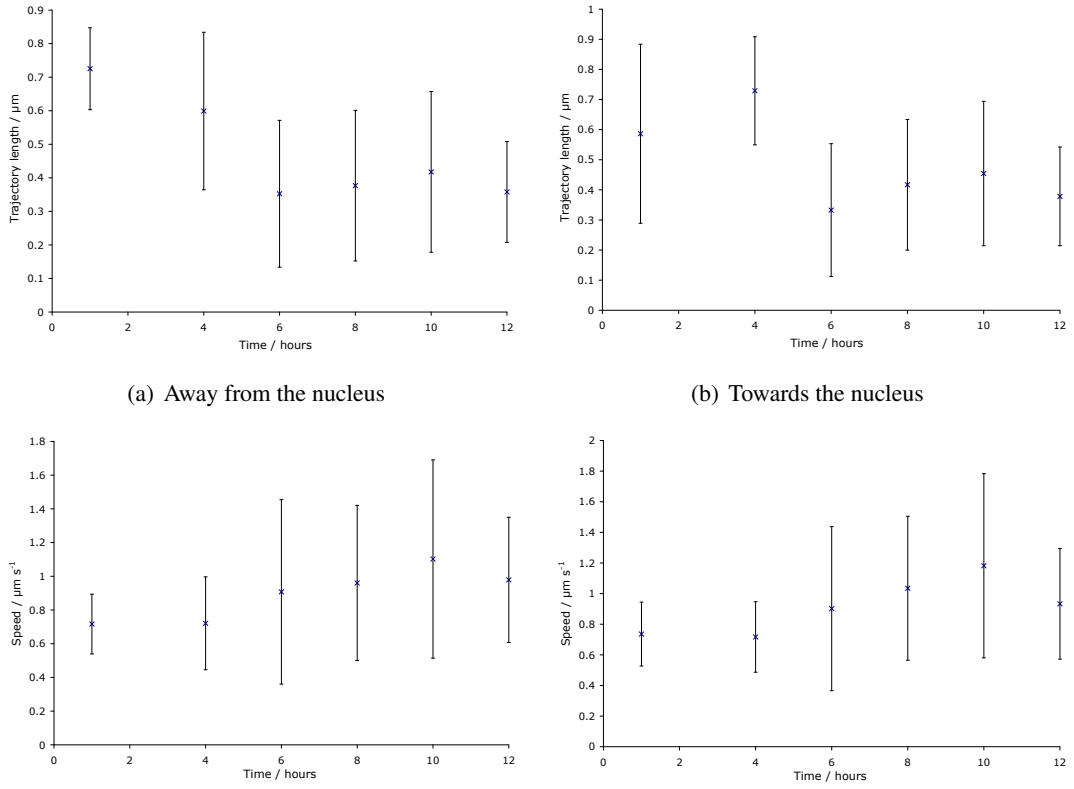

(a) Away from the nucleus

(b) Towards the nucleus

(c) Away from the nucleus

(d) Towards the nucleus

Figure 5.7: Graphs showing the average trajectory length for lipid droplets exhibiting directed motion away (a) and towards (b) the nucleus, during the course of infection. The average speeds for the trajectories away (c) and towards (d) the nucleus is also shown. Error bars indicate 1 standard deviation.

The graphs in Figure 5.7 show the average trajectory length and the average movement speed for trajectory segments exhibiting directed motion, towards and away from the nucleus. Only the results for cell 1 are presented because the results for cell 2 were similar. Referring to Figure 5.4(g), it is evident that the position of the nucleus is difficult to ascertain, and the cellular structure is disrupted, therefore the data points at 20 hours were disregarded because the same method for sorting the trajectory segments could not be applied to these images.

Figure 5.7(a) and (b) show that the average trajectory length seems to decrease during the course of infection with the average trajectory lengths in the first four hours after infection, decreasing from between 0.5 μm and 0.7 μm to between 0.3 μm and 0.5 μm, with no significant differences between the trajectories moving towards or away from the nucleus. The error bars which show one standard deviation are large, indicating that the data covers a wide variation in the measured trajectory lengths. The graphs in Figure 5.7(c) and (d) show that the average speed of the trajectories seems to increase gradually from 0.7 μms^{-1} to 1.2 μms^{-1} within the first 12 hours post infection, however the error bars indicating the standard deviation of the data sets are much larger than the apparent increase in the average values.

An issue with single cell analysis is that for each data point, only the lipid droplets from the one cell are analysed, which does not provide a large statistical sample especially when the variations within a single cell are large (N between 42 and 84 trajectories for each time point). With regards to the study of diffusive trajectories, it is already known that the intracellular viscosity is non-uniform, with the microviscosities varying widely throughout the cell. As such, it is unsurprising that the diffusion coefficient, and therefore the viscosity results would exhibit a wide distribution. Similarly, with regards to the directed trajectories, the dependence on molecular motor activity as well as the microtubule network would naturally introduce variations. For example, the molecular motors operate by hydrolysing ATP (73), therefore the number of steps is related to the amount of ATP available locally, and could possibly be affected by the viral infection.

Another method of analysis is to analyse a large sample of healthy and infected cells and therefore assess whether an ensemble variation can be identified between the two samples. This method is ideal alongside single cell analysis because the assessment of an ensemble enables variations in the population to be analysed whereas single cell analysis enables cellular variations to be detected. The following results in this chapter will study and compare the lipid droplet dynamics between groups of healthy cells, infected cells and cells in the late-stage of infection, where cells belonging to the infected group were measured between 3 and 12 hours post infection and the cells in the late-stage infected group were measured after 20 hours

post infection, at which point the cell morphology had become rounded in shape. Healthy (uninfected) cells were cultured and imaged separately, where image sequences of a sample of cells were taken within 12 hours of being placed onto the microscope stage (inside the live cell chamber).

5.4.3 Effect of mCMV infection on lipid droplet diffusion

For each group, 15 cells were analysed in order to study whether lipid droplet dynamics are affected by mCMV infection. The numbers of diffusive trajectories to which the analysis was applied for healthy, infected and late-stage infected cells were 1135, 963 and 1124 respectively.

To confirm that the trajectories were diffusive, the exponent values were calculated. A graph showing the average exponent values and standard deviation for healthy, infected and late-stage infected cells are displayed in Figure 5.8, where the average values are 0.8, 0.9 and 0.9 respectively and the error bars showing the standard deviation of the data indicate that the population of lipid droplets exhibited a range of diffusive modes. There were no significant differences in the results between healthy, infected and late-stage infected cells, with each data set exhibiting a similar range of diffusive modes.

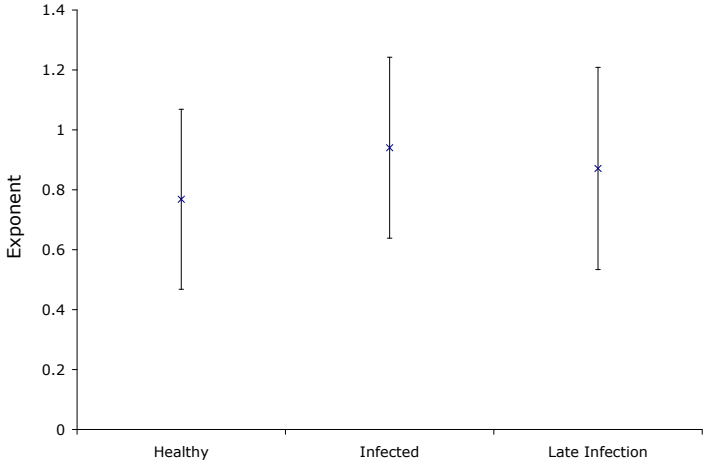

Figure 5.8: A graph showing the exponent values for healthy, infected and late-stage infected cells. Error bars are 1 standard deviation of the data sets

The diffusion coefficients were determined using MSD analysis and a histogram was

plotted for each of the data sets. Figure 5.9(a), (b) and (c) shows the probability distribution of D for healthy, infected and late-stage infected cells respectively. Using the analysis software, IGOR Pro, a lognormal fit was applied to the histograms to enable the probability distribution to be analysed. Table 5.1 shows the peak and average values of D for healthy, infected and late-stage infected cells respectively. It is clear from the probability distributions that the diffusion coefficients measured in the infected cells are significantly different to those measured for the healthy and late-stage infected cells, where the peak position in the probability distribution of infected data is at a higher D than for healthy and late-stage infected cells. Both the peak and average values of D are more than double, which indicates that the population of infected cells as a whole exhibits a significant increase in D. This is also confirmed by the shape of the histograms, with the data sets belonging to healthy and late-stage infected cells displaying a much sharper peak indicating that the majority of the population have lower values of D than in the infected cells.

	Healthy	Infected	Late-stage infection
Peak from fit curve $D/\mu m^2 s^{-1}$	$0.34(1) \times 10^{-3}$	$0.77(3) \times 10^{-3}$	$0.30(1) \times 10^{-3}$
Average $D/\mu m^2 s^{-1}$	$0.8(2) \times 10^{-3}$	$2(3) \times 10^{-3}$	$0.8(2) \times 10^{-3}$

Table 5.1: Table showing the peak positions of the lognormal fit curve on the histograms showing diffusion coefficients, D, for healthy, infected, and late-stage infected cells, where the figures in the parenthesis show the standard deviation of the data.

The changes in diffusion coefficient, mirrors the results found from the single cell study, and therefore confirms that the effects of mCMV infection on the diffusive behaviour of lipid droplets can be seen in a cell population as well as within a single cell, where the diffusive motion of the lipid droplets increases significantly as a result of mCMV infection.

An important question to assess is whether a relationship between the droplet size and the diffusive behaviour exists. The diffusion coefficient is dependent on both the effective viscosity of the media and the radius of the lipid droplet, therefore assessing whether the lipid droplet size has a direct influence on the diffusion coefficient will give an indication as to whether the droplet size or effective viscosity contributes most to the increase in diffusion coefficient measured. It is known that the size of lipid droplets vary within a cell, in addition

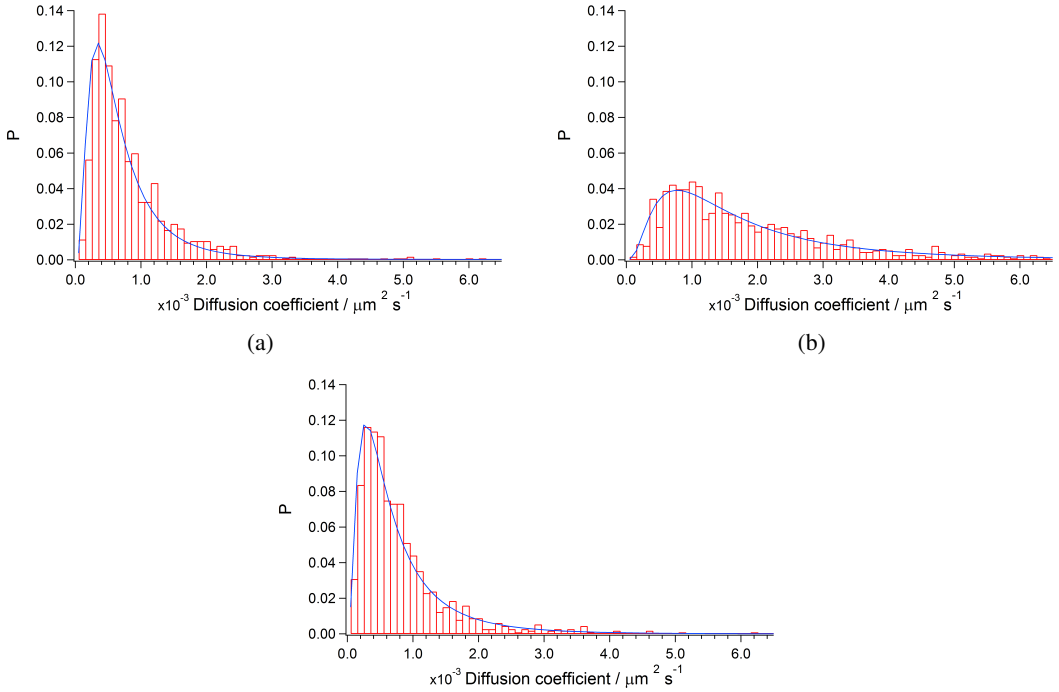

Figure 5.9: Histograms showing the probability distribution of diffusion coefficients calculated from the MSD of diffusive trajectories of healthy cells (a), infected cells (between 3 and 12 hours post infection)(b), and late-stage infected cells (after 20 hours post infection)(c). A lognormal fit was applied to the histogram. Sample sizes of 1135, 963 and 1124 for healthy, infected and late-stage infected data were used respectively.

to the measurement uncertainty due to both localization accuracy and the resolution limit. Figure 5.10(a), (c) and (e) shows the probability distribution of lipid droplet radii for healthy, infected and late-stage infected cells, where it is evident that the size distribution is Gaussian and peaks at approximately 0.23 μm. The distributions do not show a sharp cut-off towards the left of the Gaussian peak, which indicates that a large proportion of the droplet radii measured were not effected by the resolution limit. Interestingly, the probability distributions indicate that the population of lipid droplets do not increase in size due to infection, which is the converse of what was observed by CARS imaging. This discrepancy could be due to how well the imaging techniques are able to resolve two lipid droplets in close proximity. Referring to the CARS images of infected cells in Chapter 4, it can be seen that occasionally when the lipid droplets are clustered, the individual lipid droplets are not well resolved therefore two lipid droplets

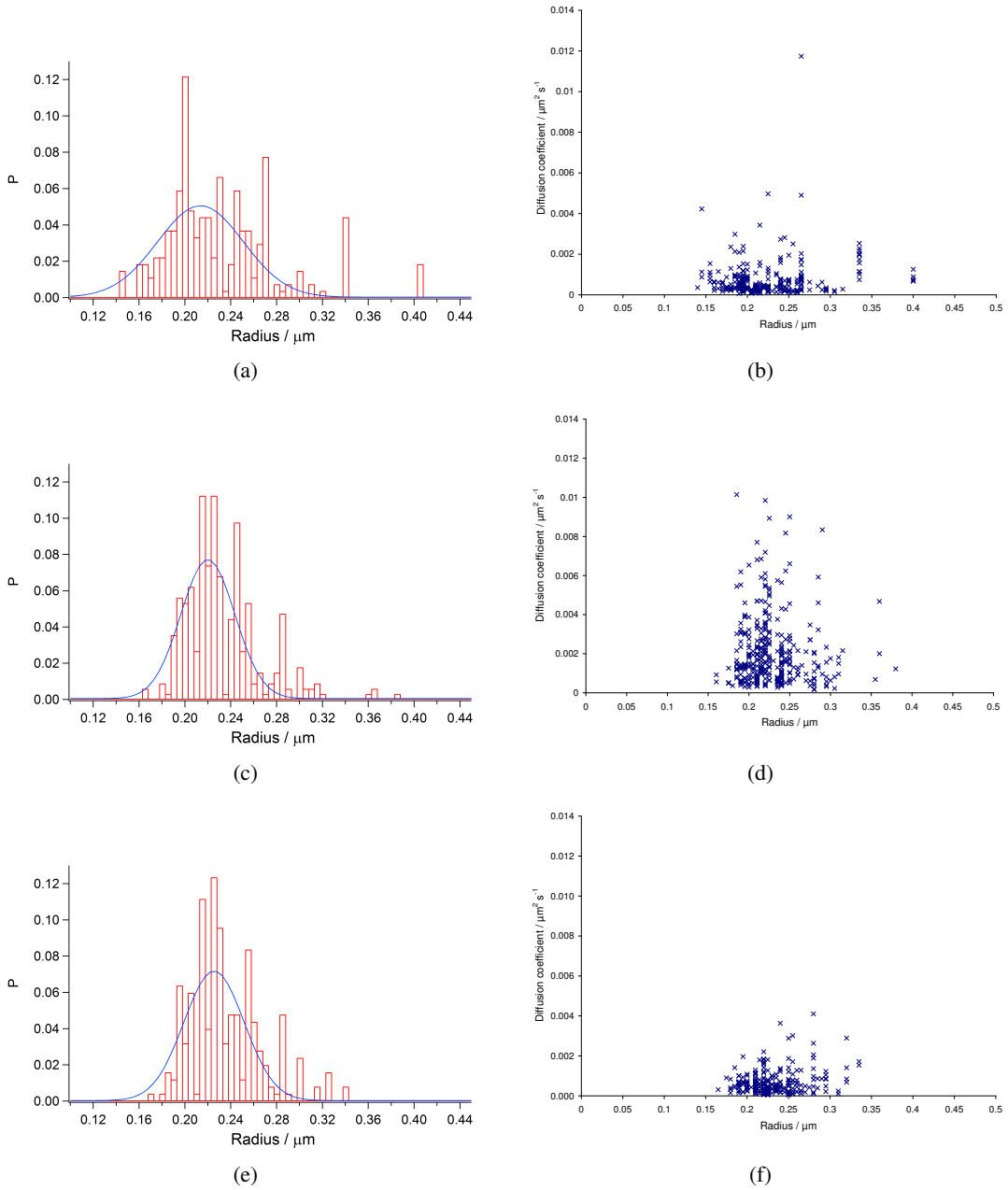

Figure 5.10: Histograms showing the probability distribution of lipid droplet size in healthy cells (a), infected cells (c), and late-stage infected cells (e) (A Gaussian fit was applied to the histograms.), alongside graphs showing the relationship between lipid droplet size and diffusion coefficient for healthy cells (b), infected cells (d) and late-stage infected cells (f).

may be measured as a single particle or the edges may be blurred affecting an accurate size determination. Finally, Figure 5.10(b), (d) and (f) show that there is not a simple $\frac{1}{r}$ correlation between D and measured lipid droplet radius. Based on the measurable dimensions of the lipid

droplets, the results indicate that the general increase in diffusion coefficient is not entirely dependent on the variation in lipid droplet size, implying that η is not constant (Equation 5.8).

Using the radius of the lipid droplets that were measured, and the diffusion coefficients that were determined, the average effective viscosities were estimated as $2.8(7)$ Pas, $0.9(8)$ Pas and $3.1(9)$ Pas for healthy, infected and late-stage infected cells respectively. The average viscosities for the infected cells are approximately a third of the viscosities for the healthy and late-stage infected cells, which indicates that the population of infected cells have a lower effective viscosity than the population of healthy and late-stage infected cells, mirroring the results from the single-cell study. This also suggests that the effective intracellular viscosities can be indirectly probed by analysing the diffusive motion of lipid droplets, whereas typical experiments involve incorporating fluorescent molecular rotary motors into the cytosol in order to specifically probe cellular microviscosities (117).

Figure 5.11 shows the probability distributions of the effective intracellular viscosities. However, due to the uncertainties regarding the measurement of the lipid droplet dimensions, caution must be exercised when making a definite conclusion about the effects of lipid droplet size and effective viscosities.

Interestingly, this finding suggests that mCMV infection causes changes to the intracellular properties, which results in a significant decrease in the effective viscosity of the cell. The intracellular viscosity is dependant on the viscosity of the cytosol, the number of macromolecules in the local region, and the cytoskeleton. Since the viscosity of the cytosol is known to be similar to water, it can be speculated that a significant reduction in the effective viscosities is related to a change in the ordering and structure within the cell, such as a reduction in local crowding experienced by the lipid droplet.

5.4.4 Effect of mCMV infection on the directed transport of lipid droplets

The lipid droplet trajectory segments exhibiting directed motion were analysed for a population of healthy and infected cells to determine whether the directed transport of lipid droplets is affected by mCMV infection. The study will compare the lipid droplet trajectories moving

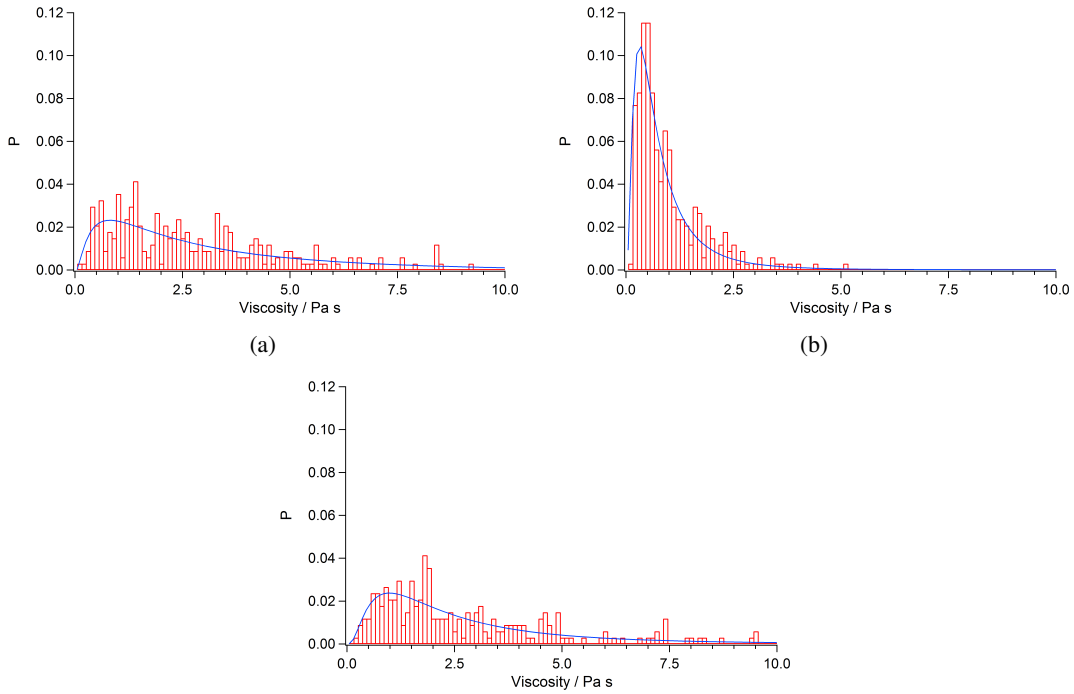

Figure 5.11: Histograms showing the probability distribution of the effective intracellular viscosity of healthy cells (a), infected cells (b), and late-stage infected cells (c). A lognormal fit was applied to the histogram.

away and towards the nucleus for healthy cells, with trajectories moving away and towards the nucleus for infected cells, where the numbers of trajectories analysed are 476, 470, 783 and 770 respectively. As discussed earlier, when the cells are in the late-stage of infection, the change in cell morphology makes it difficult to determine the location of the nucleus so the same method for sorting the directed trajectories can not be applied, as such, the late-stage infection data were excluded.

Considering the trajectory speed distributions shown in Figure 5.12, it is clear that there is a wide range of speeds across the data sets. In part this is due to the inherent variability in live cell studies, but there appears to be a systematic difference between healthy and infected cell distributions where the infected cell distributions are wider than those from healthy cells. Table 5.2 show the peak values, the maximum values and the average and standard deviation of the trajectory speeds. It is evident from the standard deviation of the data set, which is denoted

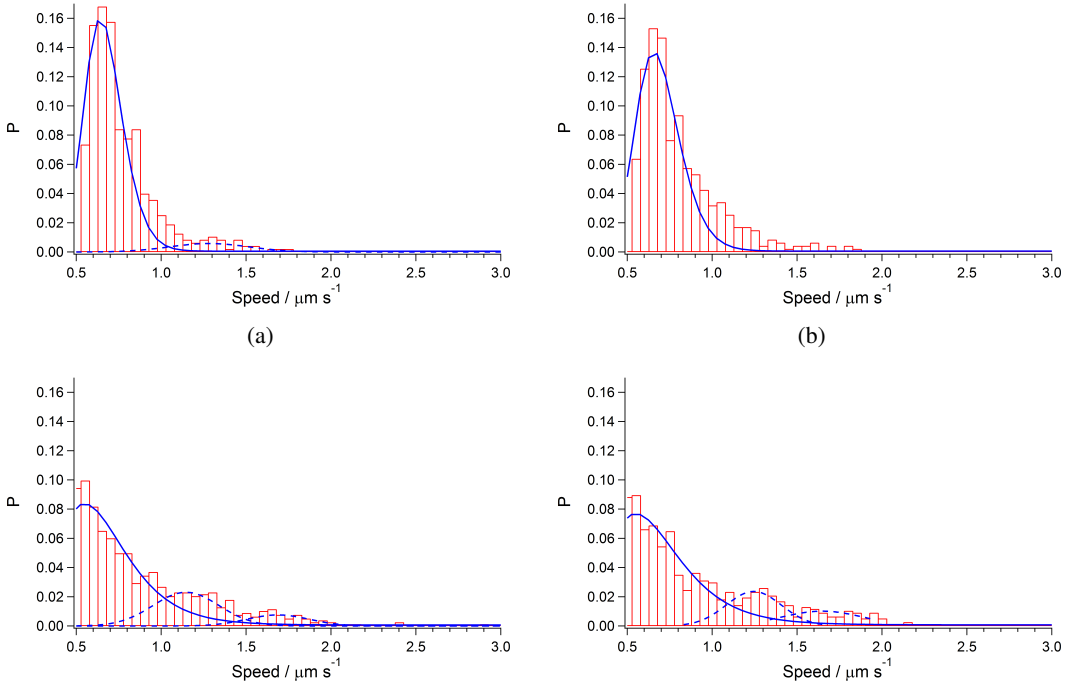

Figure 5.12: Histograms showing the probability distribution of trajectory speeds for lipid droplets undergoing directed motion in healthy cells moving away from (a) and towards (b) the nucleus; and in infected cells, moving away from (c) and towards (d) the nucleus. A Gaussian fit was applied to the histograms.

in the parenthesis next to the average speeds, that the distribution for infected cells is twice as wide as for the healthy cells. Although the average and peak values of the distributions do not show significant differences, the maximum trajectory speeds of 2.9 μms^{-1} and 2.9 μms^{-1} for the infected cells moving away and towards the nucleus respectively are significantly larger than the corresponding values of 1.7 μms^{-1} and 1.9 μms^{-1} for healthy cells, where approximately 5% of the population of the trajectory speeds in the infected cells were greater than 1.7 μms^{-1}.

The average trajectory speeds were found to be 0.8 μms^{-1}, which is interesting as various studies have found that the typical speeds of kinesin motors when attached to cargo molecules *in vivo* are $0.7 - 0.8$ μms^{-1} (123, 124). This suggests that the trajectory speeds measured in this study can be correlated to molecular motor activity, which is feasible as lipid droplets have previously been utilised in order to study the stepping behaviour of kinesin and dynein

	Healthy (away)	Healthy (towards)	Infected (away)	Infected (towards)
Peak from lognormal fit: trajectory speed μms^{-1}	0.7	0.7	0.6	0.6
Average trajectory speed μms^{-1}	0.8(2)	0.8(2)	0.8(4)	0.9(4)
Max trajectory speed μms^{-1}	1.7	1.9	2.9	2.9
Secondary peak μms^{-1}	1.3	-	1.2	1.3
Tertiary peak μms^{-1}	-	-	1.7	1.7

Table 5.2: Table showing the peak values from the lognormal fit of the probability distributions, the average and maximum values, and the secondary and tertiary peaks (when measurable) of trajectory speeds away and towards the nucleus for healthy and infected cells. Standard deviation is denoted in parenthesis.

motors (125). By comparing the results with those in the literature, the speeds measured are in agreement with those found in other studies. Kural et al. looked specifically at the movement of kinesin and dynein motors, where the motors transporting peroxisomes were tracked and the effects of coordinated movement were assessed (126). By tracking the peroxisomes, they were able to directly measure the speed of kinesin and dynein motors and concluded that depending on the type of cargo, if multiple dyneins and kinesins are involved, the transport speed can reach up to 12 μms^{-1}. Jungst et al. studied the lipid droplet motion in (healthy) HeLa cells and concluded that the droplets were rarely found to travel at speeds greater than 1 μms^{-1} (111), with average speeds measured to be 0.531 μms^{-1} for directed transport. Comparing the lipid droplet speed distributions from healthy cells in Figure 5.12(a) and (b) with the speeds measured by Jungst et al. confirms that the results measured for the healthy cells are in agreement, and as a result, the increase in the trajectory speeds and the differences in the probability distributions measured in the infected cells can be undoubtedly attributed to the effects of mCMV infection.

In addition to the main peak which appears at approximately 0.6 μms^{-1} and 0.7 μms^{-1} in the probability distributions of trajectory speeds shown in Figure 5.12, there is a small secondary peak at approximately 1.3 μms^{-1} which is more prominent in the infected cells, with the infected cells also exhibiting a tertiary peak at 1.7 μms^{-1} (Figure 5.12(c) and (d)).

Coordinated motion is common with regards to directed transport of molecules around the cell, where multiple motors attach onto a single cargo molecule and can contribute to increasing the rate of movement (127, 128). Previous studies have shown multiple peaks in the transport speed distributions (126), similar to the peaks shown in Figure 5.12, which correspond to transport involving multiple motors, whereby coordinated motion was found to significantly increase the transport speed compared to motion involving a single motor. This suggests that the molecular motor activity is affected by mCMV infection, in which the rate of directed transport of lipid droplets is significantly increased, with a larger proportion of lipid droplet transport occurring via coordinated motion involving a greater number of motors than for healthy cells. Considering the probability distributions of lipid droplet speeds in healthy cells between 0.8 µms^{-1} to 0.9 µms^{-1} (Figure 5.12(a) and (b)), it is possible that another distinct peak is present in the shoulder of the probability distribution (not detected by the peak fitting algorithm), which could also be present in the distribution for the infected cells, and could be indicative of a second type of molecular motor mediated transport.

Lastly, the proportion of trajectories undergoing directed versus diffusive motion was analysed to address the observation that the lipid droplets in the infected cells appeared to be more mobile than in healthy cells. Table 5.3 shows the proportion of the trajectories that were separated into directed or diffusive trajectory segments in terms of a percentage. It is clear that a greater proportion of trajectories measured in the infected cells were undergoing directed motion, with 44% showing directed motion compared with only 29% in healthy cells.

	Healthy	Infected
% diffusive motion	71%	56%
% directed motion	29%	44%

Table 5.3: Table showing the proportion of trajectories measured which exhibited diffusive motion versus directed motion for healthy and infected cells.

In summary, from analysing the directed trajectories, it can be concluded that lipid droplet in cells infected with mCMV exhibited a greater tendency to travel at higher speeds than lipid droplets in healthy cells. In addition, peaks in the probability distributions at speeds greater than 1 µm s^{-1} were found to be significantly more prominent for the infected cells than for the

healthy cells, suggesting that directed transport involving multiple motors is more probable in the infected cells.

5.4.5 Lipid droplet clustering

In Chapter 4, CARS images of infected cells displayed higher degrees of lipid droplet clustering. The final section of this chapter will focus on assessing and quantifying this observation.

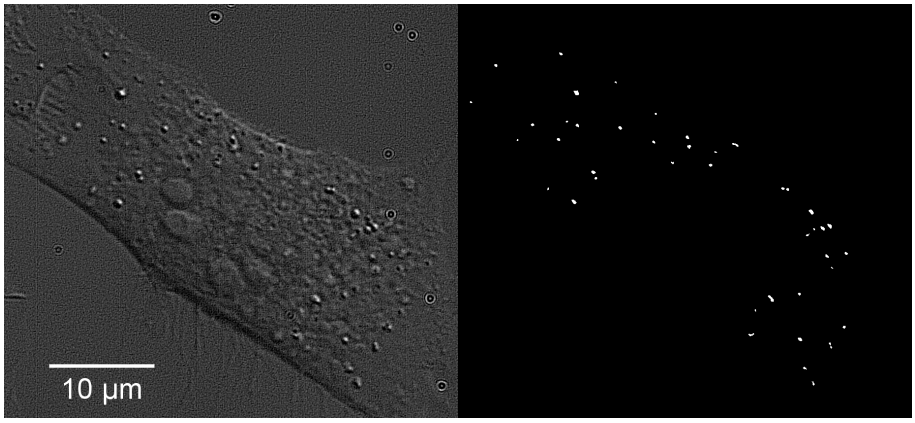

(a)

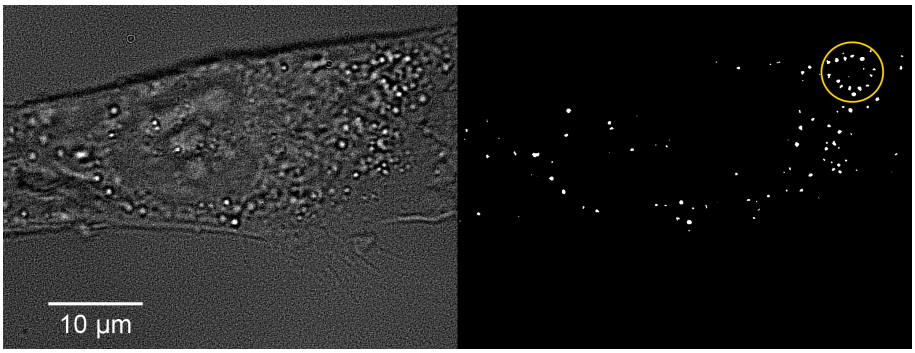

(b)

Figure 5.13: DIC and the corresponding thresholded images of a healthy cell (a) and an infected cell (b). A typical circular arrangement of lipid droplets in the infected cells is depicted by the yellow ring. Contrast enhancement was applied to the DIC images for display purposes only.

Figure 5.13 shows typical DIC images of healthy and infected cells, alongside the corresponding thresholded images. It is evident that the lipid droplets in the infected cells appear to be more clustered than in the healthy cell. Interestingly, lipid droplets in the infected

cells were often observed to be arranged in a circular pattern, as depicted by the yellow ring in Figure 5.13(b). In addition, it was possible to see individual lipid droplets being actively transported towards lipid droplet clusters. These qualitative observations suggest that the mCMV infection induces a form of order to the arrangement of the lipid droplets, where droplets are prone to arrange in a circular pattern, and are actively directed to form clusters.

As discussed earlier, lipid droplets are easily depicted in DIC images of fibroblast cells. Referring back to the CARS images of infected cells shown in Chapter 4, it can be seen that the individual lipid droplets within lipid clusters are not well resolved, whereas individual droplets can be distinguished in DIC images. Consequently, analysis of lipid droplet clustering is feasible using DIC images, since individual lipid droplet positions can be easily determined, regardless of the degree of clustering.

The purpose of this analysis is to compare the lipid droplet clustering between healthy and infected cells. To analyse clustering, the radial distribution function was used to assess the lipid droplet density within the cells. The radial distribution function, $g(r)$, describes how the lipid droplet density, $\rho(r)$, varies as a function of distance, r, from each droplet, where,

$$\rho(r) = \rho g(r) \tag{5.9}$$

where ρ is the average density of the droplets in the system and,

$$g(r) = \frac{A}{N}\frac{n(r)}{A(r)} \tag{5.10}$$

where A is the total area of the cell, N is the total number of lipid droplets in the cell, $A(r)$ is the area of the shell with radius r, and $n(r)$ is the number of droplets within the shell with radius r. It can be expected that a graph of the radial distribution function of cells containing more lipid droplet clusters would show larger peaks at small distances than for cells containing less clusters, as the rdf function gives a measure of the particle density as a function of the radial distance. Therefore, a cluster of lipid droplets would exhibit a high particle density at short radial distances.

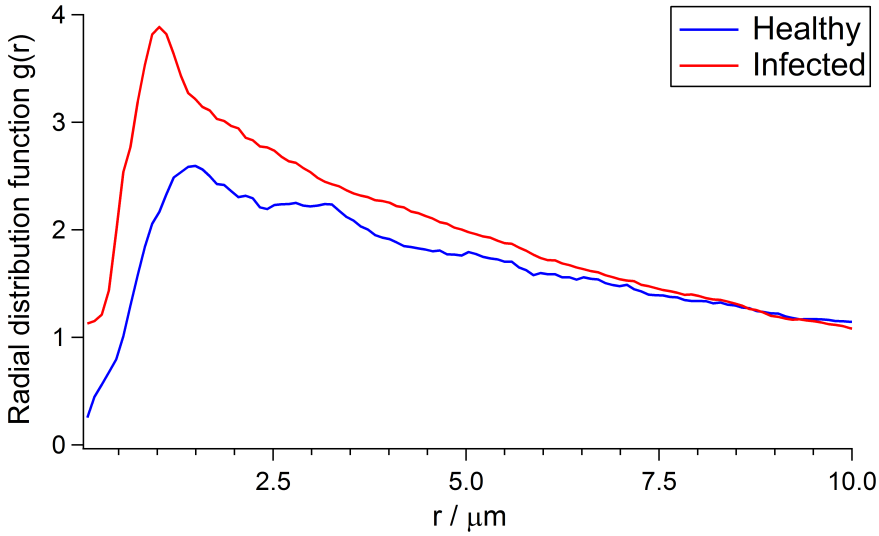

Figure 5.14: Graph showing the radial distribution function, g(r), of lipid droplet density for healthy and infected cells.

Figure 5.14 shows the radial distribution function of lipid droplet density as a function of distance for a group of healthy and infected cells. 20 healthy cells and 27 infected cells were analysed, where the number of lipid droplets within annular increments of 2 pixel radius were measured for every droplet. In this way, the average droplet density surrounding each droplet for the group of cells was calculated, and plotted as a radial distribution function. It is evident from Figure 5.14 that the rdf plot for the infected cells exhibits a sharper peak at a smaller r than for the healthy cells, with the peaks lying at 1.0 μm and 1.5 μm respectively, indicating that the infected cells exhibit a higher degree of droplet packing at smaller radial distances than the healthy cells.

It is evident that the rdf plots do not exhibit regular peaks and troughs. This confirms that the system described is disordered (129). Typically, the particle density and packing around the reference particle can be assessed by analysing the peaks and troughs of the radial distribution function curve, where the area under the curve from trough to trough gives the coordination number and therefore determines the number of nearest neighbours within the radial shell. Since the rdf plots of lipid droplet densities do not show definite shells, the area underneath the curve at various distances from the origin was assessed to estimate a coordination number at a

specific distance from the reference particle.

By measuring the approximate dimensions of lipid droplet clusters from the DIC images, it was found that an average cluster tended to cover a region with a diameter of approximately 5 µm. Therefore, the coordination numbers for radial distances between 0.35 µm, which is the minimum diameter of the lipid droplets, and 5 µm were calculated. Table 5.4 shows the coordination number at various radial distances for the healthy and infected cell data.

r / µm	Healthy	Infected
0 - 0.35	0.1	0.3
0.35-2.0	3	5
0.35-3.0	6	8
0.35-4.0	8	10
0.35 - 5.0	9	12

Table 5.4: Table showing the coordination numbers of lipid droplets in healthy and infected cells

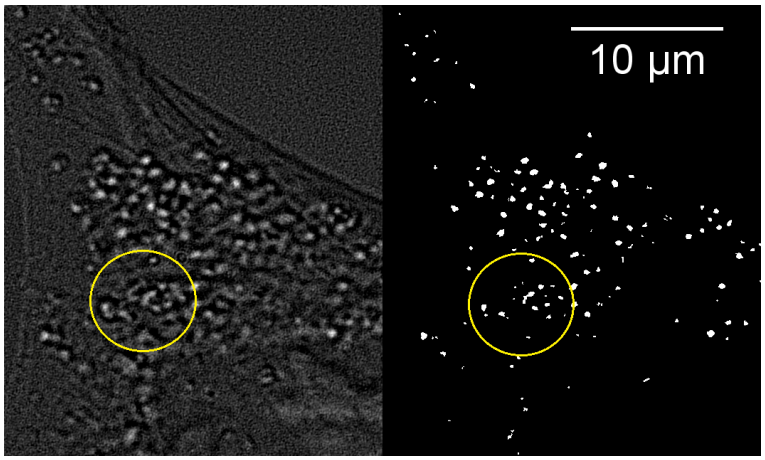

Figure 5.15: DIC image of a section of an infected cell, where yellow circles show possible lipid droplet coalescence. Contrast enhancement was applied to the DIC image for display purposes only.

Noticeably, the area under the rdf plots at $r < 0.35$ µm are not zero. The coordination number at a distance between 0 to 0.35 µm is 0.1 and 0.3 for the healthy and infected cells respectively. For this radial shell, the expected coordination number is zero as $r < 0.35$ µm is smaller than the diameter of the measured lipid droplets. Two possible explanations for this are that if the lipid droplets coalesce, two particles could be detected within 0.35 µm

radial distance. Figure 5.15 shows a section of an infected cell where the region marked with a yellow circle shows a group of clustered lipid droplets. It can be seen in the DIC image that coalescence of the droplets is not evident. Therefore the alternate explanation is that the particle thresholding may have introduced an uncertainty to the precise location of the lipid droplets. It can be seen that in the thresholded image, the droplets are not perfectly spherical, however the particle detection algorithm assumes a spherical particle in order to detect the centre and therefore introduces an error when measuring the nearest neighbour particles at small distances. To ensure that this error does not affect the results at distances greater than 0.35 μm, the threshold settings were varied and the lipid droplet positions were identified using the new parameters. It was found that the threshold parameters could vary up to 7% without affecting the shape of the rdf plots, confirming the validity of the distributions at radial distances greater than 0.35 μm are acceptable.

Referring back to Figure 5.4, it can be seen that the coordination number is consistently greater for the infected cells for increasing radial distances of between 0.35 μm and 5 μm, where the ratio between the healthy and infected coordination numbers are approximately 3:4. This confirms the qualitative observation that the lipid droplets in the infected cells exhibit a greater tendency to cluster than in healthy cells.

5.5 Conclusion

DIC imaging facilitated continuous imaging of live fibroblast cells, which enabled lipid droplets to be easily identified and tracked, whereby combining single cell and bulk sample analysis of healthy and mCMV infected cells, a more complete study of the effects of mCMV infection on lipid droplet dynamics was achieved. It was found that the lipid droplet trajectories were composed of two modes of motion which were characterised and separated into trajectory segments of diffusive motion and directed motion, allowing the modes of motion to be analysed separately.

By analysing the diffusive trajectory segments of a population of cells, the diffusion coefficients were found to be significantly higher in the infected cells than in the healthy cells,

with D being $20(19) \times 10^{-4}$ μm^2 s^{-1} and $8(9) \times 10^{-4}$ μm^2 s^{-1} respectively. The changes in diffusion coefficient were mirrored by the results found in the single cell study, confirming that the effects of mCMV infection on the diffusive behaviour of lipid droplets is detectable in both a cell population as well as within a single cell. As such, it can be concluded that the diffusive motion of the lipid droplets increases significantly as a result of mCMV infection.

Since the diffusion coefficient is dependent on both the radius of the lipid droplet and the effective viscosity of the media, it was important to assess whether the lipid droplet size had a direct influence on the diffusion coefficient. The probability distributions of the lipid droplet radii was found to be Gaussian in shape, with no evidence of a drastic cut-off towards the left of the distribution that would have indicated problematic resolution-limit effects. This suggested that the majority of the lipid droplet population exhibited sizes that are greater than the resolution limit. Additionally, the graphs showing the relationship between D and droplet size do not exhibit a simple $\frac{1}{r}$ trend, indicating that D is not solely dependant on the radius and so implies that the effective microviscosities are not constant. Using the measured lipid droplet radii and the diffusion coefficients, the average values of η were calculated to be 2.8 Pas for healthy cells and 0.9 Pas for infected cells, showing that the average effective viscosity in the infected cells is approximately a third of the average effective viscosity in the healthy cells. This result indicates that by analysing the diffusive trajectory segments of lipid droplet motion, the effective intracellular viscosities can also be probed, showing that mCMV infection affected the intracellular properties in such a way as to significantly decrease the effective viscosities. However, due to the uncertainties regarding the measurement of the lipid droplet dimensions (size of the lipid droplets are close to the resolution limit of the microscope system), caution must be exercised when making a definite conclusion about the effects of lipid droplet size and therefore the effective viscosities.

The lipid droplets in the infected cells exhibited a greater proportion of directed transport modes than diffusive transport modes, compared to the healthy cells. It is clear that the maximum speeds exhibited by the lipid droplets are significantly greater for infected cells, with maximum speeds of 2.9 μm s^{-1} measured compared to 1.7 μm s^{-1} measured in the

healthy cells, where approximately 5% of the population of the trajectories in the infected cells exhibited speeds $> 1.7\ \mu m\, s^{-1}$. Most interestingly, the directed motion of lipid droplets appear to be associated with molecular motor activity as the average measured speed of $0.8\ \mu m\, s^{-1}$ corresponds to the typical speed of kinesin motors when attached to cargo molecules *in vivo*. In addition, secondary and tertiary peaks at approximately $1.3\ \mu m\, s^{-1}$ and $1.7\ \mu m\, s^{-1}$ are evident in the trajectory speed distributions, suggesting evidence for coordinated molecular motor activity, where the peaks indicate that multiple motors act together to transport a single lipid droplet. These peaks are significantly more prominent for the infected cells, suggesting that mCMV infection affects the lipid droplet dynamics by increasing the rate of directed transport, and increases the proportion of motion that involves more than one molecular motor.

Finally, by analysing the radial distribution function of the arrangement of lipid droplets in healthy and infected cells, lipid droplet clustering has been measured, in which the infected cells are found to exhibit greater lipid droplet density at radial distances $< 5\ \mu m$ compared with the healthy cells. This result confirms the observations made from the CARS images of mCMV infection in Chapter 4, which suggested that infected cells exhibited a greater degree of lipid clustering. Furthermore, lipid droplets in the infected cells were often observed to be arranged in a circular pattern, and it was also possible to see individual lipid droplets being actively transported towards lipid droplet clusters. These qualitative observations suggest that the mCMV infection induces a form of order to the arrangement of the lipid droplets, where droplets are prone to arrange in a circular pattern, and are actively directed to form clusters. Further work is required to quantify and understand these observations.

In summary, the results of this study show that intracellular properties, such as the effective microviscosities and the molecular motor activity, can be probed by tracking and analysing both the diffusive and directed motion of intracellular lipid droplets. The main findings suggest that mCMV infection influences the arrangement of cellular lipid droplets, where the droplets appear to exhibit greater degrees of clustering and are also positioned in a much more ordered configuration within the cell. In addition, the results suggest that the viral infection increases the activity of the transport motors, and also effectively decreases the intracellular viscosity.

Part 2

Effects of antimicrobial peptides on membrane fluidity

6

Effects of antimicrobial peptides on bacterial membrane fluidity

6.1 Introduction

It is known that current antibiotics are losing effectiveness against bacterial infections. Many strains of pathogenic bacteria rapidly evolve a resistance to antibiotics, often within a couple of years after introduction (53). As a result, many research groups are involved in developing new antimicrobial agents to counteract the fast evolving bacterial strains, in addition to the many studies which focus on understanding the interactions between antimicrobial agents and bacteria (54). Currently, one major focus is the development and investigation of antimicrobial peptides (AMPs), which are host defence peptides that occur naturally in humans and animals, for example, the linear peptides such as magainin, found in frogs; and cecropin, found in insects such as the silk moth (130). The interest in AMPs stems from the possibility that bacteria may not be able to evolve a resilience against these agents, since AMPs have remained effective for millions of years in humans and animals (53). Most current theories assume that for antimicrobial peptides to kill bacteria effectively, they must disrupt the bacterial membrane, and although the precise mechanisms by which AMPs disrupt the membrane are still unknown, various modes including pore formation and the carpet mechanism have been

suggested (58) (59). Pore formation and the carpet mechanism are the two most common theories (54), and are of interest for this chapter in which the problem will be approached within a framework that suggests that bacteria maintain their membranes at an optimal state of membrane fluidity to counteract environmental and external stresses (45). As such, probing the membrane fluidity could provide insight into the effect of AMP interactions, with the hypothesis that severe disruption of the membrane would cause a drastic change in the membrane fluidity.

6.2 Background

As mentioned above, the emergence of antibiotic resistance in bacteria has led to a lot of effort being focused upon understanding the mechanisms by which antimicrobial peptides act to penetrate and disrupt bacterial membranes (60, 131). In this chapter, the interaction between models for the membranes of Gram-negative bacteria, such as *E. coli*, and a cationic antimicrobial peptide will be studied.

Gram-negative bacterial membranes typically comprise a mixture of zwitterionic and anionic lipids, where the anionic component makes up approximately 25% of the total lipid composition (49). The primary zwitterionic phospholipid has been identified as phosphatidylethanolamine (PE) and the primary anionic phospholipid as phosphatidylglycerol (PG) (61). One specific mechanism for membrane disruption suggests that certain antimicrobial peptides can cause the lipid components to separate, resulting in anionic lipid clusters and creating phase boundary defects (132). Phase boundary defects between coexisting gel and liquid crystalline domains are suggested to allow liposomes to leak (133). Furthermore, it is suggested that the formation of domains due to interaction with antimicrobial peptides occurs too rapidly for the membrane to rearrange itself. This could result in a change in the charge distribution and/or an increase in the membrane tension which cannot be counteracted: This change could then affect the conformational flexibility of the membrane, weakening the structure and allowing the membrane barrier to be breached.

This chapter will explore the hypothesis that antimicrobial peptides mediate lipid do-

main formation, modulating the lipid phase and thereby causing disruption to the bacterial membrane. Giant unilamellar vesicles (GUVs) were used as a simple model of the bacterial membrane so that attention could be focussed on any changes in the lipid phase. Bacterial membranes are complex and consist of a range of different lipids as well as various proteins. Using GUVs allowed the composition of the model bacterial membrane to be simplified and controlled. Although GUVs typically have diameters of between 10 μm and 100 μm (134), which is larger than *E. coli* (approximately 1 μm in diameter × 2 μm) it is assumed that the radius of curvature of *E. coli* is sufficiently large compared to the intrinsic curvature associated with the lipid molecules to make the effect of differences in curvature between GUVs and *E. coli* negligible (135).

6.3 Effects of AMP2 on DPPC/POPG GUV

The antimicrobial peptide, AMP2 (136) is a gene transporter (GeT) that has been found to also possess antimicrobial properties, and it is the effects on bacterial membranes that are of interest in this study. The linear sequence of AMP2 is based on a repeating pattern of CHNCHCN (136, 137), where C is cationic, H is hydrophobic and N is neutral and polar. This design promotes amphipathic alpha helix formation as the peptide binds to the surface of anionic membranes, in which the hydrophobic and polar residues segregate onto distinct regions of the peptide.

For this investigation, GUVs were produced to model the *E. coli* membrane where 1,2-dipalmitoyl-sn-glycero-3-phosphocholine (DPPC) was chosen as the zwitterionic phospholipid component and 1-palmitoyl-2-oleoyl-sn-glycero-3-phosphoglycerol (POPG) was chosen as the anionic phospholipid component. DPPC and POPG were chosen on the basis of their gel to liquid crystalline phase transition temperatures (T_m), which are $T_m = 41$ °C for DPPC and $T_m = -2$ °C for POPG (138, 139). As such, at room temperature, DPPC is in the gel phase (ordered lipid phase) and POPG is in the liquid crystalline phase[1] (disordered lipid phase) so it is expected that the lipids do not mix, forming domains instead in DPPC/POPG GUVs.

[1]The liquid crystalline phase is synonymous with the fluid phase L_α (140)

Changing the temperature allows the lipid fluidity to be manipulated and controlled. For this reason, DPPC was used instead of DPPE as the zwitterionic component, as T_m for DPPE is 71 °C, which would make it experimentally inconvenient to control the fluidity of the GUV using temperature.

6.3.1 Laurdan

Laurdan, 6-lauroyl naphthalene, is a polarity-sensitive fluorescent dye which typically aligns with its axis parallel to the acyl chain of the phospholipid, as shown in Figure 6.1, and is commonly used to probe lipid bilayer fluidity. In phospholipid bilayers, Laurdan is anchored to the hydrophobic core of the lipid bilayers, with its fluorescent moiety positioned adjacent to the phospholipid backbone (141). There is no evidence that the behaviour of Laurdan is influenced by the nature of the lipid headgroup (anionic, zwitterionic).

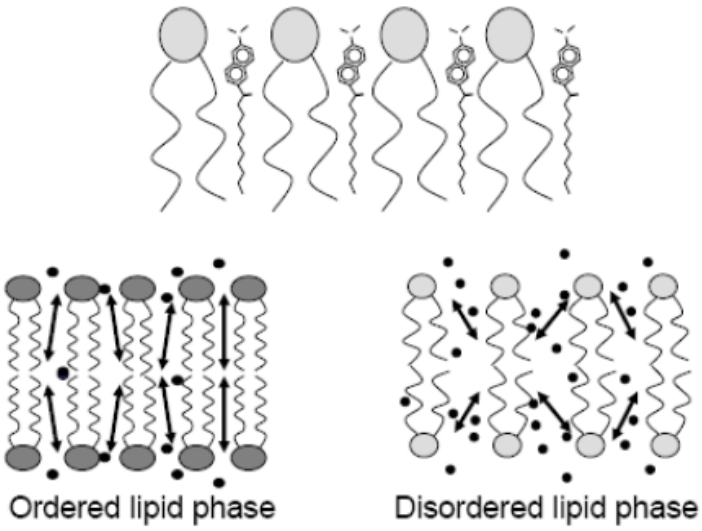

Figure 6.1: This diagram taken from the paper by Sanchez et al. (142), which illustrates the alignment of Laurdan molecules parallel to the acyl chains of the phospholid. The black dots illustrates the arrangement of water molecules surrounding the phospholipids for gel and liquid crystalline phase, which affects the emission spectra of Laurdan.

The property which makes Laurdan an interesting choice for this experiment is that its fluorescence spectrum is sensitive to the phospholipid environment (142, 143). Briefly, the

naphthlalene moiety possesses a dipole moment due to a partial charge separation between the 2-dimethylamino and 6-carbonyl parts of the Laurdan molecule. When Laurdan is in the excited state, the dipole moment drastically increases, and the presence of the dipole moment gives it the capability to reorient neighbouring polar molecules. In general, solvent molecules are excluded from the lipid bilayer, however when the bilayer is more fluid, the membrane permeability increases and as a consequence, the reorientation rate of the (polar) solvent molecules is faster than the emission process. Since energy is required to reorient the polar molecules, the resulting emission spectrum is red-shifted. As a result, the spectral shift of Laurdan emission gives an indication as to the fluidity of the lipid bilayer (144). An example of the fluorescence emission spectrum is shown in Figure 6.2.

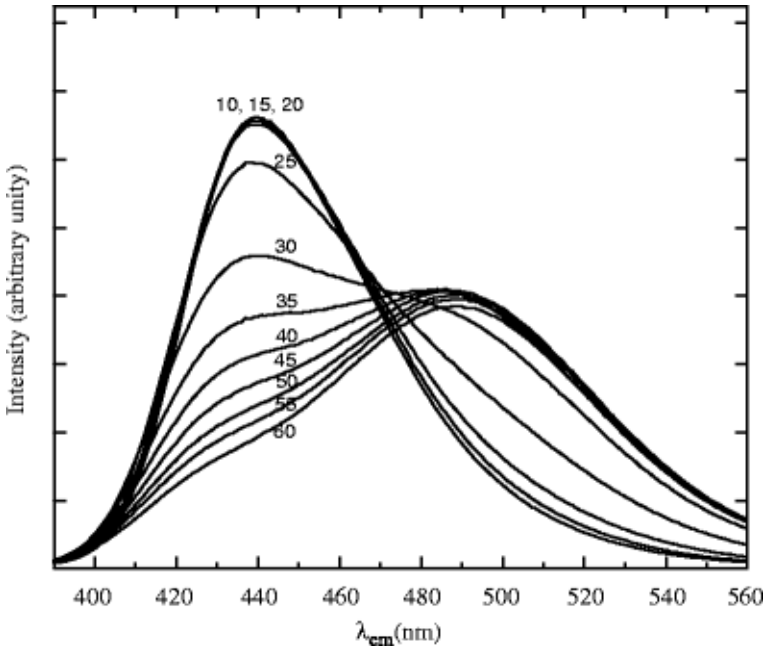

Figure 6.2: Fluorescence emission spectra (from ref. (144)) of DMPG bilayers incorporated with Laurdan at various temperatures (°C), where the temperature was used to change the fluidity of the membrane.

The excitation spectrum of Laurdan peaks at approximately 360 nm. Unsurprisingly, the emission spectrum is affected by the solvent polarity. For this experiment, water was used as the solvent, resulting in emission peaks from Laurdan in gel and liquid crystalline phase of 440 nm and 490 nm respectively (141).

6.3.2 General Polarization

General polarization (GP) is used to quantify the shift in the emission maxima of Laurdan (142), allowing the phase of the lipid bilayer to be identified. GP is defined by equation 6.1

$$GP = \frac{I_B - I_R}{I_B + I_R} \tag{6.1}$$

where I_B and I_R correspond to the intensities at the blue and red maxima of the emission spectrum, which in this case corresponds to the peaks at 440 nm and 490 nm.

Laurdan is homogeneously distributed within the lipid bilayer of the whole GUV, regardless of the lipid phase (145). As such, the whole membrane is detected and therefore calculating the GP gives a measure of the fraction of lipid bilayer that are in gel phase, liquid crystalline phase or gel/liquid crystalline coexisting phase. Theoretically, GP values can range from -1 to 1, however experimental values can vary depending on temperature and lipid composition, where previous studies have found that lipid bilayers in the gel phase typically exhibit experimental GP values between 0.5 and 0.6, and lipid bilayers in liquid crystalline phase exhibit GP values between -0.3 and 0.3 (142). Furthermore, Fahsel et al. stated that GP values for a lipid mixture of DMPC-DSPC were approximately -0.1 for homogeneous fluid phase vesicles, -0.1 to 0.5 for images with fluid and gel coexistence regions and approximately 0.55 for homogeneous gel phase lipids (145).

6.4 Method

In this study, GP values were calculated to enable the lipid phase domains of DPPC/POPG GUVs to be identified and quantified. This provides an indirect method to assess changes to the membrane fluidity and lipid domains.

GUVs composed of DPPC, and GUVs composed of POPG were first assessed to obtain a profile of the GP values expected for the individual lipid components. DPPC GUV's were analysed at temperatures of 25 °C, 35 °C, 45 °C and 55 °C to obtain a GP profile for DPPC from its gel phase through to its liquid crystalline phase. Subsequently, DPPC/POPG GUVs

were assessed at temperatures of 25 °C, 35 °C, 45 °C and 55 °C, which allowed the lipid fluidity to be modulated and the corresponding changes in the lipid phase domains to be visualised and analysed. Finally, DPPC/POPG GUVs were incubated with the antimicrobial peptide, AMP2 (136) at a concentration of 10 μM, which is the minimum inhibitory concentration (MIC) for this antimicrobial peptide (146), and the GP values were obtained. Assessment of whether AMP2 interaction causes changes in lipid fluidity and domains were made by comparing with the results obtained by manipulating lipid fluidity with temperature.

6.4.1 GUV formation

Giant unilamellar vesicles (GUVs) were produced by electroformation. Electroformation is a well established method, first developed in 1986 by Angelova and Dimitrov (147). Since then, various improvements and modifications have been made and specific details on various electroformation methods can be readily found (148). In this study, an electroformation cell using indium tin oxide (ITO) coated coverslips was constructed, and will be described in more detail later in this section. This method was used as it allows the GUVs to be produced at high yield (149) and imaged directly through the ITO coverslips using a high NA objective lens.

6.4.2 Lipid solutions

1.0 mM stock solutions of DPPC (0.7 mg/ml) and POPG (0.7 mg/ml) in chloroform were made. 1.0 ml aliquots of DPPC, POPG and a 3:1 DPPC:POPG lipid mixture (to mimic the 25% anionic lipid composition of bacterial membranes) were prepared from the stock solutions. 1.0 mol.% Laurdan (dissolved in chloroform) was added to these aliquots.

10 μM AMP2 was added to the solution after GUV formation, giving a lipid:AMP2 ratio of 100:1. AMP2 was designed, synthesized and characterized according to protocols published by Max Ryadnov, National Physical Laboratory (150). The peptide was identified by reverse phase high performance liquid chromatography (RP-HPLC) and MALDI-TOF mass spectrometry.

6.4.2.1 Electroformation

A customised chamber shown in Figure 6.3 was built in-house, which allowed for temperature control and imaging during electroformation of GUVs.

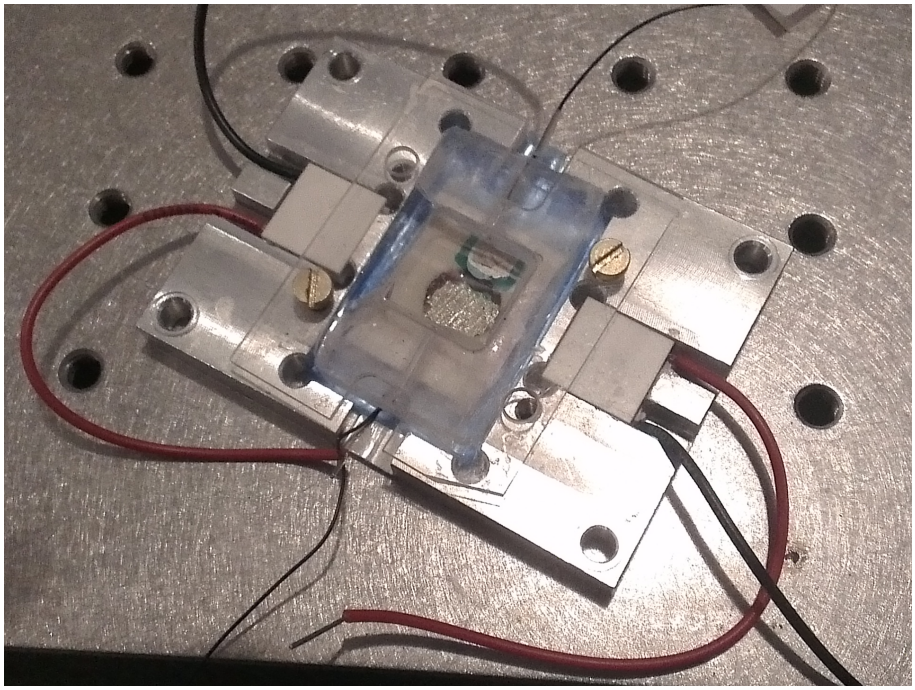

Figure 6.3: A photo of the GUV formation chamber. The chamber incorporates two Peltier heaters to enable temperature control. The ITO coverslips sandwich a 1.2 mm thick spacer and are gently clamped into the chamber; silver paint is used to provide electrical contact to the ITO. The design of the chamber also allows direct imaging of the GUVs during and directly after formation.

ITO coverslips of 20 mm $\times$ 20 mm, Number 1 thickness (0.13 - 0.17 mm) with a resistivity of 8 - 12 Ohms per square[2] were purchased from Diamond Coatings Limited. A small amount of silver paint was used to provide an electrical contact, allowing an AC voltage to be applied between the ITO plates. A pasteur pipette was used to deposit 2-3 drops of lipid solution onto the conductive surface of the coverslip. Using the tip of the pipette, the solution was spread evenly across the centre of the coverslip. Care was taken to ensure a thin, uniform coverage in order to promote optimal conditions for producing a high yield of uniform GUVs (148). The coverslip was then dried overnight in a vacuum desiccator.

[2]Ohms per square is the standard terminology to define the resistivity of the ITO coating, in which the unit of the square measured is irrelevant

GUVs are highly sensitive to osmotic pressure shocks making charged lipids more difficult to form into GUVs (149, 151). For this reason, a 200mM sucrose solution was used as the buffer in order to maintain the osmolarity at 200 mOsm. A cell was formed by sandwiching double sided foam tape of 1.2 mm thickness, with a cut-out of approximately 1 cm $\times$ 1 cm to contain the sucrose solution, between two ITO coverslips (one covered with the dried lipid film). It was important to ensure that no air bubbles were trapped between the plates as air bubbles can hinder GUV formation. The ITO plates were gently clamped into the chamber, which was fixed to the microscope stage in order to reduce any agitation that could disturb GUV formation. The lipid film must be heated past the transition temperature of the lipid with the highest T_m, as GUV formation can only occur if the lipids are in fluid phase. In this experiment, the chamber was heated to 55 °C for the formation of DPPC GUVs and mixed DPPC/POPG GUVs. POPG GUVs were formed at room temperature. Two Peltier heaters were incorporated into the chamber to provide heating and the ITO plates were connected to a Thandar TG215 function generator in order to apply a sinusoidal voltage between the plates. To improve the stability of GUVs, the initial ramp of the electric field was applied gradually. A 10 Hz sinusoidal AC field was generated at a starting voltage of 0.2 V and the voltage was incremented by 0.1 V every 10 minutes to 1.1 V. The voltage was then held at 1.1 V for a further 90 minutes. Finally, the temperature was lowered to the desired temperature ready for imaging.

Examples of DPPC/POPG GUVs formed using the electroformation cell are shown in Figure 6.4. The images were taken using a commercial, upright Nikon microscope, which was set up for phase contrast microscopy and single photon fluorescence (excitation provided by a mercury light source). A 470/30 nm band pass filter was used to filter the fluorescence emission signal. Non-uniform fluorescence is evident in the fluorescent images (left), where bright patches can be identified in the GUVs that correspond to the dark patches displayed in the phase contrast images (right). The emission filter allows red-shifted fluorescence signal to be detected, which occurs if the lipid bilayer is more fluid; as such the bright patches of fluorescence indicate lipid domains which exhibit greater fluidity. It is evident from

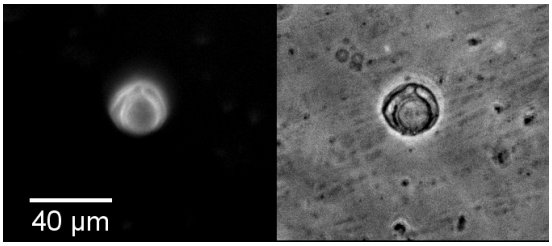

(a)

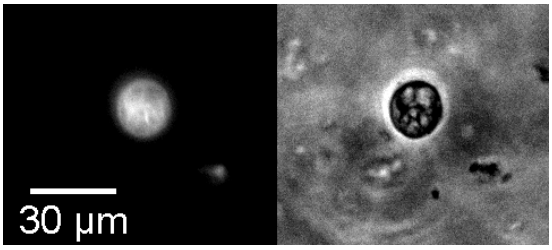

(b)

Figure 6.4: Images of two DPPC/POPG GUV incorporating Laurdan dye, at 25 °C, imaged using fluorescence microscopy (left) and phase contrast microscopy (right).

the fluorescence and phase contrast images that quantitative analysis of the lipid domains using these microscopy techniques is difficult, since both of the microscopy techniques allow detection of signals from the planes above and below the focal plane. In addition, photobleaching was a large issue with regards to single photon fluorescence as all the GUVs within the illuminated region of the sample suffered photobleaching effects. Consequently, two photon fluorescence (TPF) microscopy was used to acquire images of the GUVs for this study.

6.4.3 Imaging Technique

TPF microscopy was used to image the GUVs, using the imaging system detailed in Chapter 4. Benefits of TPF over single photon fluorescence microscopy are reduced photobleaching and photodamage to the GUVs. In addition, the mechanism of TPF is a non-linear process, in which only the focal volume is excited. As a result, optical sectioning is inherent, which ensures that the planes above and below the focal plane do not contribute to the overall image. Only one Ti:Sapphire laser was used as the excitation source, exciting at 720 nm with an average laser power of 42 mW measured before the scanning mirrors. A 100x oil 1.4 NA objective lens was used to focus the excitation light source onto the sample. Two narrow band pass filters centred

at 436/20 nm and 488/30 nm were placed in the forward and backwards detection channels respectively, allowing the emission peaks at 440 nm and 490 nm to be collected simultaneously, and the photomultiplier voltages were set to 747 V and 643 V respectively so that the detected images are visibly similar in contrast. Since two different detection channels are used, the emission intensities must be corrected for the difference in detection sensitivity between the channels. The sensitivity, S, is estimated as the ratio of the emission intensities measured in the forwards and backwards channels,

$$S = \frac{I_{Backwards,488\text{nm}}}{I_{Forwards,488\text{nm}}} \tag{6.2}$$

The GUV's were imaged immediately after formation at temperatures of 55 °C, 45 °C, 35 °C and 25 °C. The GUV's were then incubated with 10 µM AMP2 and incubated for 1 hour at room temperature before imaging at 25 °C.

Only the equatorial section of the GUVs were imaged to maximise the TPF signal intensity. The transition dipole of Laurdan in the lipid bilayer aligns parallel to the lipid tails (142) therefore strong excitation will only occur if the illuminating light is incident with the same polarization as the transition dipoles of the fluorescent probe. To this end, a quarter waveplate was used to convert the linearly polarized light into circularly polarized light to ensure strong excitation of the probe molecules around the membrane. The circularly polarized excitation source is polarized in the x-y plane, therefore strong excitation will only occur in the equatorial plane of the vesicle. As such, light illuminating the equatorial section of the GUV results in a bright fluorescent ring, which decreases in intensity for sections towards the poles of the GUV.

A consideration is that the spatial distribution of DPPC and POPG may not be uniformly distributed throughout the membrane of DPPC/POPG GUVs. One 2-dimensional slice of each GUV was imaged, so one image slice may not perfectly portray the domain structure of the whole GUV. Ideally, a 3-dimensional image stack of the GUV would enable the complete domain structure to be visualised, however for this study, acquisition of 3D image stacks was not possible due to time constraints, as only a manual method for scanning through the z-direction was available. Instead, by imaging and analysing a relatively large sample size of

GUVs, the sample of 2D image slices will be representative of the domain structure of the population of DPPC/POPG GUVs; considering the whole population effectively averages over the Euler angles, giving an average of all orientations of the GUVs.

6.5 Results

6.5.1 Image Analysis

Figure 6.5 shows an example of the GUV images collected in the backwards (488/20 nm) and forwards (436/30 nm) channels before and after image processing. The image processing software, ImageJ, was used to remove the background and noise from the raw images. The rolling ball algorithm was applied to subtract the background and also correct for any uneven illumination. The algorithm determines a local background value by averaging over an area encompassing several pixels (the ball) and this background value is then subtracted from the original image. Background subtraction was vital because the background levels for the two channels were different, which is evident in Figure 6.5(a) and (c). By subtracting the background intensities, the fluorescence signal can be measured from a zero baseline for each image, allowing comparison of the intensities in the two channels. After background subtraction, a 3×3 pixel median filter was applied to filter out noise in the image. The median filter operates by replacing each pixel value with the median of the grey-scale ranked values of the 9 neighbouring pixels. Since the noise was mostly salt and pepper single pixel noise, a median filter was deemed to be the ideal technique because it removes isolated noise whilst retaining sharp edges of features, as evident in Figure 6.5(b) and (d).

Figure 6.6 shows the intensity profile plots measured from the image of the GUV displayed in Figure 6.5 along the line from the bottom left corner to the top right corner of the GUV, as displayed in Figure 6.5(a). Figure 6.6(a) and (b) shows the intensity profile of the raw GUV images acquired from the backwards and forwards channel respectively. It is evident that before background subtraction, the signal measured in the backwards channel has a lower background level than the signal measured in the forwards channel; after applying background subtraction,

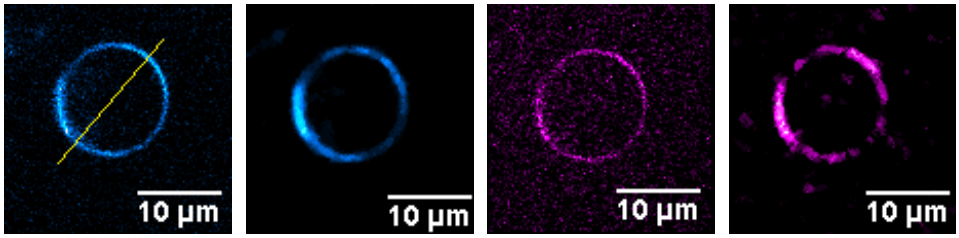

(a) (b) (c) (d)

Figure 6.5: Images of DPPC/POPG GUV at 25 °C before and after image processing. The raw images of DPPC/POPG GUV using 488/30 nm bandpass filter (a) and 436/20 nm bandpass filter (c) is shown, along with the respective corresponding images after background subtraction and 3x3 median filter was applied (b) (d). The yellow line indicates the cut through which the intensity profile in Figure 6.6 was measured. Pseudo colour and contrast adjustment applied to the images for display purposes only.

the signals are brought to the same baseline, allowing the intensities to be compared, as shown in Figure 6.6(c) and (d). Pixel noise is evident and is identified as sharp spikes in the intensity plots. The smoothing effect of applying a 3×3 pixel median filter to the image is shown in Figure 6.6(e) and (f).

To analyse the changes in membrane fluidity, the signal intensities of the GUVs after image processing were measured for each channel, and the GP values were calculated. An ImageJ plugin was written by Nicholas Barnes (152) to measure the signal intensities around the membrane ring. The plugin enables the average intensity as a function of angle around the membrane to be measured, averaging between the inner and outer membrane dimensions.

Firstly, the correction factor, S, to correct for the difference in sensitivity between the two detection channels was calculated. GUVs were imaged using a 488/20 band pass filter in both the forwards and backwards channel, and the fluorescence intensities of 21 sets of images were extracted using the ImageJ plugin. The ratio between the signal intensities from the forward and backwards channels was calculated using equation 6.2, and found to be 1.1 ± 0.2.

Using the corrected fluorescence intensities, the average GP values were calculated as a function of angle around the membrane ring using equation 6.1. For example, Figure 6.7 shows the fluorescence intensities, and calculated GP values corresponding to the DPPC/POPG GUVs displayed in Figure 6.5, as a function of arc length around the membrane ring. A boxcar average was applied to smooth out pixel noise so that the remaining fluctuations in GP indicate

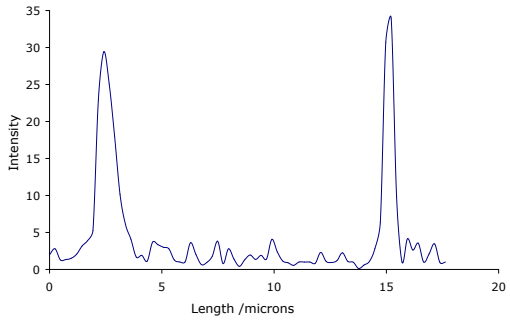

(a) Intensity profile for GUVs imaged using 488/30 nm bandpass filter before image processing.

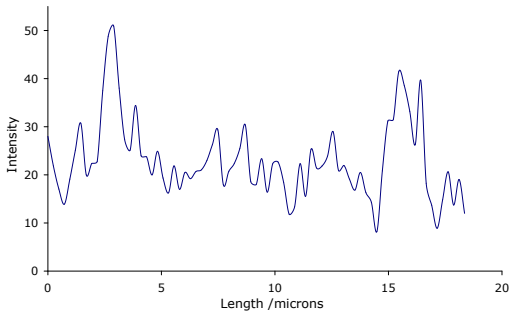

(b) Intensity profile for GUVs imaged using 436/30 nm bandpass filter before image processing.

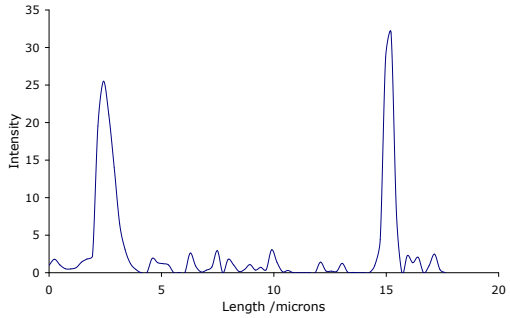

(c) Intensity profile for GUVs imaged using 488/30 nm bandpass filter after background subtraction.

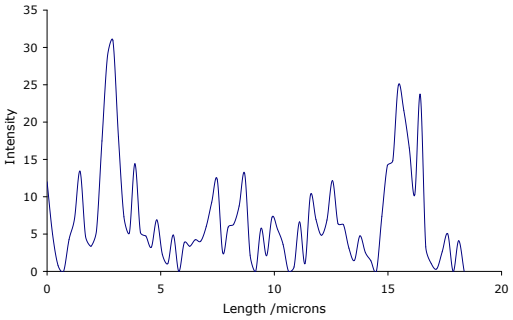

(d) Intensity profile for GUVs imaged using 436/20 nm bandpass filter after background subtraction.

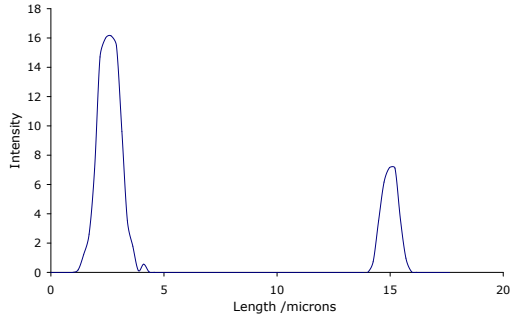

(e) Intensity profile for GUVs imaged using 488/30 nm bandpass filter after background subtraction and 3x3 median filter was applied.

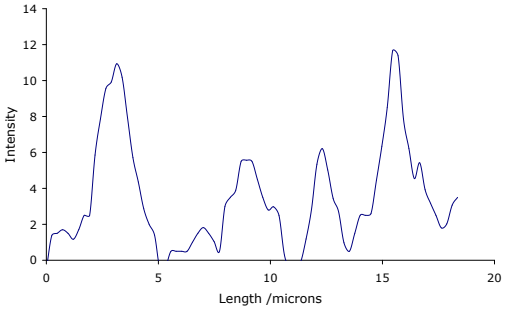

(f) Intensity profile for GUVs imaged using 436/20 nm bandpass filter after background subtraction and 3x3 median filter was applied.

Figure 6.6: Intensity profile plots measured for the GUVs shown in Figure 6.5.

differences in lipid fluidity around the membrane.

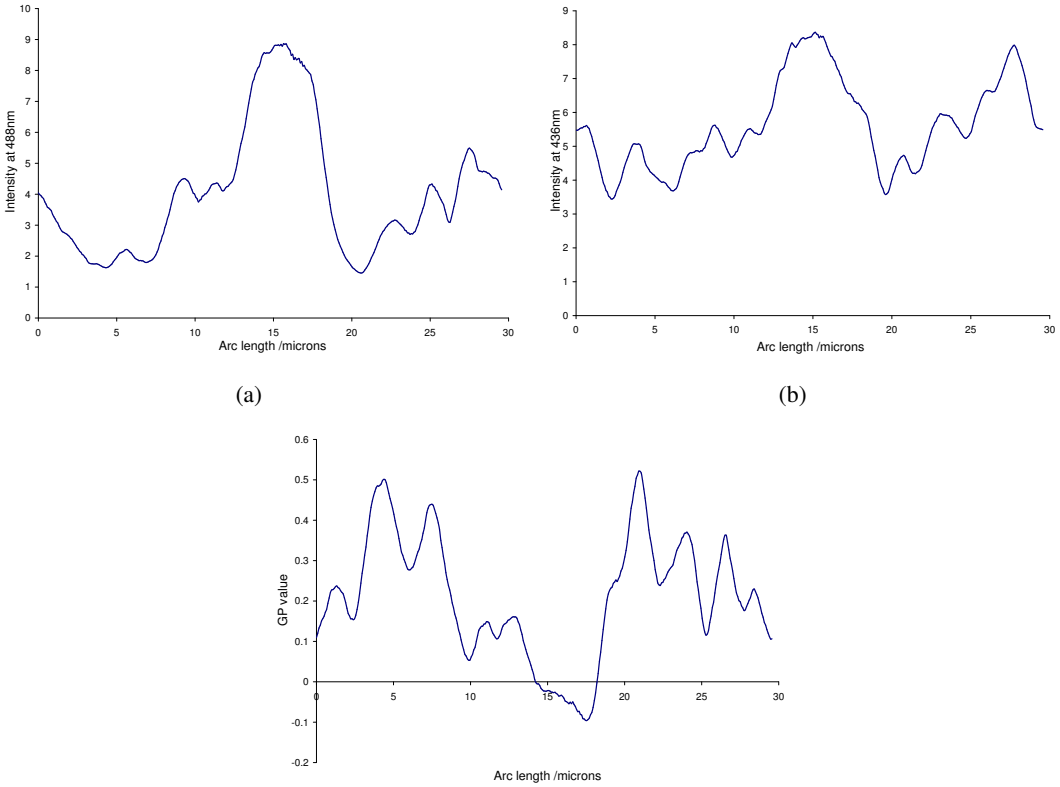

Figure 6.7: Graphs showing the fluorescence intensity as a function of length of arc around the membrane for the DPPC/POPG GUV images taken using the 488/20 nm band pass filter (a) and the 436/30 nm band pass filter (b). The corresponding GP values were calculated using the intensity measurements (c).

6.5.2 Single lipid GUV

To assess the GP of mixed DPPC/POPG GUVs and the effects of adding antimicrobial peptide, DPPC GUVs and POPG GUVs incorporating Laurdan dye were first imaged and analysed at various temperatures to obtain GP values for each type of phospholipid. An image of a group of DPPC GUVs at 25 °C, using a 488/20 nm band pass filter, is shown in Figure 6.8. Typically, isolated or distinctly separated GUVs were selected for image analysis. Temperature is a well known method for controlling the fluidity of lipids (153) and so provides a reliable method for acquiring GP values from different lipid phases. POPG GUVs were a lot more fragile than DPPC GUVs, readily rupturing and deforming during laser scanning, and at higher temperatures, the GUVs were a lot more susceptible to laser induced fragmentation. As a

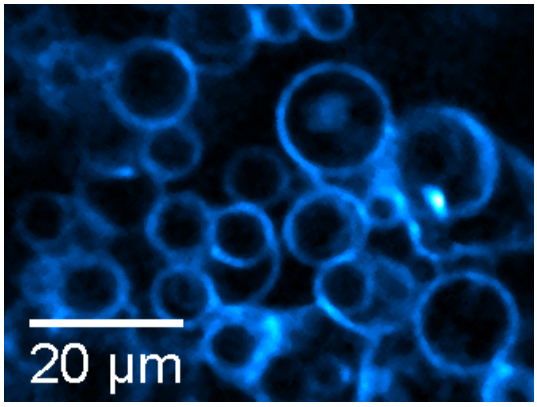

Figure 6.8: Image of a group of DPPC GUVs at 25 °C using a 488/20 nm band pass filter. Typically, isolated or distinctly separated GUVs were selected for image analysis.

consequence, only POPG GUVs at 25 °C survived the laser scanning in sufficient numbers that a statistically significant sample size could be imaged ($N = 26$).

Using the ImageJ plugin (152), the average intensities as a function of arc length around the annulus of the GUV were measured, and the GP values were calculated using equation 6.1. Examples of GP as a function of arc length are shown in Figure 6.9, where the orange and green bands on the graphs identify liquid crystalline and gel phases respectively, based on literature values (142). It is evident that the GP values reflect the lipid phases, with the plot of GP as a function of arc length for the DPPC GUV at 25 °C clearly shown to lie within the band identifying the gel phase (shown in Figure 6.9(a)), and the GP graph for the POPG GUV at 25 °C clearly shown to lie within the band identifying the liquid crystalline phase (shown in Figure 6.9(e)). As temperature increased, the GP values decreased, and the GP plot can be seen to lie within the liquid crystalline band for the DPPC GUV measured at 55 °C. Noticeably, at 45 °C the GP values fluctuate between the gel and liquid crystalline bands, showing coexisting gel and liquid crystalline phases, which is characteristic of the transition phase region.

The trend between GP and temperature/lipid phase is illustrated in Figure 6.10, which shows a graph of average GP and standard deviation, with the average GP calculated for each GUV and then averaged over the sample (N between 26 and 38) for DPPC GUVs at 25 °C, 35 °C, 45 °C and 55 °C, and POPG GUVs at 25 °C. The average GP are distinctly different for the GUVs in gel phase (DPPC GUVs measured at 25 °C and 35 °C) and the

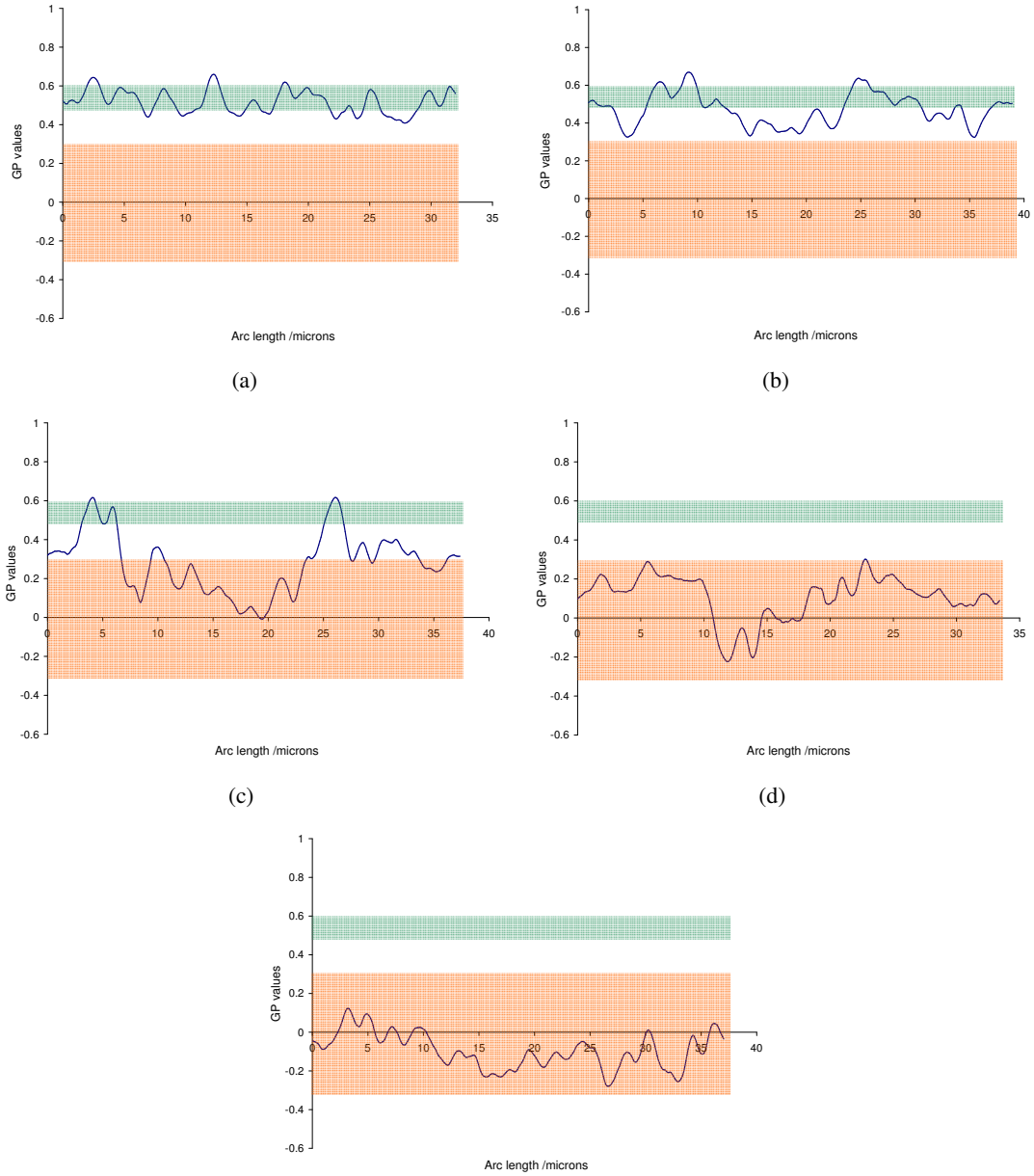

Figure 6.9: Plots of GP as a function of arc length of the annulus of the DPPC GUV at 25 °C (a), 35 °C (b), 45 °C (c), 55 °C (d), and POPG GUV at 25 °C (e). The orange band identifies the liquid crystalline phase and the green band identifies the gel phase, as determined from literature (142)

GUVs in liquid crystalline phase (DPPC GUVs measured at 55 °C and POPG GUVs at 25 °C). These results are in agreement with the GP values identified in the literature (142), where the GP values are between 0.5 and 0.6 for lipids in the gel phase, and between -0.3 and 0.3

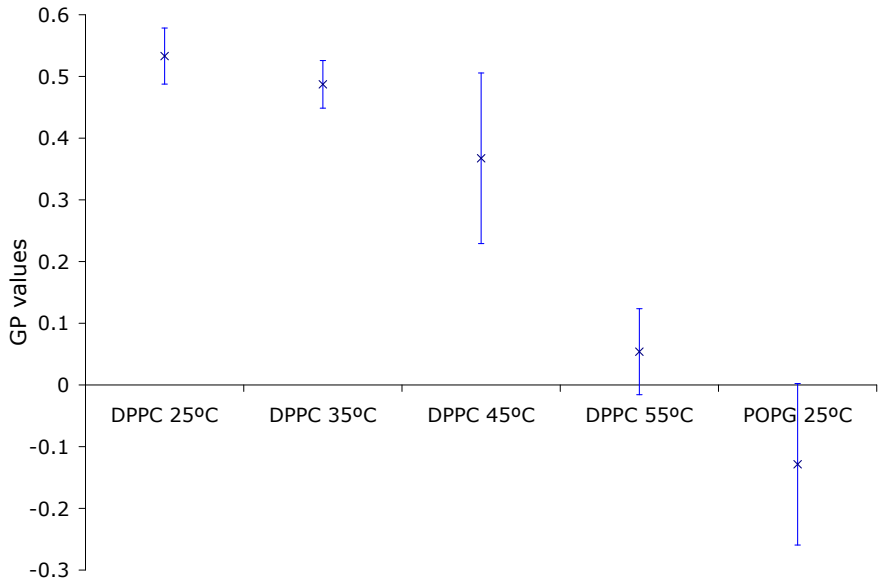

Figure 6.10: Plot of the average GP values of each DPPC and POPG GUVs, averaged over the sample with N between 26 and 38, at various temperatures. DPPC GUVs at 25 °C and 35 °C are in gel phase, with average GP values of 0.53(5) and 0.49(4) respectively. At 45 °C, DPPC GUVs are in the transition region, with an average GP value of 0.37(14) and at 55 °C, DPPC GUVs are in liquid crystalline phase with an average GP value of 0.05(7). POPG GUVs at 25 °C are in liquid crystalline phase with an average GP value of -0.13(13). Error bars show the standard deviation.

for the liquid crystalline phase. Again, the phase transition region is evident, as the standard deviation for GUVs measured at 45 °C indicates a wide distribution, which spans the expected GP values for gel and crystalline phases, suggesting coexistence of gel and liquid crystalline phase domains (153). Considering the liquid crystalline GP band, it is noticeable that the average GP and standard deviation for DPPC GUVs at 55 °C covers the upper region of the band, compared to the average GP and standard deviation of POPG GUVs which distinctively covers the lower region of the band. This indicates that liquid crystalline DPPC is less fluid than liquid crystalline POPG, which emphasises the influence of different lipid tail structures on lipid fluidity.

It is clear that the GP value gives a way to identify the phase of GUVs, since the change in the membrane fluidity can be associated with a change in the phase. The gel phase has been shown to exhibit GP values between 0.5 and 0.6, and the liquid crystalline phase GP

values between -0.3 and 0.3. These GP bands were used to assess the phase domains of mixed DPPC/POPG GUVs.

6.5.3 DPPC/POPG mixed GUVs

GUVs composed of a 3:1 mixture of DPPC:POPG were imaged at temperatures of 55 °C, 45 °C, 35 °C and 25 °C, and the GP values were calculated as described earlier, in order to track any lipid phase changes as the temperature was altered. Subsequently, the GUVs were incubated with 10 μM AMP2 for one hour at room temperature before imaging, and the GP values were calculated and compared with the GP results of GUVs at the various temperatures. Examples of DPPC/POPG GUVs at the various conditions are shown in Figure 6.11. Interestingly, the GUVs shown in Figure 6.11(e) appear to be deformed in comparison to the spherical GUVs shown in Figure 6.11(a)-(d), which indicates that AMP2 interaction with the GUVs is visibly noticeable.

Examples of typical plots of GP values as a function of distance around the equatorial section for GUVs at 25 °C, 35 °C, 45 °C, 55 °C and when incubated with AMP2 are shown in Figure 6.12, where the orange band covers the liquid crystalline phase and the green band covers the gel phase. Figure 6.12(a) shows the GP values for the GUV measured at 25 °C, where the GP fluctuate between the gel and liquid crystalline phases. Referring to the GP values shown in Figure 6.9, which were obtained by assessing DPPC GUVs and POPG GUVs, it was found that at 25 °C, the GP values of DPPC lipids lay within the boundaries indicating gel phase and the GP values of POPG lipids lay within the boundaries indicating liquid crystalline phase. Since a 3:1 composition of DPPC and POPG was used to form the mixed GUVs, at 25 °C, it is expected that if lipids separate into domains, around 25% of the membrane would be in the liquid crystalline phase, which is seen to be the case in the example shown in Figure 6.12(a) where approximately 25% of the GUV circumference shows a GP value < 0.3. This indicates that the regions of gel and liquid crystalline phase domains can be identified from the GP plots. Referring to the rest of the GP plots, it is evident that as temperature increases, the average GP values decreases, with the GP values measured at 55 °C lying wholly

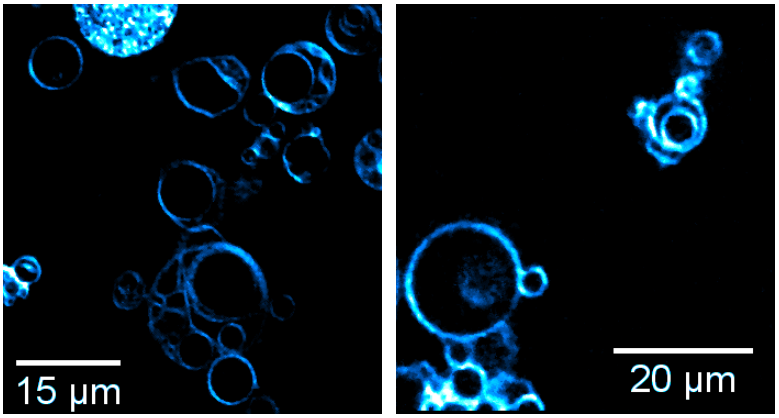

(a)

(b)

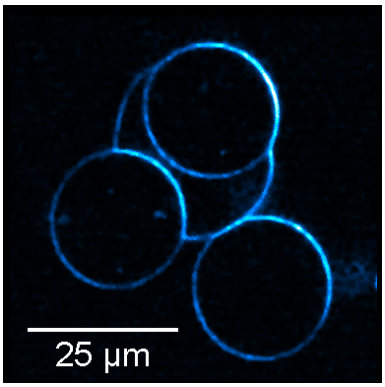

(c)

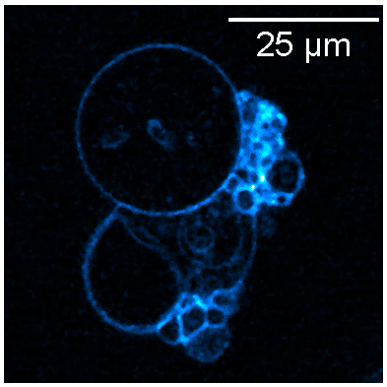

(d)

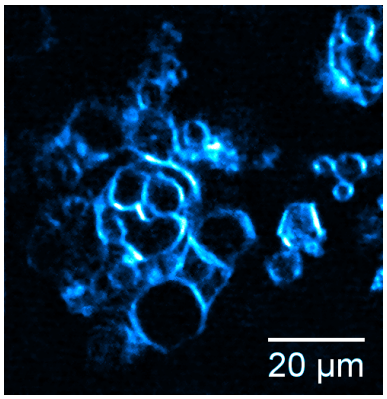

(e)

Figure 6.11: Images of DPPC/POPG GUV using 488/30 nm bandpass filter at 25 °C (a), 35 °C (b), 45 °C (c), 55 °C (d) and when incubated with 10 µM AMP2 (e). Pseudo colour and contrast adjustment were applied to the images for display purposes only.

within the liquid crystalline band, as shown in Figure 6.12(d). This trend between GP and temperature is illustrated in Figure 6.13, which shows the average GP values from a set of

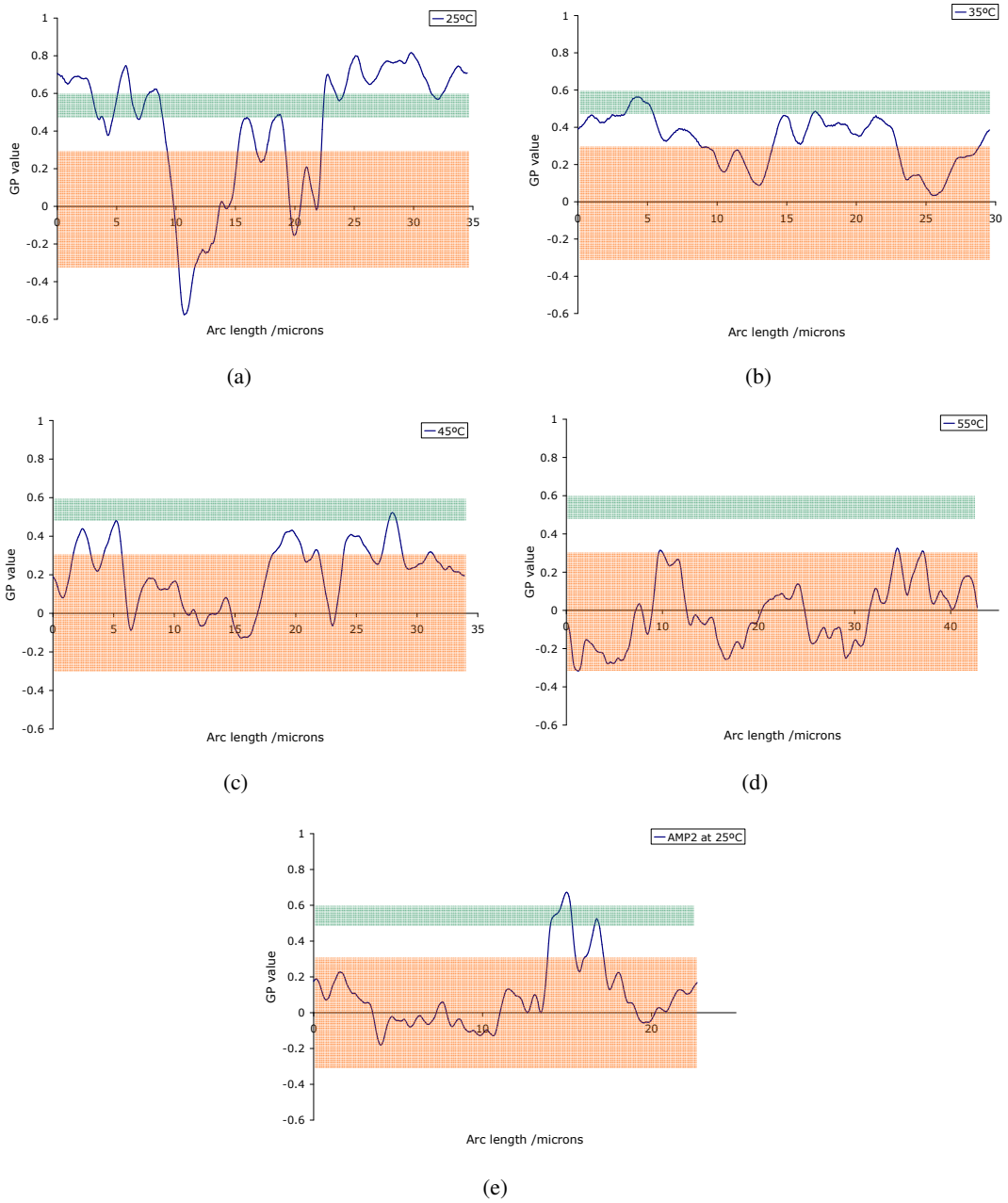

Figure 6.12: Plots of GP values as a function of arc length of the circumference of the imaged DPPC/POPG GUV. These plots show the variation of GP value, hence lipid fluidity around the membrane at 25 °C (a), 35 °C (b), 45 °C (c), 55 °C (d), and interacted with AMP2 at 25 °C (e). The orange band depict the liquid crystalline phase and the green band depict the gel phase.

GUVs ($N = 20$) measured at each temperature and when incubated with AMP2. By comparing with Figure 6.10, the average GP clearly spans a smaller range, with a maximum average GP of 0.3(9) measured for DPPC/POPG GUVs at 25 °C compared to 0.53(5) for DPPC GUVs at

25 °C, and a minimum average GP of -0.02(11) for DPPC/POPG GUVS at 55 °C compared to -0.13(13) for POPG GUVs at 25 °C. However, the associated standard deviations are larger for the mixed DPPC/POPG GUVs, which reflects the presence of domains of different phases.

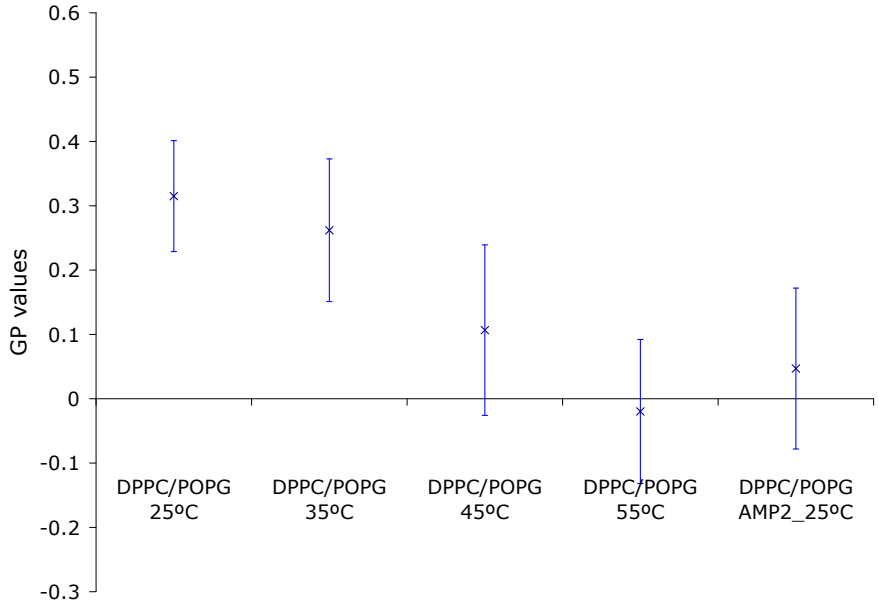

Figure 6.13: Plot of the average GP values of DPPC/POPG GUVs at various temperatures at 25 °C, 35 °C, 45 °C, 55 °C and incubated with AMP2 at 25 °C, with average GP values of 0.32(9), 0.26(11), 0.11(13), -0.02(11) and 0.05(13) respectively. Error bars show the standard deviation, with $N = 20$.

As mentioned above, phase domains can be identified from the large fluctuations in the GP values, resulting in the well defined peaks and troughs that are evident in Figure 6.12(a). The size of the GP fluctuations decrease as temperature increases, which is indicative of the lipid phase change from gel to liquid crystalline. Interestingly, referring to the GP plot of DPPC/POPG GUV at 55 °C, defined peaks and troughs are noticeable, which are larger than the fluctuations in the GP plot of DPPC GUV at 55 °C, shown in Figure 6.9(d). This suggests that even though both GUVs are in the liquid crystalline phase, the mixed DPPC/POPG GUV retains defined lipid domains. Lipid fluidity can be determined by the degree of tail orientation disorder. In this way, phase domains may be formed within the bilayer based on the arrangement of groups of lipids with similar degrees of freedom of the lipid tails.

On the other hand, the lipid head group also influences the arrangement of the lipids within the bilayer, where DPPC and POPG differ regarding the head group charge (zwitterionic and anionic respectively), therefore the formation of lipid domains is likely to be the combination of both factors.

Figure 6.12(e) shows the GP plot for DPPC/POPG GUV incubated with 10 μM AMP2, at 25 °C. It is noticeable that in comparison with the GP plot for the untreated DPPC/POPG GUV, a significantly larger proportion of the membrane is in the liquid crystalline phase. This suggests that the antimicrobial peptide has changed the membrane fluidity, increasing the proportion of liquid crystalline domains. It should be emphasized that the GP profiles shown were extracted from different GUVs, so some caution should be exercised when making direct comparisons between the plots in Figure 6.9; of greater significance are the changes in the probability distributions obtained by analysing the population of GUVs.

In order to further assess the change in phase domains, GP plots were produced for a number of GUVs ($N = 20$) at the various conditions. To compare between the different conditions, the fluctuations in the GP values (peaks and troughs) were analysed, as changes in the minima/maxima GP seem to be indicative of the local phase change. To quantify the change in GP fluctuations, multiple Gaussian peak fits were applied to each plot using the multipeak fit function in the IGOR Pro 6 software package, with the smoothing and noise value set to ensure that small fluctuations were ignored. The condition for determining whether the fluctuations were significant was based on the GP plots of DPPC GUVs and POPG GUVs at 25 °C (in Figure 6.9), since the plots correspond to homogeneous gel and liquid crystalline phases respectively. As such, fluctuations of a similar magnitude displayed in Figure 6.9(a) and (e) were treated as noise and excluded from the peak fitting. An example of the peak fitting is shown in Figure 6.14 where Figure 6.14(a) shows the overall fit after applying the multipeak analysis, and Figure 6.14(b) shows an illustration of the individual Gaussian peaks (green) and troughs (blue). The maxima and minima GP values were extracted from the Gaussian peaks and troughs, which enables the difference in fluidity between the phase domains to be quantified. Measuring the peak/trough widths of the Gaussian fits enables the phase domain lengths to

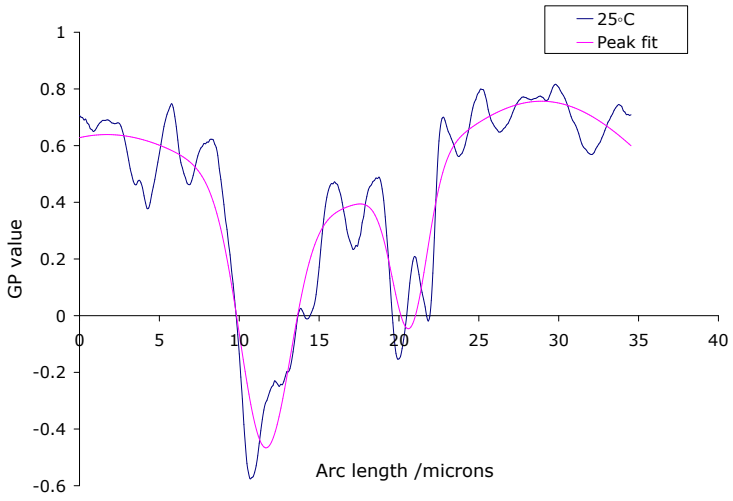

(a)

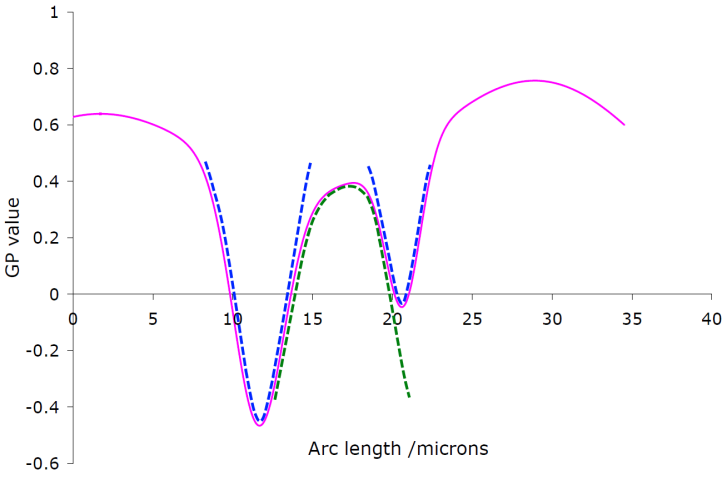

(b)

Figure 6.14: Example of the peak fitting applied to the GP plot for DPPC/POPG GUV measured at 25 °C. Multiple Gaussian peaks were fitted using the multipeak fit function in the IGOR Pro 6 software package, where a plot of the combination of Gaussian peaks (and troughs) are shown for illustration purposes (a). The individual Gaussian peaks (green) and troughs (blue) (b) are analysed, where the maxima and minima GP values, and the widths of the Gaussians are measured.

be quantified. To analyse the beginning and end regions of the GP plots (since GUVs are continuous), the beginning and end points were joined and replotted, and the multipeak fitting analysis is applied.

For each condition, the average minima/maxima GP values of the peaks/troughs were

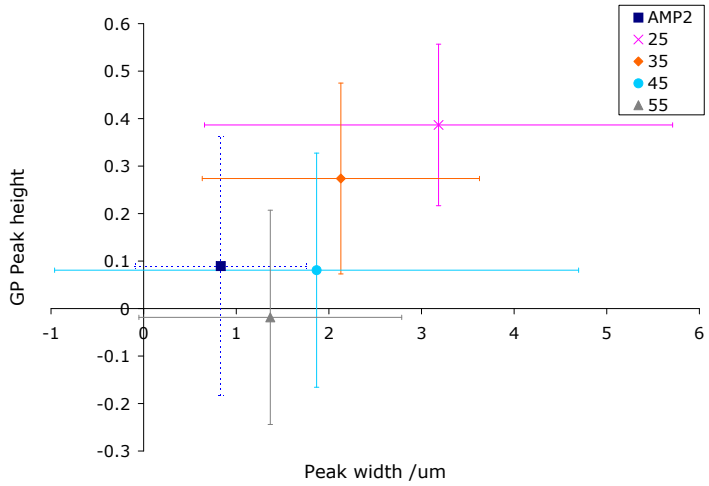

(a)

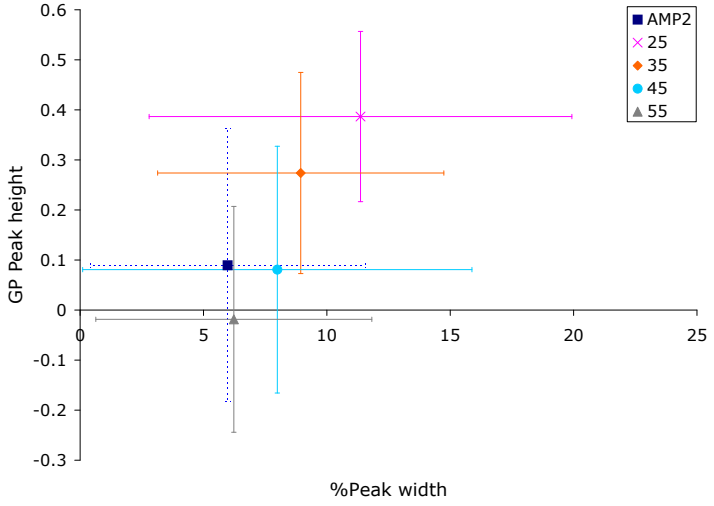

(b)

Figure 6.15: Plot of average peak maxima/minima GP values against average peak width (a) and average peak maxima/minima GP values against average peak width as a percentage of the length of the membrane circumference (b) for DPPC/POPG mixed GUVs at 25 °C, 35 °C, 45 °C and 55 °C, and interacted with AMP2 at 25 °C. Error bars show the standard deviation.

calculated and plotted against the average peak widths, as shown in Figure 6.15(a), which gives a measure of the average lipid phase and the size of the lipid domains of mixed DPPC/POPG GUVs for each condition.

As expected, the average minima/maxima GP value decreased as temperature increased,

which is consistent with the results presented earlier. Interestingly, the average maxima/minima GP value for GUVs incubated with AMP2 is 0.09, and is comparable to the average maxima/minima GP value for untreated GUVs at 45 °C. This suggests that GUVs incubated with AMP2 exhibit phase domains similar to membranes in the phase transition region.

Figure 6.15(b) shows the average maxima/minima GP values plotted against the average peak width as a percentage of the membrane circumference. Assessing the peak width as a percentage of the length of the membrane circumference accounts for the size variation in the GUVs imaged, as one consideration is whether the size of the domains are affected by the overall size of the GUV. It is evident from the graph that the relative length of the peak widths for each data set did not vary outside the uncertainties, showing that the size of the domains are unaffected by the size of the GUVs. The untreated sample of GUVs measured at 25 °C exhibit larger domains than the GUVs measured at higher temperatures and when incubated with AMP2, which indicates that a decrease in domain size is caused by both an increase in temperature as well as the interaction with AMP2. This is interesting because a decrease in domain size suggests an increase in the number of domains, since the lipid composition is unchanged, which means a greater number of domain boundaries in the GUV and so implies an increase in phase boundary defects, which may have the effect of weakening the membrane.

The plots showing the average maxima/minima GP values against peak widths are useful for identifying a basic trend regarding how the lipid domains change with temperature, and when AMP2 is added, since the GP plots indicate that DPPC/POPG GUVs may comprise both liquid crystalline and gel phase domains. A further assessment of the domain changes can be obtained by looking at the distribution of the maxima/minima GP values across a population of GUVs. Figure 6.16 shows the population distribution of maxima/minima GP values from the multipeak fitting analysis for a sample ($N = 20$) of DPPC/POPG GUVs at 25 °C, 35 °C, 45 °C and 55 °C, and incubated with AMP2 at 25 °C. Interestingly, referring to Figure 6.16(a), it is noticeable that a proportion of the population distribution lies at GP > 0.6, which indicates that at 25 °C, DPPC in mixed DPPC/POPG GUVs are less fluid than pure DPPC GUVs at 25 °C. This suggests that interaction between DPPC and POPG in the GUV, possibly due to

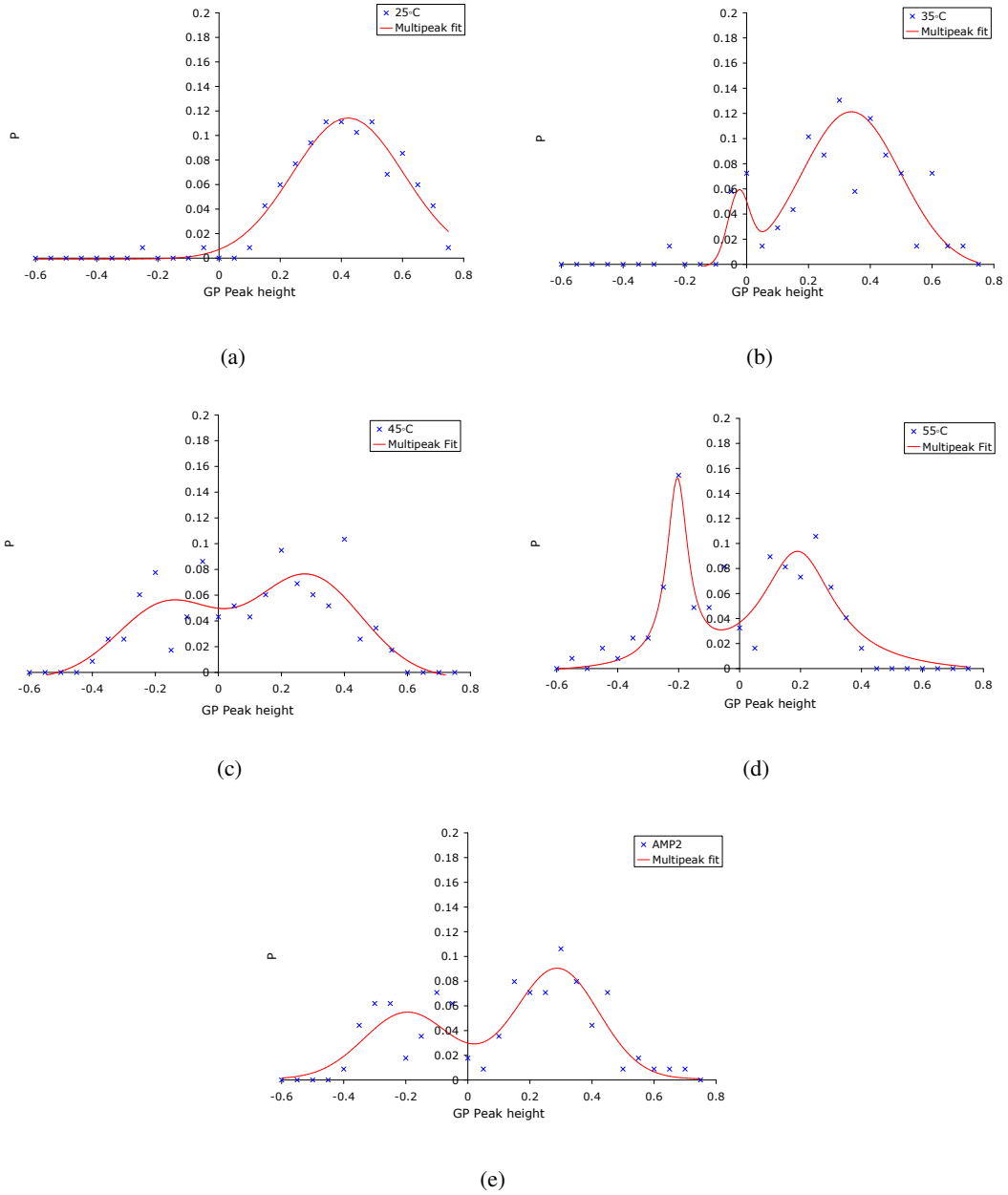

Figure 6.16: Histograms of the peak/trough maxima/minima GP values for DPPC/POPG mixed GUVs at 25 °C (a), 35 °C (b), 45 °C (c), 55 °C (d), and interacted with AMP2 at 25 °C (e). For each plot, a Gaussian multipeak fitting using IGOR Pro 6 was applied. $N = 20$

the different headgroup charges, may have an effect on the fluidity.

It is evident that the shape of the population distributions change as temperature is increased past the transition temperature of DPPC. The population distribution of DPPC/POPG GUVs

at 25 °C, shown in Figure 6.16(a), show that the majority of the GP peaks lie in the gel phase bands, with the peak of the distribution at a GP value of 0.48. It is not immediately obvious that there are distinct domains at 25 °C, which is partly due to the relative proportion of POPG in the mixture being approximately 25%, but also partly implies that the GP for the liquid crystalline POPG must be towards the upper end of the liquid crystalline GP band. As temperature increases, the population distribution evidently shifts towards the liquid crystalline region, with the peak of the population distribution shifting down to a GP value of 0.2 for the sample measured at 55 °C. For the mixed GUVs measured at 35 °C, a second peak in the population distribution emerges at at a GP value of approximately -0.2, and the peak becomes more prominent as temperature increases to 55 °C, which reflects the increase in the proportion of liquid crystalline phase domains.

The change in the proportion of GP peaks measured that were in the liquid crystalline phase is shown in Table 6.1 for each condition, where the percentage of peaks with GP < 0.3 and GP > 0.3 are displayed. A GP value of 0.3 can be associated with the liquid crystalline/gel phase boundary, with GP < 0.3 indicating liquid crystalline phase and GP > 0.3 indicating coexisting or gel phases, as stated in literature (153). Referring to Table 6.1, 30% of peaks measured at 25 °C are in the liquid crystalline phase, which increases to 94% at 55 °C. For GUVs measured at 35 °C, 55% of the peaks lie in the liquid crystalline band, which is higher than expected considering that the transition temperature for DPPC is 41 °C. Studies have found that a subtransition region of DPPC exists between 35 °C and 36 °C (153)(154) where the liquid crystalline domains are formed only when cooling through this temperature range, which may explain why an increase in the amount of lipids in liquid crystalline domains are detected.

GP	AMP2	25 °C	35 °C	45 °C	55 °C
< 0.3	75%	30%	55%	77%	94%
> 0.3	25%	70%	45%	23%	6%

Table 6.1: Table showing the percentage of peaks with GP < 0.3 and GP > 0.3 for the different GUV conditions.

Most interestingly, for the GUV sample incubated with AMP2 at 25 °C, 75% of the peaks are in the liquid crystalline phase, which is a significantly larger proportion of liquid crystalline domains than exhibited by the untreated sample at 25 °C. This proportion is similar to that for the proportion of peaks of the untreated GUV sample measured at 45 °C (77%), which suggests that the addition of AMP2 causes a significant change to the lipid domains similar to that for the GUVs in the phase transition temperature region.

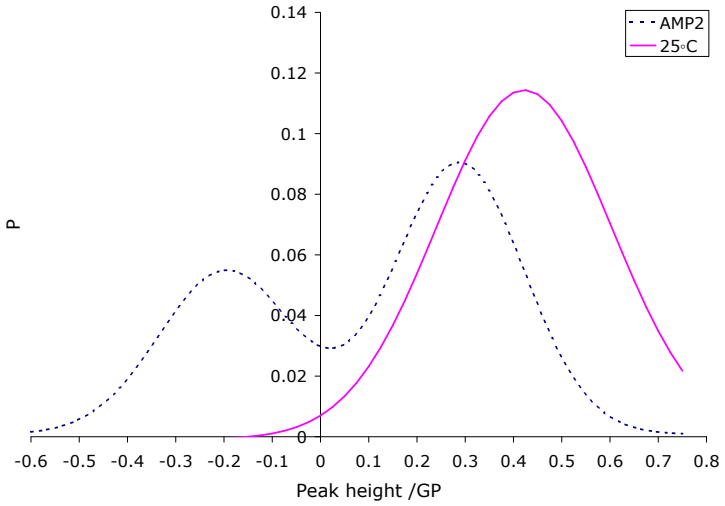

(a)

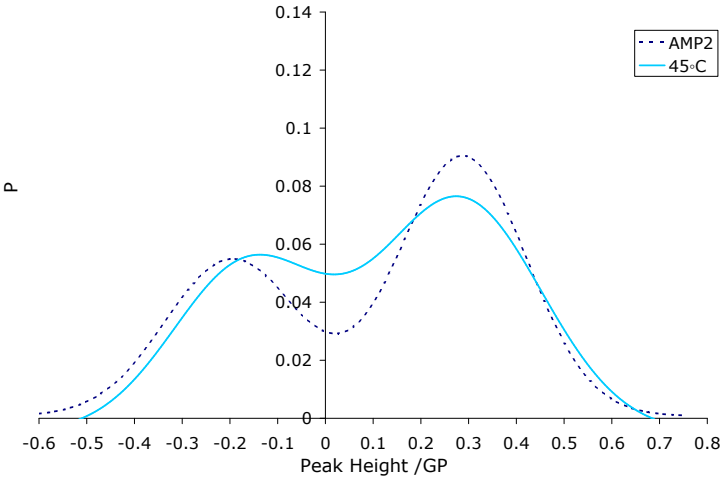

(b)

Figure 6.17: Histogram overlays of the peak maxima/minima GP values of DPPC/POPG mixed GUVs at 25 °C and interacted with AMP2 at 25 °C (a); 45 °C and interacted with AMP2 (b).

Referring to Figure 6.16, the shape of the population distribution for DPPC/POPG incubated with AMP2 at 25 °C clearly differs from that of the untreated sample at 25 °C, with the distribution showing a second, defined peak in the liquid crystalline GP band at a GP ≈ -0.2. This is evident in Figure 6.17(a), which shows an overlay of the population distribution of GP peak values for both the untreated DPPC/POPG GUV sample, and DPPC/POPG GUV sample incubated with AMP2, at 25 °C, and emphasises the change in the relative populations of the different phase domains as a result of antimicrobial peptide interaction. As mentioned earlier, the interaction of AMP2 with DPPC/POPG GUVs appears to result in lipid domains that are similar to DPPC/POPG GUVs in the phase transition region. An overlay of the population distributions of DPPC/POPG GUV incubated with AMP2 at 25 °C, and DPPC/POPG GUVs at 45 °C is shown in Figure 6.17(b), which highlights the similarities in the shape of the population distribution of GP peak values. This overlay emphasises that the distribution of gel and liquid crystalline phase domains are similar, which indicates that the effect of AMP2 on DPPC/POPG GUVs effectively causes an increase in the population of liquid crystalline domains.

6.6 Conclusion

DPPC/POPG GUVs were formed using electroformation to provide a model bacterial membrane, and by incorporating Laurdan fluorescent dye into the GUVs, the lipid phases were visualised based on the GP values. It was found that by assessing pure DPPC GUVs at temperatures ranging from 25 °C to 55 °C, and pure POPG GUVs at 25 °C, the GP values were ideal for identifying the lipid phases with spatial resolution, in which the gel phase was characterized as exhibiting GP values between 0.5 to 0.6, and the liquid crystalline phase was characterized as exhibiting GP values between -0.3 to 0.3. When comparing the average GP and standard deviation between DPPC GUVs and POPG GUVs in the liquid crystalline phase, it was clear that the GP values for DPPC lay towards the upper region of the liquid crystalline GP band (0 - 0.1), in comparison to the GP values for POPG which lay in the lower region of the liquid crystalline band (-0.3 - 0). This result indicated that differences in fluidity within the same lipid phase could be detected by the GP. In addition, coexistence of both gel and

liquid crystalline phases were detectable as the GP values for DPPC GUVs measured at 45 °C spanned across the gel and liquid crystalline GP band.

It was found that the GP values of mixed DPPC/POPG GUVs also lay within the characterized GP bands corresponding to gel and liquid crystalline phases, therefore the lipid phases could be identified using the same GP bands determined using pure DPPC and pure POPG GUVs. GP plots of mixed DPPC/POPG GUVs exhibited large fluctuations in GP, which was most obvious in the DPPC/POPG GUV samples measured at 25 °C. In this sample, 30% of the GP values lay in the liquid crystalline phase band, which is slightly higher than what might be expected given that only 25% of the lipid composition is POPG (POPG is expected to be in the liquid crystalline phase at 25 °C). A possible explanation is that DPPC molecules at the edges of the DPPC domains find themselves in a more fluid environment than those in the centre of the domain, thus increasing the proportion of lipids in the liquid crystalline phase. It was found that the average GP value and the fluctuation in the GP plots decreases as temperature increases past the phase transition temperature of DPPC (41 °C), where at 55 °C, the values lay within the liquid crystalline GP band, indicative of the increase in the proportion of liquid crystalline phase domains (and decrease in the proportion of gel phase domains) confirming that the change in the phase domains could be detected using this method. Additionally, defined peaks and troughs were identifiable in the GP plots of DPPC/POPG GUVs at 55 °C, suggesting that even though the GP values indicated that the GUV comprised only liquid crystalline phases, defined lipid domains were still present, which was most likely the result of DPPC and POPG not mixing due to interaction between the different headgroups.

Analysing the probability distributions of minima/maxima GP values of the peaks and troughs of the GP plots ascertained that by measuring the large fluctuations in GP, gel and liquid crystalline phase domains could be identified across the population of GUVs ($N = 20$ for each condition). The probability distributions of minima/maxima GP showed defined peaks, in which a peak was evident at a GP of 0.48 for GUVs measured at 25 °C, confirming the presence of gel phase domains, that then decreased to a GP of 0.2 as temperature increased to 55 °C. The emergence of a second peak in the probability distributions at a GP of -0.2, at 35 °C,

confirmed the presence of liquid crystalline phase domains, which became more prominent as temperature increased to 55 °C indicating the increase in the proportion of liquid crystalline phase domains. A significant change to the lipid phase domains were seen when DPPC/POPG GUVs were incubated with AMP2. It was found that interaction of AMP2 with DPPC/POPG GUVs at 25 °C resulted in a distribution of lipid domains similar to those exhibited by untreated samples in the phase transition region (45 °C). The proportion of liquid crystalline domains increased significantly from 30% for untreated GUVs at 25 °C, to 75% for GUVs incubated with AMP2. This indicates that the antimicrobial peptide induces a significant increase in the proportion of liquid crystalline phase domains formed in the membrane. In addition, it was found that the size of the phase domains were smaller for DPPC/POPG GUVs incubated with AMP2 than when untreated, at 25 °C. This is an interesting result because a decrease in domain size suggests an increase in the number of domains, since the lipid composition remains unchanged, which means a greater number of domain boundaries in the GUV and so implies an increase in phase boundary defects, which may have the effect of weakening the membrane.

Conclusion and further works

7

Conclusions

7.1 Conclusions

This chapter will give an overview of the results and findings from the studies presented in this thesis, and highlight the significance of these contributions. In addition, avenues for further studies will be discussed.

7.1.1 Part 1

The first study investigated the interaction between mCMV and lipid droplets in fibroblast cells, as although it has been acknowledged that there are links between cytomegalovirus and host-cell lipid droplets, the specific interactions and physical effects of the infection on the droplets remained unknown. In Chapter 4, it was shown that using a multimodel optical microscopy set-up, comprising CARS and TPF, the lipid droplets in fibroblast cells can be easily identified with CARS microscopy, and by using a modified version of the Smith strain of mCMV, which caused the host cell to express GFP as it replicated the viral protein, the progression of infection was quantified using TPF microscopy to detect and measure the fluorescence intensity in the cell. The addition of a live cell chamber made it possible to maintain live cells for 2 to 3 days on the microscope stage, which was essential for enabling the changes to the lipid droplet configurations to be observed over the entire course of infection. This live cell imaging

platform facilitated the imaging and measurement of lipid droplet configurations as a function of the stage of mCMV infection (early, intermediate or late stage of infection). It was found that the number of lipid droplets observed decreased significantly from the early stage of infection through to the late stage of infection, and that the cross-sectional areas increased as infection progressed, where lipid droplets exhibiting cross-sectional areas greater than $8\ \mu m^2$ were only detected in the intermediate and late stages of infection.

In addition, lipid droplet clustering was observed in the CARS images of live cells during the intermediate stage of infection. Interestingly, lipid droplet clustering was often observed to be positioned around the cell periphery, with a tendency of finding lipid droplet clusters at the cell boundaries adjacent to neighbouring cells. This observation suggests that the viral infection influences the movement of lipid droplets, with the possibility that the droplets are specifically directed towards the cell periphery and towards neighbouring cells. It is possible that the virus may use the lipid droplets as a means to transport the viral progeny out of the host cell, where it also specifically directs the progeny towards neighbouring cells. However, this speculation requires further work to determine the specific function of lipid droplets with regards to mCMV. Rather, the lipid droplet mobility was analysed to determine whether mCMV infection affected the dynamics of intracellular lipid droplets. A drawback of using CARS/TPF microscopy to study live cells is the photodamage exerted on the fibroblast cells due to the laser scanning, which perturbed the cells to an extent that meant a single cell could not be imaged over the course of infection. In addition, with the relatively long image acquisition times of laser scanning, lipid droplet movements could not be followed. To address these issues, DIC microscopy was used to track lipid droplet motion across the course of infection as the technique is capable of continuous imaging, and also exerts low stress on the cells making imaging over long time scales feasible.

It was found that the lipid droplet trajectories are composed of two modes of motion, which were characterised and separated into diffusive and directed motion trajectory segments. From the analysis of the diffusive trajectory segments of a population of cells, the diffusion coefficients, D, were found to be significantly higher in the infected cells than in the healthy

cells, with D being $20(19) \times 10^{-4}$ μm^2 s^{-1} and $8(9) \times 10^{-4}$ μm^2 s^{-1} respectively. The changes in diffusion coefficient were mirrored by the results found in the single cell study, confirming that the effects of mCMV infection on the diffusive behaviour of lipid droplets is detectable in both a cell population as well as within a single cell. It can be concluded that the diffusive motion of the lipid droplets increases significantly as a result of mCMV infection.

Since the diffusion coefficient is dependent on both the effective viscosity, η of the media and the radius, r, of the lipid droplet, an important question was to assess whether the lipid droplet size had a direct influence on the diffusion coefficient. However, as the lipid droplets are close to the resolution limit of the microscope system, caution must be exercised when making a definite conclusion about the effects of lipid droplet size. The probability distributions of the lipid droplet radii was found to be Gaussian in shape, with no evidence of a drastic cut-off towards the left of the distribution that would have indicated problematic resolution-limit effects. This suggested that the majority of the lipid droplet population exhibited sizes that were greater than the resolution limit. The graphs showing the relationship between D and droplet size does not exhibit a simple $\frac{1}{r}$ trend, indicating that D is not solely dependant on the radius, which implies that the effective microviscosities are not constant. Using the measured lipid droplet radii and the diffusion coefficients, the average values of η were calculated to be 2.8 Pas for healthy cells and 0.9 Pas for infected cells, showing that the average effective viscosity in the infected cells is approximately a third of the average effective viscosity in the healthy cells. This result indicates that the effective intracellular viscosities can be probed by analysing the diffusive trajectory segments of lipid droplet motion, which is interesting because typically, cellular microviscosity is measured by incorporating fluorescent molecular rotary motors into the cell, since the fluorescence emission spectra alters with the change in viscosity and can measure a dynamically changing environment (see references (117) (122) and (119) for details).

Moreover, this finding suggests that mCMV infection causes changes to the intracellular properties, which results in a significant decrease in the effective viscosity of the cell. The intracellular viscosity is dependant on the viscosity of the cytosol, the number of

macromolecules in the local region, and the cytoskeleton. Since the viscosity of the cytosol is known to be similar to water, it can be speculated that a significant reduction in the effective viscosities is related to a change in the ordering and structure within the cell, such as a reduction in local crowding experienced by the lipid droplet.

By comparing the proportion of trajectory segments that were diffusive versus directed, it was found that lipid droplets in the infected cells exhibited a greater proportion of directed transport modes than diffusive transport modes, compared to the healthy cells. In addition, it was clear that the maximum speeds exhibited by the lipid droplets were significantly greater for infected cells, with maximum speeds of 2.9 μm s^{-1} measured compared to 1.7 μm s^{-1} measured in the healthy cells, where approximately 5% of the population of the trajectories in the infected cells exhibited speeds $>$ 1.7 μm s^{-1}. Most interestingly, the directed motion of lipid droplets appears to be associated with molecular motor activity, as the average speed measured of 0.8 μm s^{-1} corresponds to the typical speed of kinesin motors when attached to cargo molecules *in vivo*. In addition, secondary and tertiary peaks at approximately 1.3 μm s^{-1} and 1.7 μm s^{-1} are evident in the trajectory speed distributions, suggesting evidence for coordinated molecular motor activity, where the peaks indicate that multiple motors act together to transport a single lipid droplet. These peaks are significantly more prominent in the infected cells, suggesting that mCMV infection affects the lipid droplet dynamics by increasing the rate of directed transport, and increases the proportion of motion that involves a multiple of molecular motors.

It was observed from the CARS images that the lipid droplets tended to cluster in infected cells. By analysing the radial distribution function of the arrangement of lipid droplets in DIC images of healthy and infected cells, this lipid droplet clustering was quantified. The infected cells were found to exhibit greater lipid droplet density at radial distances $<$ 5 μm compared with the healthy cells, showing that infected cells exhibited a greater degree of lipid clustering. It was also observed that lipid droplets in the infected cells tended to arrange in a circular (ring) formation. In addition, it was possible to see individual lipid droplets being actively transported towards lipid droplet clusters. These qualitative observations suggest that the mCMV infection

induces a form of order to the arrangement of the lipid droplets, where droplets are prone to arrange in a circular pattern, and are actively directed to form clusters.

In summary, it can be concluded that the lipid droplet dynamics are substantially affected by mCMV infection. Tracking the motion of the droplets has shown that the diffusion coefficient increases significantly, that the proportion of trajectories exhibiting directed transport increases, with greater movement speeds, and that the droplets exhibit a greater degree of clustering as a result of infection. The results of this study also indicate that intracellular properties, such as the effective microviscosities and the molecular motor activity can be probed by tracking and analysing both the diffusive and directed motion of intracellular lipid droplets. These findings suggest that the effect of mCMV infection influences the arrangement of lipid droplets, where the droplets appear to be positioned in a much more ordered configuration. In addition, the results suggest that the viral infection causes an increase in the activity of the transport motors, and also effectively decreases the intracellular viscosity.

This work is the first of its kind, where lipid droplet motion (diffusive and directed modes of motion) is measured in order to estimate intracellular viscosity and molecular motor activity as a function of the viral infection cycle. It can be speculated that the effects that were observed and quantified are the result of the virus hijacking the cell. It is possible that the virus influences a restructuring of the cytoskeleton, and increases the rate of molecular motor activity in order to optimise the delivery of viral progeny out of the host cell. Further research is required to investigate this speculation.

7.1.2 Part 2

The second study investigated whether antimicrobial peptides induce drastic changes in membrane fluidity. DPPC/POPG GUVs were formed using electroformation to produce a simple model for the *E. Coli* membrane, and by incorporating Laurdan fluorescent dye into the GUVs, the lipid phases were visualised based on the GP values. By assessing pure DPPC GUVs at temperatures ranging from 25 °C to 55 °C, and pure POPG GUVs at 25 °C, it was found that spatially resolved GP values could be used to identify the lipid phases, with the gel

phase being characterized by GP values between 0.5 to 0.6, and the liquid crystalline phase being characterized by GP values between -0.3 to 0.3. When comparing the average GP and standard deviation of DPPC GUVs and POPG GUVs in the liquid crystalline phase, it is clear that the GP values for DPPC lie towards the upper region of the liquid crystalline GP band (0 - 0.1), in comparison to the GP values for POPG which lie in the lower region of the liquid crystalline band (-0.3 - 0). This result indicates that differences in fluidity within the same lipid phase can be identified using GP. In addition, coexistence of both gel and liquid crystalline phases is detectable, as the GP values for DPPC GUVs measured at 45 °C span between the gel and liquid crystalline GP bands.

It was found that the GP values of mixed DPPC/POPG GUVs also lie within the GP bands corresponding to the gel and liquid crystalline phases that were determined using pure DPPC and pure POPG GUVs. GP plots of mixed DPPC/POPG GUVs at 25 °C exhibit large fluctuations in GP, which decrease in magnitude as the temperature increases to 55 °C. In addition the average GP values decrease as the temperature increases past the phase transition temperature of DPPC (41 °C), such that at 55 °C, all the GP values lie within the liquid crystalline GP band. The decrease in average GP value and decrease in the magnitude of the GP fluctuations as temperature increases past the phase transition temperature is indicative of the increase in the proportion of liquid crystalline phase domains (and decrease in the proportion of gel phase domains) confirming that the change in the phase domains could be detected by determining the GP value. Additionally, defined peaks and troughs can be identified in the GP plots of DPPC/POPG GUVs at 55 °C. This suggests the presence of defined lipid domains within the liquid crystalline phases, which is most likely the result of DPPC and POPG not mixing due to different interactions between the different headgroups. By measuring the maxima/minima GP values of the peaks and troughs of the GP fluctuations, the lipid phase domains were analysed. The probability distributions of minima/maxima GP show defined peaks, with a peak in GP of 0.48 for GUVs measured at 25 °C, confirming the presence of gel phase domains, that decreases to a GP of 0.2 as temperature increases to 55 °C, showing the transition from the gel phase to liquid crystalline phase. The emergence of a second peak in the

probability distributions at a GP of -0.2, at 35 °C, confirmed the presence of liquid crystalline phase domains, which becomes more prominent as temperature increases to 55 °C indicating the increase in the proportion of liquid crystalline phase domains.

The analysis of single lipid GUVs and mixed lipid GUVs at a range of different temperatures confirmed the feasibility of using GP values to identify and measure lipid phase domains. Therefore, this method was employed to measure the effect of AMP2 interaction on membrane fluidity.

A significant change in the lipid phase domains is seen when DPPC/POPG GUVs are incubated with AMP2. It was found that interaction of AMP2 with DPPC/POPG GUVs at 25 °C results in a distribution of lipid domains similar to those exhibited by untreated samples in the phase transition region (45 °C). The proportion of liquid crystalline domains increases significantly from 30% for untreated GUVs at 25 °C, to 75% for GUVs incubated with AMP2. This indicates that the antimicrobial peptide induces a significant increase in the proportion of liquid crystalline phase domains formed in the membrane. In addition, the size of the domains are smaller for DPPC/POPG GUVs incubated with AMP2 at 25 °C than when untreated. This is an interesting result because a decrease in domain size suggests an increase in the number of domains, since the lipid composition remains unchanged, which means a greater number of domain boundaries in the GUV and so implies an increase in phase boundary defects, which could lead to a weakening of the membrane.

7.2 Further work

To summarise, the results show that AMP2 induces disruptions to the DPPC/POPG GUV membranes that causes lipid disorder, resulting in an increase in the number of liquid crystalline lipid domains detected. An obvious question is how relevant the model membrane is compared to studying the membrane of a live bacterial cell. Therefore, a natural step is to extend this research to study the effects of AMP2 on live bacterial samples, to see if the effects of AMP2 on GUVs incorporated with Laurdan fluorescent dye can be replicated using live bacteria. A second possible study is to use CARS microscopy to probe membrane fluidity, which would

enable label-free studies of the bacterial membrane. A preliminary study was performed to determine the feasibility of the second project.

CARS microscopy has the potential for probing membrane fluidities by using the Raman spectral shifts to attain quantitative information on lipid phases. A paper published by Slipchenko in 2009 shows a Raman spectra of palmitic methyl ester, in which the spectra of the lipid in the gel phase, and the liquid crystalline phase are significantly different (155). Comparing the spectra of the lipid in the gel phase and the lipid in the liquid crystalline phase, two peaks are seen to differ in height depending on the phase of the lipid. The two peaks are at 2850 cm^{-1}, which corresponds to the CH_2 symmetric stretch, and at 2885 cm^{-1}, which corresponds to the CH_2 antisymmetric stretch (155), and the ratio between these two peaks changes between the different lipid phases.

To test if this effect could be reproduced for PC lipids, the Raman spectra of DPPC, 18:0-18:1 PC and 18:0-18:2 PC were measured at room temperature. 18:0-18:1 PC has the PC head group attached to a saturated tail and a tail containing one C=C double bond, 18:0-18:2 PC has one saturated tail and one tail containing two C=C double bonds. Due to the unsaturated bonds, 18:0-18:1 PC and 18:0-18:2 PC are in liquid crystalline phase at room temperature whereas DPPC is in gel phase. Unsaturated lipids were used to test PC lipids in the liquid crystalline phase because the Raman spectrometer was not equipped with a temperature control.

Figure 7.1 shows the bulk Raman spectra of the three samples taken at room temperature. Looking at the intensity ratios of the peaks centred at 2850 cm^{-1} and 2885 cm^{-1}, DPPC peaks show a ratio of approximately 2:3 respectively whereas the unsaturated lipids show a ratio of approximately 1:1 respectively. The indicates that for lipids in gel phase, the 2850 cm^{-1} peak height is around 67% of the 2885 cm^{-1} peak height. As the lipids increase in fluidity the ratio balances to approximately 1:1 ratio. This small study shows the potential of using the spectral peaks, 2850 cm^{-1} and 2885 cm^{-1}, to determine whether the lipids are in gel or liquid crystalline phase. This presents a potential method for determining lipid fluidity by using these Raman bands for attaining CARS signals, whereby the lipid phase can be identified by measuring the ratio between the signal intensities.

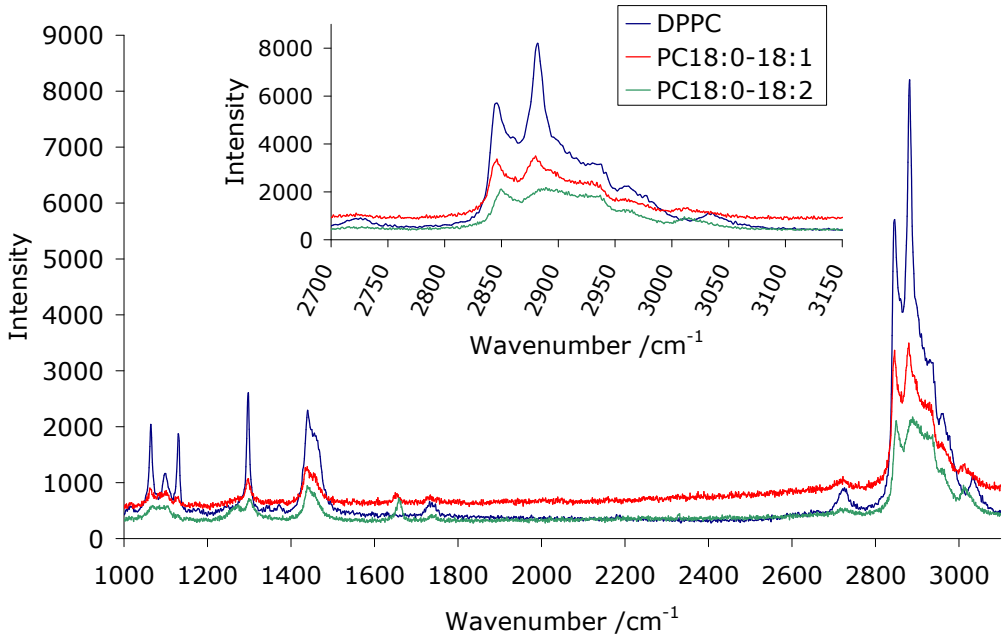

Figure 7.1: Raman spectra of DPPC, single unsaturated PC (PC18:0-18:1) and double unsaturated PC (PC18:0-18:2). Inset: Raman spectra between 2700 cm^{-1} and 3150 cm^{-1}.

Ideally, a multiplex CARS system would be used, which would enable multiple Raman bands to be probed simultaneously (156), however the current optical set-up is only designed for standard CARS imaging. Instead, the lipid phase could possibly be probed by measuring the change in the intensity of the CARS signal for either the CH_2 symmetric or anti-symmetric stretch. (The optical set up described in Chapter 4 was used to image live MG1655 *E. coli* samples.) Firstly, the feasibility of performing CARS microscopy on live *E. coli* was assessed as theoretically, the resolution limit of the CARS system when fully optimised is approximately 0.3 µm, and typical dimensions of *E. coli* are approximately 1×2 µm, therefore the physical size of *E. coli* is close to the resolution limit of the system. So a prerequisite is to ensure that high contrast CARS images could be obtained, and since high-contrast CARS images had already been demonstrated in Chapter 4 by targetting the CH_2 symmetric stretch, CARS imaging at 2845 cm^{-1} Raman band was tested.

CARS images of *E. coli* were acquired jointly with Alex McVey. Figure 7.2(a) shows a CARS image of *E. coli*, generated by targeting the 2845 cm^{-1} Raman vibration. The average laser power of the combined beams measured 179.8 mW before the scanning mirrors and a pixel dwell time of 25 µs was used. Figure 7.2(b) shows an image of the *E. coli* sample when the two laser beams were shifted $180°$ out of phase, in which the visible signal in this image is the non-resonant CARS signal. Since the non-resonant CARS signal level is significantly lower than the signal in Figure 7.2(a), it can be deduced that Figure 7.2(a) contains a resonant CARS signal.

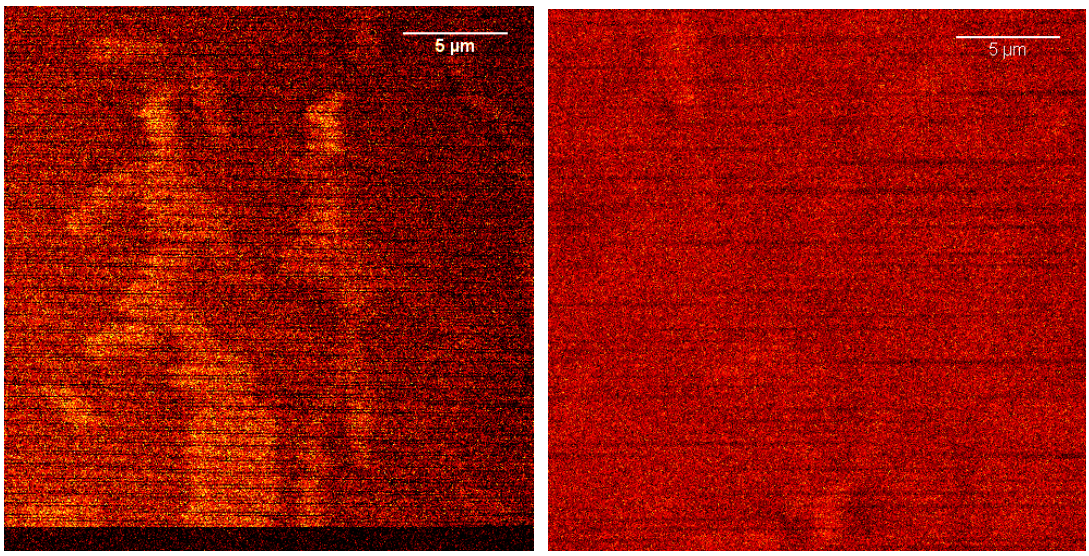

(a) (b)

Figure 7.2: CARS image of *E. coli*, with the average combined laser power (measured before the scanning mirrors) of 179.8 mW and pixel dwell time of 25 µs. The bottom of the image shows the laser beams losing modelock (a). Image of *E. coli* taken with the two laser beams shifted $180°$ out of phase. The average laser power (measured before the scanning mirrors) is 180.0 mW and pixel dwell time is 25 µs (b). The Images were acquired jointly with Alex McVey.

It can be seen that the movement of *E. coli* affected the image, either due to bacterial mobility or due to the effects of laser tweezing. Observation of the sample using brightfield microscopy showed that the bacteria were in constant motion. The bacteria lying on the coverslip tended not to swim, but would tumble and vibrate. The laser scan is from left to right, top to bottom, of the image. Any effect of tweezing would show up in the image as

the object appearing to be elongated from the top left corner to the bottom right corner, due to being dragged by the laser during the scan. This does not seem to be the case, indicating that the blurriness in the image is probably due to bacterial mobility. The bottom of the image shows the laser beams losing modelock, which could possibly be due to back-reflection affecting the stability of the laser.

It is also clear from the images in Figure 7.2 that the image contrast and quality is not sufficient for analytical studies. Extensive modifications to the optical set up are required in order to fully optimise and stabilise the system to the level required for attaining high quality *E. coli* images. Some issues to consider include maximising the excitation efficiency whilst minimising the laser power in order to facilitate effective live cell studies. Currently, neutral density filters are used to control the average laser power. This reduces the overall peak power, which in turn reduces the excitation efficiency. Alternatively, a pulse picker could be used. This component reduces the overall laser power by picking certain pulses and rejecting others within the laser beam therefore maintains the peak power of each pulse. The CARS set up used by S.X. Xie's group to acquire reasonably high contrast CARS images of membrane bilayers consists of a Bragg cell to pulse pick each beam at the rate of 250 kHz (157). After pulse-picking, the average powers of the pump and Stokes laser beams were reduced to 0.3 mW and 0.1 mW respectively, which is a significantly lower laser power than the powers this system is currently capable of working with (also demonstrated in Chapter 4).

This preliminary study shows the potential of using CARS microscopy to quantifiably study changes in membrane fluidity, however much optimization is required, and ideally multiplex CARS capability needs to be included, which is beyond the scope of the project. Therefore, to continue the study on the effects of AMP2 on bacterial membrane fluidity, an advisable next step is to incorporate Laurdan fluorescent dye into live bacterial samples, and study the change in GP using TPF microscopy, which will enable the change in fluidity to be resolved spatially so that changes to the membrane fluidity can be spatially located.

References

[1] Douglas B Murphy and Michael W Davidson. *Fundamentals of light microscopy and electronic imaging*. Wiley-Blackwell, 2012.

[2] Vasilis Ntziachristos. *Going deeper than microscopy: the optical imaging frontier in biology*. *Nature methods*, 7(8):603–614, 2010.

[3] Nuno Moreno, Susan Bougourd, Jim Haseloff, and José A Feijó. *Imaging plant cells*. In *Handbook of biological confocal Microscopy*, pages 769–787. Springer, 2006.

[4] R Cubeddu, D Comelli, C D'Andrea, P Taroni, and G Valentini. *Time-resolved fluorescence imaging in biology and medicine*. *Journal of Physics D: Applied Physics*, 35(9):R61, 2002.

[5] Sean G Megason and Scott E Fraser. *Imaging in systems biology*. *Cell*, 130(5):784–795, 2007.

[6] Steeve Boulant, Mark W Douglas, Laura Moody, Agata Budkowska, Paul Targett-Adams, and John McLauchlan. *Hepatitis C Virus Core Protein Induces Lipid Droplet Redistribution in a Microtubule-and Dynein-Dependent Manner*. *Traffic*, 9(8):1268–1282, 2008.

[7] M. S. Elliot. *The Optical Microscopy of Colloidal Suspensions (Thesis)*. University of Edinburgh, 1999.

[8] S. Bradbury. *An introduction to the optical microscope*. Royal Microscopical Society: Microscopy Handbooks 01, Oxford University press, 1984.

[9] *Royal Microscopical Society Microscropy Handbooks 01: An introduction to the optical microscope*. Oxford University Press, 1984.

[10] A. H. Bennett, Helen Jupnik, Harold Osterberg, and Oscar W. Richards. *Phase Microscopy*. *Transactions of the American Microscopical Society*, 65(2):pp. 99–131, 1946.

[11] Eugene Hecht and Alfred Zajac. *Optics*. Addison Wesley, 4th edition, 2002.

[12] Stanley Schwartz Michael W. Davidson Douglas B. Murphy, Ron Oldfield. *http://www.microscopyu.com/articles/phasecontrast/phasemicroscopy.html*.

[13] Maksymilian Pluta. *Nomarski's DIC microscopy: a review*. In *Phase Contrast and Differential Interference Contrast Imaging Techniques and Applications*, pages 10–25. International Society for Optics and Photonics, 1994.

[14] Walter Lang. *Nomarski differential interference-contrast microscopy*. Oberkochen, Carl Zeiss, 1982.

[15] A. Lasslett. *Principles and applications of differential interference contrast light microscopy. Microscopy and Analysis*, 20:S9–S11, 2006.

[16] M. R. Arnison, K. G. Larkin, C. J. R. Sheppard, N. I. Smith, and C. J. Cogswell. *Linear phase imaging using differential interference contrast microscopy*. *Journal of Microscopy*, 214(1):7–12, 2004.

[17] Joseph R Lakowicz. *Principles of fluorescence spectroscopy*. Springer, 2009.

[18] William W Parson. *Modern Optical Spectroscopy: With Exercises and Examples from Biophysics and Biochemistry*. Springer, 2007.

[19] Roger Y Tsien. *The green fluorescent protein*. *Annual review of biochemistry*, 67(1):509–544, 1998.

[20] Josef Priller, Alexander Flügel, Tim Wehner, Matthias Boentert, Carola A Haas, Marco Prinz, Francisco Fernández-Klett, Konstantin Prass, Ingo Bechmann, Bauke A de Boer, et al. *Targeting gene-modified hematopoietic cells to the central nervous system: use of green fluorescent protein uncovers microglial engraftment*. *Nature medicine*, 7(12):1356–1361, 2001.

[21] Derek A Persons, James A Allay, Esther R Allay, Richard J Smeyne, Richard A Ashmun, Brian P Sorrentino, and Arthur W Nienhuis. *Retroviral-mediated transfer of the green fluorescent protein gene into murine hematopoietic cells facilitates scoring and selection of transduced progenitors in vitro and identification of genetically modified cells in vivo*. *Blood*, 90(5):1777–1786, 1997.

[22] Xue Feng Wang and Brian Herman. *Fluorescence imaging spectroscopy and microscopy*. Wiley, 1996.

[23] M. Oheim, D. J. Michael, M. Geisbauer, D. Madsen, and R. H. Chow. *Principles of two-photon excitation fluorescence microscopy and other nonlinear imaging approaches*. *Advanced Drug Delivery Reviews*, 58:788–808, 2006.

[24] C. L. Evans and X. S. Xie. *Coherent Anti-Stokes Raman Scattering Microscopy: Chemical Imaging for Biology and Medicine*. *Annu. Rev. Anal. Chem.*, 1:883–909, 2008.

[25] John R Ferraro. *Introductory raman spectroscopy*. Academic press, 2003.

[26] Ewen Smith and Geoffrey Dent. *Modern Raman spectroscopy: a practical approach*. Wiley, 2005.

[27] Iain Thomas Robinson. *Nonlinear laser microscopy for the study of virus-host interactions*. PhD thesis, The University of Edinburgh, 2010.

[28] Ji-Xin Cheng, Andreas Volkmer, and X Sunney Xie. *Theoretical and experimental characterization of coherent anti-Stokes Raman scattering microscopy*. *JOSA B*, 19(6):1363–1375, 2002.

[29] Xiaolin Nan, Eric O Potma, and X Sunney Xie. *Nonperturbative chemical imaging of organelle transport in living cells with coherent anti-stokes Raman scattering microscopy*. *Biophysical journal*, 91(2):728–735, 2006.

[30] Andreas Volkmer. *Coherent Raman Scattering Microscopy*. In *Emerging Raman Applications and Techniques in Biomedical and Pharmaceutical Fields*, pages 111–152. Springer, 2010.

[31] Ji-Xin Cheng and Xiaoliang Sunney Xie. *Coherent Raman Scattering Microscopy*, volume 1. CRC PressI Llc, 2012.

[32] Michiel Müller and Andreas Zumbusch. *Coherent anti-Stokes Raman Scattering Microscopy*. *ChemPhysChem*, 8(15):2156–2170, 2007.

[33] Robert Tyson. *Principles of adaptive optics*. CRC PressI Llc, 2010.

[34] Yuen-Ron Shen. *The principles of nonlinear optics*. *New York, Wiley-Interscience, 1984, 575 p.*, 1, 1984.

[35] Robert W Boyd. *Nonlinear optics*. Academic press, 2003.

[36] Ji-Xin Cheng, Lewis D Book, and X Sunney Xie. *Polarization coherent anti-Stokes Raman scattering microscopy*. *Optics Letters*, 26(17):1341–1343, 2001.

[37] Christian W Freudiger, Wei Min, Brian G Saar, Sijia Lu, Gary R Holtom, Chengwei He, Jason C Tsai, Jing X Kang, and X Sunney Xie. *Label-free biomedical imaging with high sensitivity by stimulated Raman scattering microscopy*. *Science*, 322(5909):1857–1861, 2008.

[38] Ji-xin Cheng, Andreas Volkmer, Lewis D Book, and X Sunney Xie. *An epi-detected coherent anti-Stokes Raman scattering (E-CARS) microscope with high spectral resolution and high sensitivity*. *The Journal of Physical Chemistry B*, 105(7):1277–1280, 2001.

[39] A. Yu, X. Ye, D. Ionascu, W. Cao, and P.M. Champion. *Two-colour pump-probe laser spectroscopy instrument with picosecond time-resolved electronic delay and extended scan range*. *Rev. Sci. Instrum.*, 76:114301–1–8, 2005.

[40] Stephen R. Bolsover, Jeremy S. Hyams, Elizabeth A. Shephard, Hugh A. White, and Claudia G. Wiedemann. *Cells and Tissues*, pages 1–18. John Wiley & Sons, Inc., 2004.

[41] Kim KS Salton MRJ. *Medical Microbiology. 4th edition. Galveston (TX)*. University of Texas Medical Branch at Galveston, http://www.ncbi.nlm.nih.gov/books/NBK8477/, 1996.

[42] Sigrid Brynestad, Bjørnar Synstad, and Per Einar Granum. *The Clostridium perfringens enterotoxin gene is on a transposable element in type A human food poisoning strains*. *Microbiology*, 143(7):2109–2115, 1997.

[43] Tomaz Koprivnjak and Andreas Peschel. *Bacterial resistance mechanisms against host defense peptides*. *Cellular and Molecular Life Sciences*, 68(13):2243–2254, 2011.

[44] Nikken Wiradharma, Ulung Khoe, Charlotte AE Hauser, See Voon Seow, Shuguang Zhang, and Yi-Yan Yang. *Synthetic cationic amphiphilic< i> α</i>-helical peptides as antimicrobial agents*. *Biomaterials*, 32(8):2204–2212, 2011.

[45] L. Beney and P. Gervais. *Influence of the fluidity of the membrane on the response of microorganisms to environmental stresses*. *Applied microbiology and biotechnology*, 57(1):34–42, 2001.

[46] Ad C Fluit, Maarten R Visser, and Franz-Josef Schmitz. *Molecular detection of antimicrobial resistance*. *Clinical microbiology reviews*, 14(4):836–871, 2001.

[47] A Mrozik, Z Piotrowska-Seget, and S Labuzek. *Cytoplasmatic bacterial membrane responses to environmental perturbations*. *Polish Journal of Environmental Studies*, 13(5):487–494, 2004.

[48] Mohammad J. Hajipour, Katharina M. Fromm, Ali Akbar Ashkarran, Dorleta Jimenez de Aberasturi, Idoia Ruiz de Larramendi, Teofilo Rojo, Vahid Serpooshan, Wolfgang J. Parak, and Morteza Mahmoudi. *Antibacterial properties of nanoparticles*. *Trends in Biotechnology*, 30(10):499 – 511, 2012.

[49] EJJ Lugtenberg and R Peters. *Distribution of lipids in cytoplasmic and outer membranes of< i> Escherichia coli</i> K12*. *Biochimica et Biophysica Acta (BBA)-Lipids and Lipid Metabolism*, 441(1):38–47, 1976.

[50] June R Scott and Timothy C Barnett. *Surface proteins of gram-positive bacteria and how they get there*. *Annu. Rev. Microbiol.*, 60:397–423, 2006.

[51] Michael R Yeaman and Nannette Y Yount. *Mechanisms of antimicrobial peptide action and resistance*. *Pharmacological reviews*, 55(1):27–55, 2003.

[52] Arash Izadpanah and Richard L. Gallo. *Antimicrobial peptides*. *Journal of the American Academy of Dermatology*, 52(3):381 – 390, 2005.

[53] G. Bell and P.H. Gouyon. *Arming the enemy: the evolution of resistance to self-proteins*. *Microbiology*, 149(6):1367–1375, 2003.

[54] M.N. Melo, R. Ferre, and M.A.R.B. Castanho. *Antimicrobial peptides: linking partition, activity and high membrane-bound concentrations*. *Nature Reviews Microbiology*, 7(3):245–250, 2009.

[55] Hiromi Sato and Jimmy B Feix. *Peptide–membrane interactions and mechanisms of membrane destruction by amphipathic α-helical antimicrobial peptides*. *Biochimica et Biophysica Acta (BBA)-Biomembranes*, 1758(9):1245–1256, 2006.

[56] Kevin L Piers and Robert EW Hancock. *The interaction of a recombinant cecropin/melittin hybrid peptide with the outer membrane of Pseudomonas aeruginosa*. *Molecular microbiology*, 12(6):951–958, 1994.

[57] Kevin L Piers, Melissa H Brown, and RE Hancock. *Improvement of outer membrane-permeabilizing and lipopolysaccharide-binding activities of an antimicrobial cationic peptide by C-terminal modification. Antimicrobial agents and chemotherapy*, 38(10):2311–2316, 1994.

[58] Yechiel Shai. *Mode of action of membrane active antimicrobial peptides*. *Biopolymers*, 66(4):236–248, 2002.

[59] Katsumi Matsuzaki. *Magainins as paradigm for the mode of action of pore forming polypeptides*. *Biochimica et Biophysica Acta (BBA) - Reviews on Biomembranes*, 1376(3):391–400, November 1998.

[60] K.A. Brogden. *Antimicrobial peptides: pore formers or metabolic inhibitors in bacteria? Nature Reviews Microbiology*, 3(3):238–250, 2005.

[61] Richard M. Epand and Raquel F. Epand. *Lipid domains in bacterial membranes and the action of antimicrobial agents*. *Biochimica et Biophysica Acta (BBA) - Biomembranes*, 1788(1):289–294, January 2009.

[62] Hayet Bensikaddour, Karim Snoussi, Laurence Lins, Françoise Van Bambeke, Paul M Tulkens, Robert Brasseur, Erik Goormaghtigh, and Marie-Paule Mingeot-Leclercq. *Interactions of ciprofloxacin with DPPC and DPPG: Fluorescence anisotropy, ATR-FTIR and< sup> 31</sup> P NMR spectroscopies and conformational analysis*. *Biochimica et Biophysica Acta (BBA)-Biomembranes*, 1778(11):2535–2543, 2008.

[63] Wilson CK Poon and David Andelman. *Soft condensed matter physics in molecular and cell biology*, volume 59. Taylor & Francis Group, 2006.

[64] Lewis J et al. Alberts B, Johnson A. *Fibroblasts and Their Transformations: The Connective-Tissue Cell Family*. In *Molecular Biology of the Cell*. New York: Garland Science, 4th edition. edition, 2002.

[65] Robin J McAnulty. *Fibroblasts and myofibroblasts: their source, function and role in disease*. *The international journal of biochemistry & cell biology*, 39(4):666–671, 2007.

[66] George J. Todaro and Howard Green. *QUANTITATIVE STUDIES OF THE GROWTH OF MOUSE EMBRYO CELLS IN CULTURE AND THEIR DEVELOPMENT INTO ESTABLISHED LINES*. *The Journal of Cell Biology*, 17(2):299–313, http://jcb.rupress.org/content/17/2/299.full.pdf+html, 1963.

[67] Margarete Digel, Robert Ehehalt, and Joachim Füllekrug. *Lipid droplets lighting up: insights from live microscopy*. *FEBS letters*, 584(11):2168–2175, 2010.

[68] Constantine Londos, Dawn L Brasaemle, Charles J Schultz, Jere P Segrest, Alan R Kimmel, et al. *Perilipins, ADRP, and other proteins that associate with intracellular neutral lipid droplets in animal cells.* In *Seminars in cell & developmental biology*, volume 10, page 51, 1999.

[69] Yale School of Medicine. *http://www.yalescientific.org/wp-content/uploads/2013/04/Picture-2.jpg*.

[70] Yuki Ohsaki, Jinglei Cheng, Akikazu Fujita, Toshinobu Tokumoto, and Toyoshi Fujimoto. *Cytoplasmic lipid droplets are sites of convergence of proteasomal and autophagic degradation of apolipoprotein B. Molecular biology of the cell*, 17(6):2674–2683, 2006.

[71] Sally Martin and Robert G Parton. *Lipid droplets: a unified view of a dynamic organelle*. *Nature Reviews Molecular Cell Biology*, 7(5):373–378, 2006.

[72] Steven P Gross. *Hither and yon: a review of bi-directional microtubule-based transport*. *Physical Biology*, 1(2):R1, 2004.

[73] Michael A Welte. *Bidirectional transport along microtubules*. *Current Biology*, 14(13):R525–R537, 2004.

[74] Jonathan W Driver, D Kenneth Jamison, Karthik Uppulury, Arthur R Rogers, Anatoly B Kolomeisky, and Michael R Diehl. *Productive cooperation among processive motors depends inversely on their mechanochemical efficiency*. *Biophysical journal*, 101(2):386–395, 2011.

[75] Thomas C Mettenleiter, Barbara G Klupp, and Harald Granzow. *Herpesvirus assembly: a tale of two membranes*. *Current opinion in microbiology*, 9(4):423–429, 2006.

[76] C. Sweet. *The pathogenicity of cytomegalovirus*. *FEMS Microbiology Reviews*, 23:457–482, 1999.

[77] David Hames and Nigel Hooper. *Instant notes in biochemistry*. Taylor & Francis, 2000.

[78] D. M. Jones and J. McLauchlan. *Hepatitis C Virus: Assembly and Release of Virus Particles*. *J. Biol. Chem.*, 285:22733–22739, 2010.

[79] R. K. Lyn, D. C Kennedy, A. Stolow, A. Ridsdale, and J. P. Pezacki. *Dynamics of lipid droplets induced by the hepatitis C virus core protein*. *Biochem. Biophys. Res. Commun.*, 399:518–524, 2010.

[80] E. Herker, C. Harris, C. Hernandez, A. Carpentier, K. Kaehlcke, A. R. Rosenberg, R. V. Farese, and M. Ott. *Efficient hepatitis C virus particle formation requires diacylglycerol acyltransferase-1,*. *Nat. Med.*, 16:1295–1298, 2010.

[81] V. Lohmann R. Bartenschlager, F. Penn and P. Andre. *Assembly of infectious hepatitis C virus particles,*. *Trends in Microbiology*, 19:95–103, 2010.

[82] John McLauchlan. *Lipid droplets and hepatitis C virus infection*. *Biochimica et Biophysica Acta (BBA)-Molecular and Cell Biology of Lipids*, 1791(6):552–559, 2009.

[83] Mathieu Blanc, Wei Yuan Hsieh, Kevin A. Robertson, Steven Watterson, Guanghou Shui, Paul Lacaze, Mizanur Khondoker, Paul Dickinson, Garwin Sing, Sara RodrÃguez-MartÃn, Peter Phelan, Thorsten Forster, Birgit Strobl, Matthias Maller, Rudolph Riemersma, Timothy Osborne, Markus R. Wenk, Ana Angulo, and Peter Ghazal. *Host Defense against Viral Infection Involves Interferon Mediated Down-Regulation of Sterol Biosynthesis*. *PLoS Biol*, 9(3):e1000598, 03 2011.

[84] D.J. Murphy. *The biogenesis and functions of lipid bodies in animals, plants and microorganisms*. *Progress Lipid Res.*, 40:325–438, 2001.

[85] Amir Kol and Peter Libby. *The mechanisms by which infectious agents may contribute to atherosclerosis and its clinical manifestations*. *Trends in cardiovascular medicine*, 8(5):191–199, 1998.

[86] John P Tomtishen III. *Human cytomegalovirus tegument proteins (pp65, pp71, pp150, pp28)*. *Virology journal*, 9(1):22, 2012.

[87] Marko Reschke. *http://www.virology.net/big_virology/bvdnaherpes.html*, 1997.

[88] Thomas C Mettenleiter, Barbara G Klupp, and Harald Granzow. *Herpesvirus assembly: an update*. *Virus research*, 143(2):222–234, 2009.

[89] Gulam H Syed, Yutaka Amako, and Aleem Siddiqui. *Hepatitis C virus hijacks host lipid metabolism*. *Trends in Endocrinology & Metabolism*, 21(1):33–40, 2010.

[90] Masayoshi Fukasawa. *Cellular lipid droplets and hepatitis C virus life cycle*. *Biological and Pharmaceutical Bulletin*, 33(3):355–359, 2010.

[91] R.V. Farese Y. Guo, K. R. Cordes and T.C. Walther. *Lipid droplets at a glance*. *J. Cell Sci.*, 122:749–752, 2009.

[92] J. Cheng. *Coherent Anti-Stokes Raman Scattering Microscopy*. *Appl. Spectroscopy*, 61:197A–208A, 2007.

[93] Roger Y Tsien. *Rosy dawn for fluorescent proteins*. *Nature Biotechnology*, 17(10):956–957, 1999.

[94] P. Ghazal A. Angulo and M. Messerle. *'The major immediate-early gene ie3 of mouse cytomegalovirus is essential for viral growth*. *J. Virol.*, 74:11129–11136, 2000.

[95] I. Robinson, M. A. Ochsenkühn, C. J. Campbell, G. Giraud, W. J. Hossack, J. Arlt, and J. Crain. *Intracellular imaging of host-pathogen interactions using combined CARS and two-photon fluorescence microscopies*. *J. Biophoton.*, 3:138–146, 2010.

[96] N. E. Bishop. *Hepatitis A virus replication: an intermediate in the uncoating process," Intervirology*. *Intervirology*, 43:36–47, 2000.

[97] F. J. Miller G. Sluder, J. J. Nordberg and E. H. Hinchcliffe. *Live Cell Imaging: A Laboratory Manual*, chapter A sealed preparation for long-term observations of cultured cells, pages 345–349. Cold Spring Harbor Laboratory Press, 2005.

[98] B. Agate F. Gunn-Moore D. J. Stevenson, D. J. Carnegie and K. Dholakia. *Long-term cell culture on a microscope stage: the carrel flask revisited*. *Microscopy and Analysis*, 22:9–11, 2008.

[99] M. E. Dailey, D. C. Focht, A. Khodjakov, C. L. Rieder, K. R. Spring, N. S. Claxton, S. G. Olenych, J. D. Griffin, and M. W. Davidson. *Maintaining live cells on the microscope stage*.

[100] T. Shenk E. S. Mocarski and R. F. Pass. *Fields Virology*, 2006.

[101] Christine SY Wong, Iain Robinson, Michael A Ochsenkühn, Jochen Arlt, William J Hossack, and Jason Crain. *Changes to lipid droplet configuration in mCMV-infected fibroblasts: live cell imaging with simultaneous CARS and two-photon fluorescence microscopy*. *Biomedical optics express*, 2(9):2504, 2011.

[102] J. X. Cheng X. Nan and X. S. Xie. *Vibrational imaging of lipid droplets in live fibroblast cells with coherent anti-Stokes Raman scattering microscopy*. *J. Lipid. Res.*, 44:2202–2208, 2003.

[103] D. W. Piston W. Denk and W. W. Webb. *Handbook of Biological confocal microscopy*, chapter Multi-photon molecular excitation in laser scanning microscopy, pages 535–549. Springer, 2006.

[104] J. Bewersdorf and S. W. Hell. *Picosecond pulsed two-photon imaging with repetition rates of 200 and 400 MHz. J. Microsc.*, 191:28–38, 1998.

[105] M. A. Hayat. *Principles and Techniques of Electron Microscopy Biological Applications*, chapter Chemical fixation, pages 43–44. Cambridge University Press, 2000.

[106] H. Fried and U. Kutay. *Nucleocytoplasmic transport: taking an inventory*. *Cell. Mol. Life Sci.*, 60:1659–1688, 2003.

[107] W. Muranyi, J. Haas, M. Wagner, G. Krohne, and U. H. Koszinowski. *Cytomegalovirus recruitment of cellular kinases to dissolve the nuclear lamina*. *Science*, 297:854–857, 2002.

[108] W. S. Rasband. *"ImageJ"*.

[109] Rodney K Lyn, David C Kennedy, Albert Stolow, Andrew Ridsdale, and John Paul Pezacki. *Dynamics of lipid droplets induced by the hepatitis C virus core protein*. *Biochemical and biophysical research communications*, 399(4):518–524, 2010.

[110] Maksymilian Pluta. *Nomarski's DIC microscopy: a review*. pages 10–25, 1994.

[111] Christian Jüngst, Martin J Winterhalder, and Andreas Zumbusch. *Fast and long term lipid droplet tracking with CARS microscopy*. *Journal of Biophotonics*, 4(6):435–441, 2011.

[112] Marcus Otten, Amitabha Nandi, Delphine Arcizet, Mari Gorelashvili, Benjamin Lindner, and Doris Heinrich. *Local motion analysis reveals impact of the dynamic cytoskeleton on intracellular subdiffusion*. *Biophysical Journal*, 102(4):758–767, 2012.

[113] Xavier Michalet. *Mean square displacement analysis of single-particle trajectories with localization error: Brownian motion in an isotropic medium*. *Physical Review E*, 82(4):041914, 2010.

[114] Sébastien Huet, Erdem Karatekin, Viet Samuel Tran, Isabelle Fanget, Sophie Cribier, and Jean-Pierre Henry. *Analysis of transient behavior in complex trajectories: application to secretory vesicle dynamics*. *Biophysical journal*, 91(9):3542, 2006.

[115] John C. Crocker and Eric R. Weeks. *http://www.physics.emory.edu/ weeks/idl/msd.html*.

[116] Nicholas Barnes. *Private communications: ImageJ script*. 2013.

[117] Marina K. Kuimova, Gokhan Yahioglu, James A. Levitt, and Klaus Suhling. *Molecular Rotor Measures Viscosity of Live Cells via Fluorescence Lifetime Imaging*. *Journal of the American Chemical Society*, 130(21):6672–6673, http://pubs.acs.org/doi/pdf/10.1021/ja800570d, 2008. PMID: 18457396.

[118] Bionumbers database. *http://bionumbers.hms.harvard.edu//bionumber.aspx?id=102561&ver=2*.

[119] Fei Liu, Tong Wu, Jianfang Cao, Shuang Cui, Zhigang Yang, Xinxin Qiang, Shiguo Sun, Fengling Song, Jiangli Fan, Jingyun Wang, et al. *Ratiometric Detection of Viscosity Using a Two-Photon Fluorescent Sensor*. *Chemistry-A European Journal*, 19(5):1548–1553, 2013.

[120] A.H. Wyllie. *Cell death: a new classification separating apoptosis from necrosis*. In I.D. Bowen and R.A. Lockshin, editors, *Cell death in biology and pathology*, pages 9–34. Springer Netherlands, 1981.

[121] PeterG.H. Clarke. *Developmental cell death: morphological diversity and multiple mechanisms*. *Anatomy and Embryology*, 181(3):195–213, 1990.

[122] Marina K Kuimova, Stanley W Botchway, Anthony W Parker, Milan Balaz, Hazel A Collins, Harry L Anderson, Klaus Suhling, and Peter R Ogilby. *Imaging intracellular viscosity of a single cell during photoinduced cell death*. *Nature chemistry*, 1(1):69–73, 2009.

[123] Dawen Cai, Kristen J. Verhey, and Edgar Meyhöfer. *Tracking Single Kinesin Molecules in the Cytoplasm of Mammalian Cells*, June 2007.

[124] Adam G Hendricks, Erika LF Holzbaur, and Yale E Goldman. *Force measurements on cargoes in living cells reveal collective dynamics of microtubule motors*. *Proceedings of the National Academy of Sciences*, 109(45):18447–18452, 2012.

[125] Peter A Sims and X Sunney Xie. *Probing dynein and kinesin stepping with mechanical manipulation in a living cell*. *ChemPhysChem*, 10(9-10):1511–1516, 2009.

[126] Comert Kural, Hwajin Kim, Sheyum Syed, Gohta Goshima, Vladimir I Gelfand, and Paul R Selvin. *Kinesin and dynein move a peroxisome in vivo: a tug-of-war or coordinated movement?* *Science*, 308(5727):1469–1472, 2005.

[127] Erika LF Holzbaur and Yale E Goldman. *Coordination of molecular motors: from in vitro assays to intracellular dynamics*. *Current Opinion in Cell Biology*, 22(1):4 – 13, 2010. Cell structure and dynamics.

[128] D Kenneth Jamison, Jonathan W Driver, and Michael R Diehl. *Cooperative responses of multiple kinesins to variable and constant loads*. *Journal of Biological Chemistry*, 287(5):3357–3365, 2012.

[129] Peter William Atkins and Julio De Paula. *Atkins' physical chemistry*, volume 8. Oxford University Press Oxford, 2006.

[130] M. Zasloff et al. *Antimicrobial peptides of multicellular organisms*. *Nature*, 415(6870):389–395, 2002.

[131] R.E.W. Hancock and H.G. Sahl. *Antimicrobial and host-defense peptides as new anti-infective therapeutic strategies*. *Nature biotechnology*, 24(12):1551–1557, 2006.

[132] Raquel F. Epand, Margaret A. Schmitt, Samuel H. Gellman, and Richard M. Epand. *Role of membrane lipids in the mechanism of bacterial species selective toxicity by two alphabeta-antimicrobial peptides*. *Biochimica et Biophysica Acta (BBA) - Biomembranes*, 1758(9):1343–1350, September 2006.

[133] Lisa M. Hays, John H. Crowe, Willem Wolkers, and Sergey Rudenko. *Factors Affecting Leakage of Trapped Solutes from Phospholipid Vesicles during Thermotropic Phase Transitions*. *Cryobiology*, 42(2):88–102, March 2001.

[134] Armelle Varnier, Frederique Kermarrec, Iulia Blesneac, Christophe Moreau, Lavinia Liguori, JeanLuc Lenormand, and Nathalie Picollet-D'hahan. *A Simple Method for the Reconstitution of Membrane Proteins into Giant Unilamellar Vesicles*. *Journal of Membrane Biology*, 233:85–92, 2010.

[135] Jacob N Israelachvili. *Intermolecular and surface forces: revised third edition*. Academic press, 2011.

[136] Baptiste Lamarre, Jascindra Ravi, and Maxim G Ryadnov. *GeT peptides: a single-domain approach to gene delivery*. *Chemical Communications*, 47(32):9045–9047, 2011.

[137] Paulina D. Rakowska, Haibo Jiang, Santanu Ray, Alice Pyne, Baptiste Lamarre, Matthew Carr, Peter J. Judge, Jascindra Ravi, Ulla I. M. Gerling, Beate Koksch, Glenn J. Martyna, Bart W. Hoogenboom, Anthony Watts, Jason Crain, Chris R. M. Grovenor, and Maxim G. Ryadnov. *Nanoscale imaging reveals laterally expanding antimicrobial pores in lipid bilayers*. *Proceedings of the National Academy of Sciences*, 110(22):8918–8923, http://www.pnas.org/content/110/22/8918.full.pdf+html, 2013.

[138] R.L. Biltonen and D. Lichtenberg. *The use of differential scanning calorimetry as a tool to characterize liposome preparations*. *Chemistry and physics of lipids*, 64(1):129–142, 1993.

[139] Avanti Lipids. *http://avantilipids.com/*.

[140] John F Nagle and Stephanie Tristram-Nagle. *Structure of lipid bilayers*. *Biochimica et Biophysica Acta (BBA)-Reviews on Biomembranes*, 1469(3):159–195, 2000.

[141] T. Parasassi, E.K. Krasnowska, L. Bagatolli, and E. Gratton. *Laurdan and Prodan as polarity-sensitive fluorescent membrane probes*. *Journal of fluorescence*, 8(4):365–373, 1998.

[142] SA Sanchez, MA Tricerri, G. Gunther, and E. Gratton. *Laurdan generalized polarization: from cuvette to microscope*. *Modern Research and Educational Topics in Microscopy, Formatex*, pages 1007–1014, 2007.

[143] Carme Sua¡rez-Germa , M.Teresa Montero, Jordi Ignas-Mullol, Jordi Herna¡ndez-Borrell, and ascar Domanech. *Acyl Chain Differences in Phosphatidylethanolamine Determine Domain Formation and LacY Distribution in Biomimetic Model Membranes*. *The Journal of Physical Chemistry B*, 115(44):12778–12784, http://pubs.acs.org/doi/pdf/10.1021/jp206369k, 2011.

[144] Aline D Lúcio, Cíntia C Vequi-Suplicy, Roberto M Fernandez, and M Teresa Lamy. *Laurdan spectrum decomposition as a tool for the analysis of surface bilayer structure and polarity: a study with DMPG, peptides and cholesterol*. *Journal of fluorescence*, 20(2):473–482, 2010.

[145] S. Fahsel, EM Pospiech, M. Zein, TL Hazlet, E. Gratton, and R. Winter. *Modulation of concentration fluctuations in phase-separated lipid membranes by polypeptide insertion. Biophysical journal*, 83(1):334, 2002.

[146] Jana Schwarz-Linek. *Private communications: University of Edinburgh, Physics and Astronomy*. 2012.

[147] Miglena I. Angelova and Dimiter S. Dimitrov. *Liposome electroformation*. *Faraday Discuss. Chem. Soc.*, 81:303–311, 1986.

[148] Suliana Manley and Vernita D. Gordon. *Making Giant Unilamellar Vesicles via Hydration of a Lipid Film*. John Wiley & Sons, Inc., 2001.

[149] Jean-Baptiste Manneville, CÃ©cile Leduc, Benoit Sorre, and Guillaume Drin. *Chapter 3 - Studying In Vitro Membrane Curvature Recognition by Proteins and its Role in Vesicular Trafficking*. In Gilbert Di Paolo and Markus R Wenk, editors, *Lipids*, volume Volume 108, pages 47–71. Academic Press, 2012.

[150] Maxim G. Ryadnov, Galina V. Mukamolova, Ayman S. Hawrani, James Spencer, and Roscoe Platt. *RE Coil: An Antimicrobial Peptide Regulator*. *Angewandte Chemie International Edition*, 48(51):9676–9679, 2009.

[151] Christoph Herold, Grzegorz Chwastek, Petra Schwille, and Eugene P. Petrov. *Efficient Electroformation of Supergiant Unilamellar Vesicles Containing Cationic Lipids on ITO-Coated Electrodes*. *Langmuir*, 28(13):5518–5521, March 2012.

[152] Nicholas Barnes. *Private communications: ImageJ plugin script for measuring the intensities of the GUV fluorescence*. 2013.

[153] Z.V. Leonenko, E. Finot, H. Ma, T.E. S. Dahms, and D.T. Cramb. *Investigation of Temperature-Induced Phase Transitions in DOPC and DPPC Phospholipid Bilayers Using Temperature-Controlled Scanning Force Microscopy*, June 2004.

[154] L. Li and J.X. Cheng. *Coexisting stripe-and patch-shaped domains in giant unilamellar vesicles*. *Biochemistry*, 45(39):11819–11826, 2006.

[155] M.N. Slipchenko, T.T. Le, H. Chen, and J.X. Cheng. *High-speed vibrational imaging and spectral analysis of lipid bodies by compound Raman microscopy*. *The Journal of Physical Chemistry B*, 113(21):7681–7686, 2009.

[156] Hilde A Rinia, Mischa Bonn, and Michiel Müller. *Quantitative multiplex CARS spectroscopy in congested spectral regions*. *The Journal of Physical Chemistry B*, 110(9):4472–4479, 2006.

[157] E.O. Potma and X.S. Xie. *Detection of single lipid bilayers with coherent anti-Stokes Raman scattering (CARS) microscopy*. *Journal of Raman spectroscopy*, 34(9):642–650, 2003.

Publication

Changes to lipid droplet configuration in mCMV-infected fibroblasts: live cell imaging with simultaneous CARS and two-photon fluorescence microscopy

Changes to lipid droplet configuration in mCMV-infected fibroblasts: live cell imaging with simultaneous CARS and two-photon fluorescence microscopy

Christine S. Y. Wong,[1,*] Iain Robinson,[1] Michael A. Ochsenkühn,[2] Jochen Arlt,[1] William J. Hossack,[1] and Jason Crain[1]

[1]*Collaborative Optical Spectroscopy Micromanipulation and Imaging Centre (COSMIC), School of Physics and Astronomy, The University of Edinburgh, Edinburgh, Mayfield Road, Edinburgh, EH9 3JZ, UK*

[2]*School of Chemistry, The University of Edinburgh, West Mains Road, Edinburgh, EH9 3JJ, UK*

**c.s.y.wong@ed.ac.uk*

Abstract: We have performed multimodal imaging of live fibroblast cells infected by murine cytomegalovirus (mCMV). The infection process was monitored by imaging the two-photon fluorescence signal from a GFP-expressing strain of mCMV, whilst changes to lipid droplet configuration were observed by CARS imaging. This allowed us to identify three visually distinct stages of infection. Quantitative analysis of lipid droplet number and size distributions were obtained from live cells, which showed significant perturbations across the different stages of infection. The CARS and two-photon images were acquired simultaneously and the experimental design allowed incorporation of an environmental control chamber to maintain cell viability. Photodamage to the live cell population was also assessed.

© 2011 Optical Society of America

OCIS codes: (180.0180) Microscopy; (170.3880) Medical and biological imaging; (170.1530) Cell analysis; (190.4380) Nonlinear optics, four-wave mixing; (170.2520) Fluorescence microscopy.

References and links

1. I. Robinson, M. A. Ochsenkühn, C. J. Campbell, G. Giraud, W. J. Hossack, J. Arlt, and J. Crain, "Intracellular imaging of host-pathogen interactions using combined CARS and two-photon fluorescence microscopies," J. Biophoton. **3**, 138–146 (2010).
2. J. Cheng, "Coherent anti-Stokes Raman scattering microscopy," Appl. Spectrosc. **61**, 197A–208A (2007).
3. C. L. Evans and X. S. Xie, "Coherent anti-Stokes Raman scattering microscopy: chemical imaging for biology and medicine," Annu. Rev. Anal. Chem. **1**, 883–909 (2008).
4. Y. Guo, K. R. Cordes, R.V. Farese, and T.C. Walther, "Lipid droplets at a glance," J. Cell Sci. **122**, 749–752 (2009).
5. D. M. Jones and J. McLauchlan, "Hepatitis C virus: assembly and release of virus particles," J. Biol. Chem. **285**, 22733–22739 (2010).
6. R. K. Lyn, D. C Kennedy, A. Stolow, A. Ridsdale, and J. P. Pezacki, "Dynamics of lipid droplets induced by the hepatitis C virus core protein," Biochem. Biophys. Res. Commun. **399**, 518–524 (2010).
7. E. Herker, C. Harris, C. Hernandez, A. Carpentier, K. Kaehlcke, A. R. Rosenberg, R. V. Farese, and M. Ott, "Efficient hepatitis C virus particle formation requires diacylglycerol acyltransferase-1," Nat. Med. **16**, 1295–1298 (2010).
8. R. Bartenschlager, F. Penn, V. Lohmann and P. Andre, "Assembly of infectious hepatitis C virus particles," Trends Microbiol. **19**, 95–103 (2010).

#147177 - $15.00 USD Received 9 May 2011; revised 5 Jun 2011; accepted 8 Jul 2011; published 2 Aug 2011

9. A. Angulo, P. Ghazal, and M. Messerle, "The major immediate-early gene *ie3* of mouse cytomegalovirus is essential for viral growth," J. Virol. **74**, 11129–11136 (2000).
10. N. E. Bishop, "Hepatitis A virus replication: an intermediate in the uncoating process," Intervirology **43**, 36–47 (2000).
11. G. Sluder, J. J. Nordberg, F. J. Miller, and E. H. Hinchcliffe, "A sealed preparation for long-term observations of cultured cells," in *Live Cell Imaging: A Laboratory Manual*, R. D. Goldman and D. L. Spector eds. (Cold Spring Harbor Laboratory Press, 2005), pp. 345–349.
12. D. J. Stevenson, D. J. Carnegie, B. Agate, F. Gunn-Moore, and K. Dholakia, "Long-term cell culture on a microscope stage: the carrel flask revisited." Microsc. Anal. **22**, 9–11 (2008).
13. M. E. Dailey, D. C. Focht, A. Khodjakov, C. L. Rieder, K. R. Spring, N. S. Claxton, S. G. Olenych, J. D. Griffin, and M. W. Davidson, "Maintaining live cells on the microscope stage," http://www.microscopyu.com/articles/livecellimaging/livecellmaintenance.html.
14. E. S. Mocarski, T. Shenk, and R. F. Pass, "Cytomegaloviruses," in *Fields Virology*, D. M. Knipe and P. M. Howley eds. (Lippincott Williams and Wilkins, 2006) pp. 2702–2772.
15. A. Yu, X. Ye, D. Ionascu, W. Cao, and P.M. Champion, "Two-colour pump-probe laser spectroscopy instrument with picosecond time-resolved electronic delay and extended scan range," Rev. Sci. Instrum. **76** 114301 (2005).
16. X. Nan, J. X. Cheng, and X. S. Xie, "Vibrational imaging of lipid droplets in live fibroblast cells with coherent anti-Stokes Raman scattering microscopy," J. Lipid. Res. **44**, 2202–2208 (2003).
17. W. Denk, D. W. Piston, and W. W. Webb, "Multi-photon molecular excitation in laser scanning microscopy," in *Handbook of Biological Confocal Microscopy* J. B. Pawley, (Springer, 2006) pp. 535–549.
18. J. Bewersdorf and S. W. Hell, "Picosecond pulsed two-photon imaging with repetition rates of 200 and 400 MHz," J. Microsc. **191**, 28–38 (1998).
19. M. A. Hayat, "Chemical fixation," in *Principles and Techniques of Electron Microscopy Biological Applications* (Cambridge University Press, 2000), pp. 43–44.
20. H. Fried and U. Kutay, "Nucleocytoplasmic transport: taking an inventory," Cell. Mol. Life Sci. **60**, 1659–1688 (2003).
21. W. Muranyi, J. Haas, M. Wagner, G. Krohne, and U. H. Koszinowski, "Cytomegalovirus recruitment of cellular kinases to dissolve the nuclear lamina," Science **297**, 854–857 (2002).
22. W. S. Rasband, "ImageJ," U. S. National Institutes of Health, http://imagej.nih.gov/ij/.

1. Introduction

The physical dimensions of viruses are smaller than the resolution limit of far field microscopy thereby precluding direct observation. As a result, many studies focus on examining the host–pathogen interactions which can be observed with far field microscopy. These studies generally involve labelling cells with fluorescent markers. However, labels can degrade into toxic photochemical reaction products and can also perturb the native biochemical pathways which operate between host and pathogen. This has restricted many previous investigations to working with fixed rather than living cells.

In this paper we demonstrate the application of far field microscopy to the study of host–pathogen interactions in unlabelled live cells. Specifically, we examine the correlation between cytomegalovirus infection and the behaviour of cellular lipid droplets by imaging live cells on a multimodal microscope platform which combines coherent anti-Stokes Raman scattering (CARS) and two-photon fluorescence (TPF). This work extends our previous study [1] which was based only on fixed cell samples.

The importance of label-free live cell imaging has led to the development of a variety of new methods for far field microscopy. Among them, CARS has emerged as the ideal technique for imaging cellular lipid droplets [2, 3]. The basic functions of lipid droplets as a store for energy reserves, hydrophobic compounds, and membrane building blocks have long been understood [4]. Recently, the more subtle and complex role played by these organelles has been revealed, including the discovery that lipid droplets are appropriated by the hepatitis C virus during the infection cycle [5–8]. CARS is clearly a valuable tool for the study of the link between lipids and viral replication. Used alone however, CARS is insufficient for identifying the infection state of cells, so we combine CARS with TPF to simultaneously image cellular lipid droplets whilst identifying and monitoring viral activity using a genetically modified

#147177 - $15.00 USD Received 9 May 2011; revised 5 Jun 2011; accepted 8 Jul 2011; published 2 Aug 2011
(C) 2011 OSA

murine cytomegalovirus (mCMV). The virus causes the host cell to express green fluorescent protein (GFP) upon infection.

The use of the modified virus allows the cellular expression of GFP to be utilised as a definitive marker of infection, to indicate that cellular translation of viral mRNA has begun. The modified genetic code persists in the DNA of viral progeny, therefore GFP expression continues for an extended time period after the initial infection. Furthermore, with this technique, it is possible to use the GFP expression to correlate observed cell changes with the overall timescale of the infection process. This imaging technique avoids the problems of toxicity, changes to cell function and fluorophore fading inherent to fluorescent labels.

In our previous study [1] we combined CARS and TPF imaging to compare fixed samples of healthy (uninfected) and infected mouse fibroblast cells. The main results were that the virus causes morphological changes to the cell, including expansion of the cell nucleus, and that an apparent rearrangement of lipid droplets occurs at some point during the infection process.

The aim of this study is to understand this dynamic process by relating the observed changes in lipid droplet configuration with the GFP expression, and hence the infection stage. A preliminary study of fixed cell samples is used to systematically identify the stages of viral infection by observing the quantity of GFP expression within the cell. We then image the lipid droplet behaviour in live cells during the infection process by using the fixed cell data as a reference to identify the stage of infection from the level of GFP expression.

2. Experimental Method

2.1. Sample Preparation

The method for sample preparation and infection with the genetically modified virus was described in detail in a previous paper [1]. Briefly, NIH/3T3 fibroblast cells with a passage number in the range 11–20 were cultured in Dulbecco's modified Eagle's medium (DMEM), with L-glutamine (200 mol/m^3), penicillin/streptomycin (10 000 units/ml) and 10 % calf serum. Standard growth conditions of 37 °C and a 5 % CO_2 environment were maintained during an incubation period of 12 hours. Cells were seeded onto glass-bottom Petri dishes (P35Gcol-1.0-14-C, MatTec). Infection with mCMV wildtype mutant C3X was carried out using a genetically modified version of the Smith strain [9] at a multiplicity of infection of 1, with the growth media containing 3 % calf serum in order to reduce cell growth.

2.2. Preliminary Study

A preliminary study was conducted with fixed cells, prepared as described above, with the exception that the cells were seeded onto glass coverslips and fixed using 1 % formaldehyde in phosphate buffered saline. By using a synchronized transfection method [10] a range of samples were fixed at known time points between 0 and 96 hours post transfection (hpt). The samples therefore consisted of a large number of cells fixed at the same time (hpt) in the infection cycle.

2.3. Live Cell Chamber

A portable cell chamber was built to provide a suitable environment for sustaining live cells on the microscope stage. The chamber was designed to attach directly onto the microscope, as shown in Fig. 1. Since the function of the chamber was to sustain a stable population of living cells, access for passaging or perfusion was not required. Therefore, the chamber was designed to be airtight, to maintain a 5 % CO_2 atmosphere, and to provide a controlled temperature of 37.0 °C [11]. The top window of the chamber was designed to touch the growth media in order to minimize signal loss due to refraction and to prevent the formation of condensation on the glass. We found that this set-up enabled live cells to survive on the microscope for at

#147177 - $15.00 USD Received 9 May 2011; revised 5 Jun 2011; accepted 8 Jul 2011; published 2 Aug 2011
(C) 2011 OSA

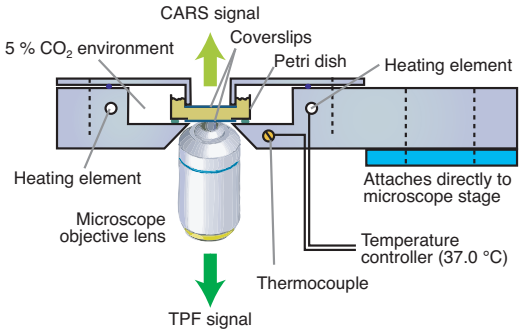

Fig. 1. Portable cell chamber for live cell imaging. A glass-bottom Petri dish containing the cell sample is sealed into the chamber in a 5 % CO_2 environment. The aluminium chamber body is fitted with heating elements and connected to a temperature controller which maintains a constant temperature of 37.0 °C. The chamber attaches directly to the stage of the (custom-built) microscope.

least 7 days. This was verified by observing a gradual growth in cell population from the initial 50–70 % to 100 % confluence over the period. A phenol-red indicator confirmed that neutral pH was maintained, suggesting that the CO_2 concentration remained constant inside the chamber [12, 13]. As cytomegalovirus completes its replication cycle after 72 hours at most [14], the longevity of cells in the chamber is more than sufficient for the process being investigated.

2.4. Imaging Instrumentation

A custom-built laser-scanning inverted CARS microscope setup [1], shown in Fig. 2, was used to record both CARS and TPF images simultaneously. The laser source was a pair of titanium-sapphire lasers (Mira 900, Coherent), which were mode-locked and synchronized via a phase-locked loop system [15] (Synchrolock, Coherent).

The 2845 cm^{-1} Raman vibration, which corresponds with the aliphatic C–H vibrations found in lipids [16], was targeted by tuning the pump laser wavelength to 714 nm and the Stokes laser to 896 nm. This generated a CARS signal at 593 nm, which was reflected out of laser beam path with a long wave-pass dichroic mirror (683dcxr, Chroma) and further filtered with a short wave-pass filter (680/SP-25, Semrock) and a narrow band-pass filter (600/14-25, Semrock). The forward CARS (F-CARS) signal was detected with a photomultiplier tube (PMT) (R3896, Hamamatsu).

The Stokes beam at 896 nm falls within the excitation band of GFP, allowing simultaneous TPF imaging with CARS. Unlike CARS, TPF is non-directionally scattered [17] and is most efficiently collected in the backward direction. A dichroic mirror behind the objective lens reflected the TPF signal out of the beam path. An identical PMT (R3896) was used to detect the signal. Two filters, a short wave-pass (680/SP-25, Semrock) and a broad band-pass (510/84-25, Semrock), were used to block the pump and Stokes laser wavelengths whilst transmitting most of the GFP emission spectrum. The band-pass filter also blocks the CARS signal at 593 nm. The picosecond pulse duration used in this set-up is ideal for CARS microscopy, but less so for TPF. Nonetheless, it is still capable of producing high-quality TPF images [18].

Image acquisition was achieved with a customized LabVIEW program, which controls the beam scanning mirrors and records the CARS and TPF PMT signals. The laser power at the sample was adjusted with neutral density filters (not shown in the figure). Bright field microscopy was used for all sample alignment and focusing in order to minimize the exposure of the sample to the laser beam.

#147177 - $15.00 USD Received 9 May 2011; revised 5 Jun 2011; accepted 8 Jul 2011; published 2 Aug 2011
(C) 2011 OSA

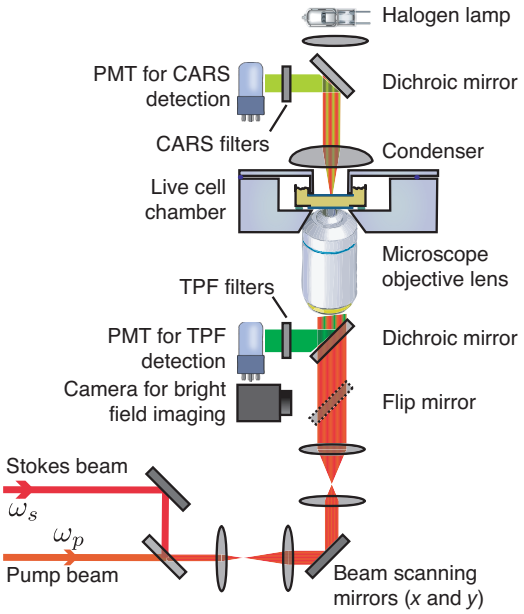

Fig. 2. Multimodal CARS and TPF microscopy system. The Stokes laser is tuned to 896 nm and the pump to 714 nm, to target a Raman shift of 2845 cm^{-1}. The two lasers are mode-locked and the pulses are synchronized. An *x*–*y* pair of galvanometer mirrors is used to scan the combined beams across the sample. The CARS signal is detected by a photomultiplier tube (PMT) in the forward direction (F-CARS) and TPF is detected, also by a PMT, in the backward direction. The set-up can also perform bright field imaging with a halogen lamp and camera.

3. Results and Discussion

3.1. Multimodal microscopy: simultaneous CARS and TPF

We used CARS to target the C–H Raman band at 2845 cm^{-1}. Bright spots were observed in the cytosol, which were identified as the resonant CARS signal from lipid droplets [16]. The cellular and nuclear membranes were also visible in CARS images due to the nonresonant background, revealing the cell morphology and the outline of the nucleus as a dark elliptical region.

Simultaneous and sequential CARS and TPF images are shown in Fig. 3. Sequential TPF images (Fig. 3(C)) were collected by scanning the Stokes laser beam only, the wavelength of which falls within the two-photon excitation band of GFP. It is evident that the TPF images generated simultaneously with CARS (Fig. 3(B)) are comparable to the images generated sequentially (Fig. 3(C)), with both TPF images revealing similar features. The bright high-contrast spots in the simultaneous image (Fig. 3(B)) could in principle arise from either CARS or GFP. To confirm that cross-channel leakage was not significant, pairs of images were taken with the phase of the pump and Stokes beams shifted by approximately 180° using the phase-locked loop system (Synchrolock). When the beams are out of phase, pump and Stokes pulses do not arrive at the sample simultaneously, so frequency mixing cannot occur and no CARS signal is generated. This test allows ready discrimination of the TPF signal from the CARS and confirmed that the filters prevented cross-channel leakage. The bright spots in TPF images recorded simultaneously with CARS (Fig. 3(B)) were therefore unambiguously identified as sites of GFP

#147177 - $15.00 USD Received 9 May 2011; revised 5 Jun 2011; accepted 8 Jul 2011; published 2 Aug 2011
(C) 2011 OSA

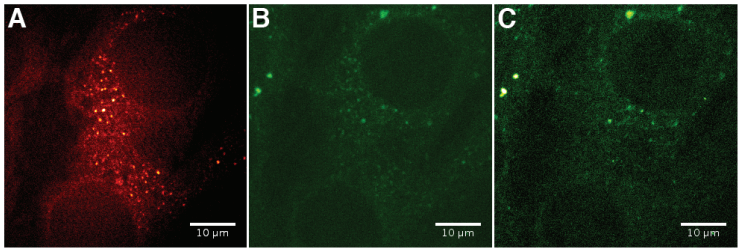

Fig. 3. Images of fibroblast cells infected with a genetically modified mCMV which causes cellular expression of GFP. The CARS image (A) shows the distribution of cellular lipid droplets. The TPF image (B), acquired simultaneously with the CARS, shows the sites of GFP, indicating that the cell is infected. A second TPF image (C) was recorded after the CARS image (sequentially) using only the Stokes laser beam; the pump beam was blocked.

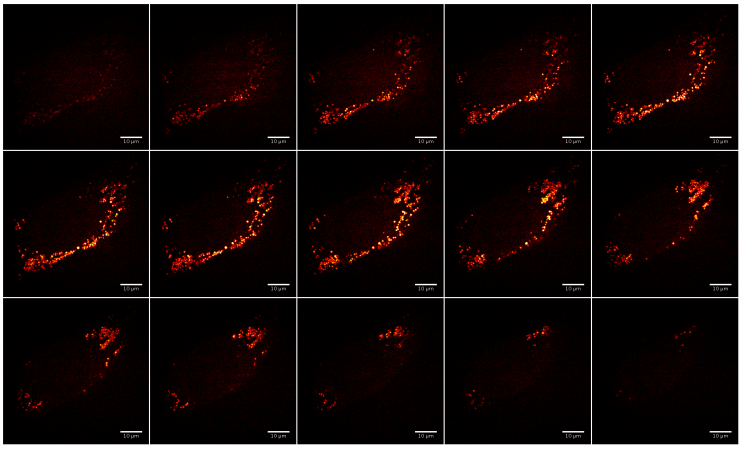

Fig. 4. A stack of CARS images through a single cell. Slices were taken at 0.25 μm increments in the z-direction. The laser power at the sample was approximately 35 mW. The bright spots visible in the images were identified as lipid droplets.

accumulation.

3.2. Cell Viability

The setup enabled acquisition of high-contrast CARS images using a reasonably low laser power of approximately 35 mW at the sample. Figure 4 shows a stack of images of a single live cell at increments of 0.25 μm, starting from the coverslip and scanning upwards in the z-direction. Bright field images were taken before (Fig. 5(A)) and after (Fig. 5(B)) recording the stack to assess possible photodamage. The image taken after recording the stack shows morphological changes to the cellular membrane, suggesting that some photodamage had occurred. Images of the same cell recorded two hours later, Fig. 6, revealed that the cell had become rounded and detached from the surface of the Petri dish. Nearby cells retained a normal appearance, indicating that the cell's death was due to photodamage.

The accumulated laser exposure experienced by a cell during stack acquisition is far greater than required for imaging a single slice. We tested cell viability against a range of laser powers in order to determine the optimum parameters for 2D imaging. We found that acquiring a 512×512 pixel image and integrating over 4 scans provided the optimum balance between

#147177 - $15.00 USD Received 9 May 2011; revised 5 Jun 2011; accepted 8 Jul 2011; published 2 Aug 2011
(C) 2011 OSA

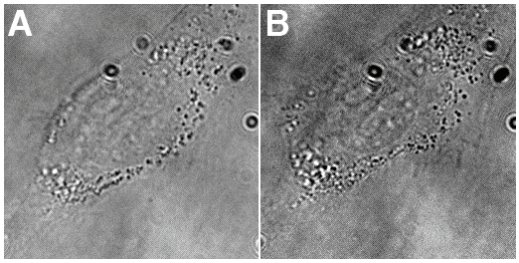

Fig. 5. Brightfield images recorded before (A) and after (B) the acquisition of the stack shown in Fig. 4. Visible photodamage is apparent after laser scanning.

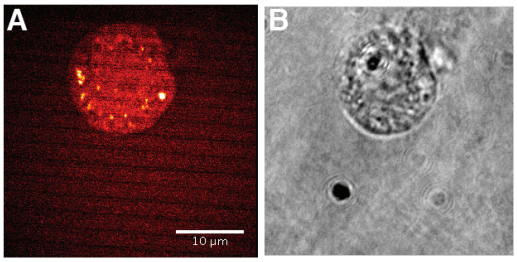

Fig. 6. CARS (A) and brightfield (B) images of the same cell shown in Fig. 4 and Fig. 5 recorded 2 hours after acquisition of the stack.

noise, image contrast and acquisition time. The minimum power achieved at these parameters was approximately 28 mW at the sample. Increasing the laser power increased the image contrast, but also increased the likelihood of photodamage.

Viability was tested with different cells over a range of laser powers in order to determine whether higher laser powers caused immediate damage to the cell morphology. It was found that powers up to 120 mW could be used without causing morphological changes in the cell on the timescale of the imaging. However the accumulated photodamage typically caused a delayed change in cell morphology after imaging. As a result, long time-course experiments, which involve imaging a single cell over many hours cannot be carried out at present. Instead, we are able to image many cells within the same live cell population over a time period of interest. This gives an overall view of the state of the cell population at the specific time point, and thus allows the change in overall cell population to be assessed over the time-course of infection.

3.3. Preliminary Study: Identification of Infection Stages

Samples of infected cells were fixed at 3 hour intervals and visually classified into three distinct groups: group 1, cells show low or nil concentrations of GFP, along with no significant changes to lipid droplet configurations compared to uninfected cells (0–9 hpt); group 2, cells show higher concentrations of GFP and significant changes to lipid droplet configuration (9–24 hpt); group 3, cells show major morphological changes and lipid droplet configuration changes, plus very high concentrations of GFP observed in the cells ($>$ 24 hpt). We refer to these groups respectively as the early, intermediate and late stages of infection.

All cell samples in the early infection stage (0–9 hpt) displayed similar features to those exhibited by the cell in Fig. 7. During this stage, CARS images showed both uniform size and spatial distributions of lipid droplets throughout the cytosol. TPF images had zero or limited

#147177 - $15.00 USD Received 9 May 2011; revised 5 Jun 2011; accepted 8 Jul 2011; published 2 Aug 2011
(C) 2011 OSA

contrast, indicating either no GFP, or the presence of a low concentration of GFP in the cytosol. There was no TPF signal from the nucleus, as GFP is expressed in the cytoplasm. The images also show areas of small accumulations of GFP in the cytosol, which could indicate the sites of GFP expression or suggest vesicle-mediated GFP transport.

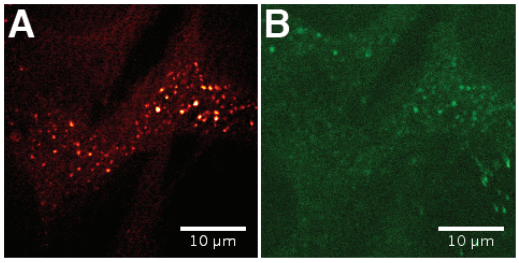

Fig. 7. CARS (A) and TPF (B) images of cells fixed at the early stage of infection. Lipid droplets of regular size are uniformly distributed in the cytosol. The low level of fluorescence provides limited contrast in the TPF image.

Cell samples infected for 9–24 hpt, the intermediate stage, typically exhibited the features shown in Fig. 8. The cells in this group displayed some lipid droplet clustering, where non-uniform spatial distributions of lipid droplets and some relatively large lipid droplets were identifiable. In addition, a general increase in cell nucleus area was evident. This is consistent with our earlier study [1], although in that investigation we were unable to associate nuclear expansion with a definite infection stage. The larger overall TPF signal indicated higher concentrations of GFP in the cytosol, thus confirming a progression of the infection.

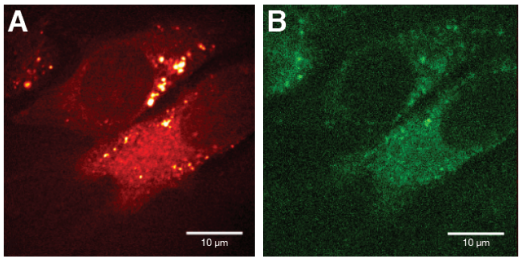

Fig. 8. CARS (A) and TPF (B) images of cells in the intermediate stage of infection. The distribution of lipid droplets is less uniform than in the early stage (Fig. 7) with the emergence of some clustering. The TPF image shows an increased amount of GFP expression.

Samples containing cells infected for $>$ 24 hpt, Fig. 9, we designated as the late stage of infection. Cells in this infection stage imaged using CARS show a dramatic reduction in the number of lipid droplets. The corresponding TPF images indicated high concentrations of GFP in both cytosol and nucleus, showing that GFP is imported into the cell nucleus at this late infection stage. Additionally, many images display fragmented cell nuclei, which suggests the cells are undergoing apoptosis.

Since GFP is expressed as a result of viral protein translation, we expect the fluorescence intensity to increase as the infection progresses. Figure 10 shows the measure of intensity of intracellular fluorescence per cell throughout the infection process. The graph shows a significant increase in fluorescence intensity as the infection progressed, where an average intensity of 17.3, 160.4 and 1025.9 (normalised units) was measured for each group of infected cells.

#147177 - $15.00 USD Received 9 May 2011; revised 5 Jun 2011; accepted 8 Jul 2011; published 2 Aug 2011
(C) 2011 OSA

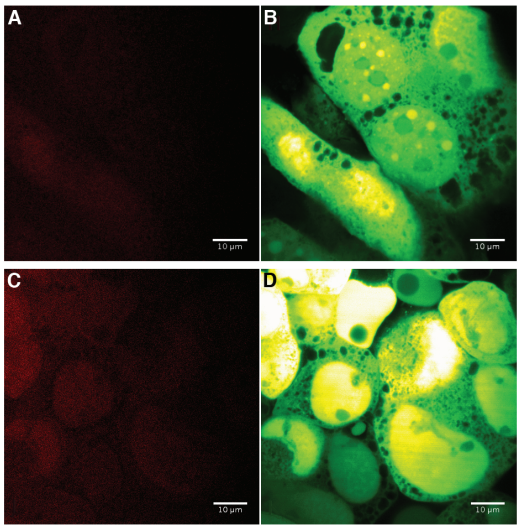

Fig. 9. CARS (A) and TPF (B) images of a sample of cells fixed in the late infection stage. (C) and (D) are CARS and TPF images of a different area of the same sample. The contrast in the two CARS images (A,C) is very limited due to the absence of lipid droplets. The TPF images (B,D) show a high level of GFP expression as well as fragmentation of cell nuclei suggesting apoptosis.

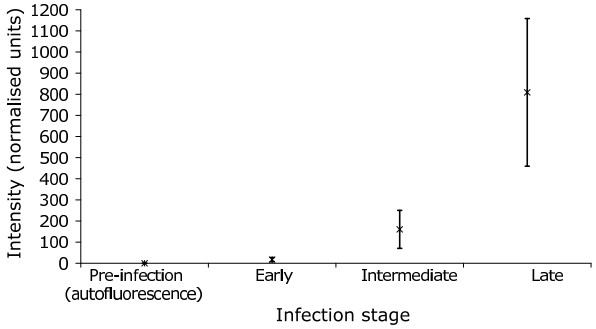

Fig. 10. Graph showing the average intensities for TPF images acquired pre-infection; and during the early, intermediate and late stages. Error bars indicate 1 standard deviation. To account for small changes in laser power between images the two-photon intensities have been normalized by dividing by the square of the power.

Pre-infection TPF images were also acquired where an average intensity of 0.09 was measured, indicating that there was no significant autofluorescence background in TPF images.

3.4. Imaging of Live Infected Cells

Although our preliminary study allowed us to group the infection process into three visually distinct stages, it is unsuitable for quantitative analysis of the observed changes in lipid droplet configuration because the formaldehyde fixing method causes rapid degradation of lipid droplets [19]. Therefore, the use of live cell samples is imperative for further analysis of lipid droplet characteristics during the infection process. Different cells in live samples had often progressed to different stages of the infection process, therefore within one image, each cell

#147177 - $15.00 USD Received 9 May 2011; revised 5 Jun 2011; accepted 8 Jul 2011; published 2 Aug 2011
(C) 2011 OSA

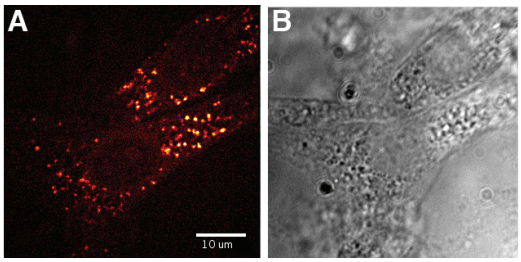

Fig. 11. CARS (A) and bright field (B) images of a group of live cells during the early stage of infection. The CARS image shows lipid droplets of regular size uniformly distributed throughout the cytosol. The pump and Stokes laser powers at the sample were approximately 25 mW and 30 mW respectively. The bright field image shows the cell outlines only.

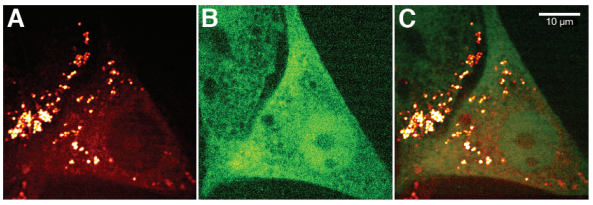

Fig. 12. CARS (A) and TPF (B) images of two cells in the intermediate stage of infection. The images are overlaid in (C). The pump and Stokes laser powers at the sample were approximately 28 mW and 32 mW respectively. The CARS image shows a non-uniform distribution of lipid droplets within the cytosol, with the appearance of clustering, specifically towards the neighbouring cell. The TPF image confirms that the cells are infected, and also shows that some GFP has been imported into the nucleus.

may be at a different stage of infection, as evident in Fig. 13(B). Using the data from the preliminary study we were able to assign the live cells to a definite stage (early, intermediate or late) of the infection process.

Cells in the early stage of infection provided a low overall intensity in TPF images. GFP expression is initiated by cellular translation of viral mRNA, therefore the initial appearance of GFP within the cell can be attributed to the onset of viral replication. CARS images of live cells acquired during the early infection stage, such as the image shown in Fig. 11, clearly show regularly-sized lipid droplets uniformly distributed throughout the cytosol, consistent with the preliminary study (Fig. 7).

CARS images acquired from cells in the intermediate stage of infection, such as the image shown in Fig. 12, showed non-uniform spatial distribution of lipid droplets throughout the cytosol. In addition, some relatively large lipid droplets were seen, suggesting a clustering effect. This behaviour is consistent with observations in the preliminary study (Fig. 8). Furthermore, some images of live cell infection, including Fig. 12, suggested that lipid droplets migrated towards neighbouring cells. Live cell TPF images revealed GFP in a number of cell nuclei. This feature was not observed in fixed cell images at the same infection stage, where GFP was only detected in the nucleus during the late stages of infection. These live cell images suggest that nuclear import of GFP occurs during the same infection stage as lipid droplet aggregation, indicating a possible link between the two processes. The import of GFP into the nucleus was an unexpected feature. Since GFP is synthesized in the cytosol, and nucleocytoplasmic transport is highly controlled [20], large molecules such as GFP must be actively transported in order to

#147177 - $15.00 USD Received 9 May 2011; revised 5 Jun 2011; accepted 8 Jul 2011; published 2 Aug 2011
(C) 2011 OSA

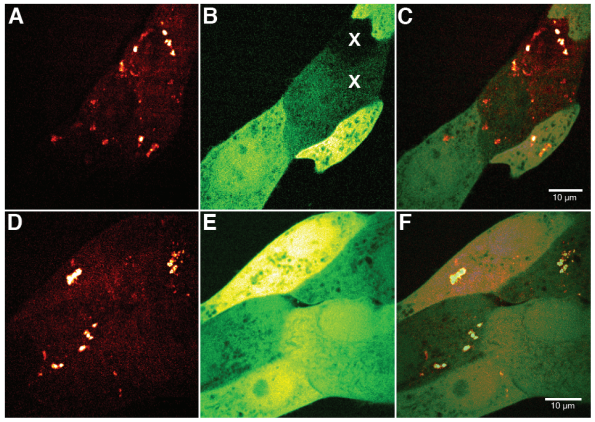

Fig. 13. CARS (A), TPF (B) and overlaid (C) images of a group of live cells in the late infection stage. (D–F) show a different group of cells. The pump and Stokes laser power at the sample was approximately 43 mW and 47 mW respectively. The CARS images (A,D) show a small number of lipid clusters. The high intensity in the corresponding TPF images (B,E) confirm the late stage of infection. Inhomogeneous infection is evident in image (B), where most cells are in the late infection stage with the exception of the two cells marked X which are in the intermediate stage, identified using fixed cell data as a reference.

enter the nucleus. This suggests that the behaviour may not be a cellular function initiated by the virus but rather a side-effect of infection caused by some mechanism occurring within the cell during the infection cycle [21].

CARS images of cells in the late stages of infection, Fig. 13, show a significant reduction in the number of lipid droplets. Where lipid droplets were still visible, much larger droplet sizes were typical. The high intensity in TPF images provided evidence of fragmented cells and apoptosis.

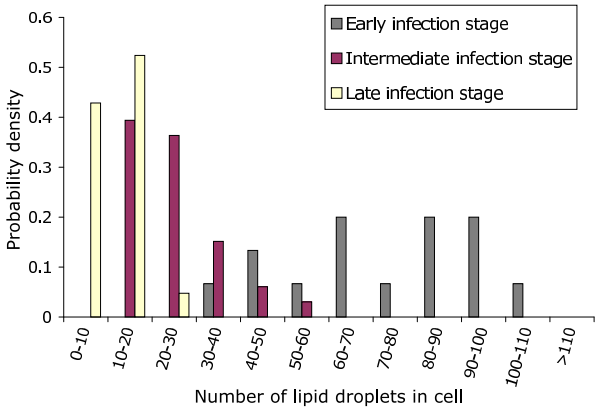

Fig. 14. Histogram showing the probability distribution of the number of lipid droplets in a cell for the early, intermediate and late infection stages. The separate counts for each infection stage group were binned and are plotted in the histogram. An empty bin for a particular infection stage indicates that there were no cells whose lipid droplet count was within the bin range.

#147177 - $15.00 USD Received 9 May 2011; revised 5 Jun 2011; accepted 8 Jul 2011; published 2 Aug 2011
(C) 2011 OSA

To confirm that the observed reduction in lipid droplet number is linked to the infection process, a sample of 69 cells was examined in more detail. The cells were first grouped into the three infection stages-early, intermediate and late-based on the level of GFP expression identified by the preliminary study. For each infection stage group, the number of lipid droplets per cell was counted. The histogram in Fig. 14 shows the probability that a cell has a given number of lipid droplets during the early, intermediate and late stages of infection. A clear decrease in lipid droplet number throughout the infection process is apparent. The mean number of lipid droplets are 63, 29 and 14, for the early, intermediate and late infection stages respectively, where the early infection probability distribution is between $37 \rightarrow 106$ lipid droplets, the intermediate infection probability distribution is between $12 \rightarrow 54$ lipid droplets, and the late infection probability distribution show that no cell contains more than 21 lipid droplets from the data set collected.

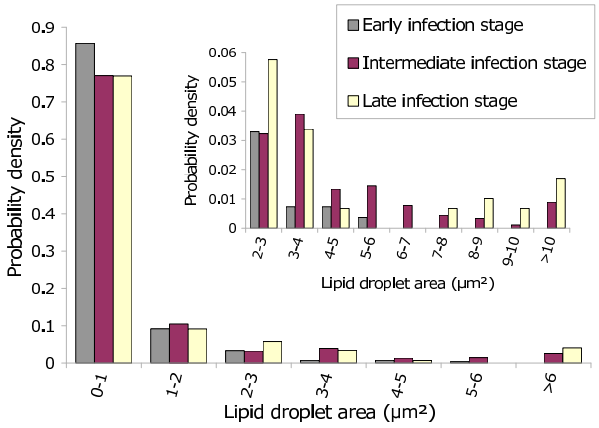

Fig. 15. Histogram showing the probability distribution of lipid droplet area for the early, intermediate and late infection stages. Inset: histogram (of the same data) showing the probability distribution of the lipid droplets with area greater than 2 μm^2.

In addition to a reduction in the number of lipid droplets, there appeared to be an increase in the size of the remaining droplets. In order to quantitatively determine the change in size due to clustering, the areas of lipid droplets were measured in a large sample of cells using ImageJ [22]. 545, 897 and 295 lipid droplet areas were measured for the early, intermediate and late infection stages respectively. A histogram showing the probability of measuring lipid droplets with a certain size during each infection stage is shown in Fig. 15. In the early infection stage, 86 % of the cells' lipid droplets were less than 1 μm^2 in size. This confirmed the observation in CARS images that lipid droplets were broadly similar in size during this infection stage. The graph also shows high probability of measuring lipid droplets with sizes less than 1 μm^2 for the intermediate and late infection stages, both 77 %. The difference between the lipid droplet sizes throughout the infection stages are most evident when looking at lipid droplets with area greater than 6 μm^2. In the intermediate infection stage, there was an increased probability of finding lipid droplets larger than 6 μm^2, with the probability further increasing in the late infection stage. No lipid droplets larger than 5.8 μm^2 were measured in cells in the early infection stage, showing that as the infection progresses, the probability of finding larger lipid droplets increases. This behaviour is highlighted by the inset in Fig. 15, where the histogram shows the probability distribution in more detail for the lipid droplets larger than 2 μm^2. These results confirm the observation of progressive lipid droplet clustering during infection.

#147177 - $15.00 USD Received 9 May 2011; revised 5 Jun 2011; accepted 8 Jul 2011; published 2 Aug 2011
(C) 2011 OSA

4. Conclusion

We have shown that a multimodal CARS and TPF microscope system allows the observation and measurement of changes in live fibroblast cells that occur during infection by cytomegalovirus. Imaging with TPF allowed us to identify three distinct stages of the infection process; early, intermediate and late infection stage, whilst simultaneous CARS imaging was used to observe the changes in cell morphology, and to quantify the perturbations to cellular lipid droplets, enabling us to correlate these findings against the defined infection stages. This enabled us to identify several persistent features of cytomegalovirus infection including a change in cell morphology, a decrease in the number of cellular lipid droplets and an overall increase in the size of the remaining droplets, thus suggesting a clustering of lipid droplets. The increase in the size was significant, with some lipid droplets of area greater than 6 μm^2 emerging in the later stages of infection. The biological significance of these observed processes requires further investigation.

Acknowledgments

We appreciate the provision of C3X-GFP virus from Mathieu Blanc of the Division of Pathway Medicine, University of Edinburgh.

#147177 - $15.00 USD Received 9 May 2011; revised 5 Jun 2011; accepted 8 Jul 2011; published 2 Aug 2011
(C) 2011 OSA